

Development and Evaluation of Distributed Energy Resource Device Models

Electric Vehicles, Electric Water Heaters,
and Commercial Refrigeration Systems

July 2020



GRID
MODERNIZATION
LABORATORY
CONSORTIUM
U.S. Department of Energy

Argonne National Laboratory
National Renewable Energy Laboratory
Oak Ridge National Laboratory

Development and Evaluation of Distributed Energy Resource Device Models

Electric Vehicles, Electric Water Heaters, and
Commercial Refrigeration Systems

Argonne National Laboratory

Michael Douba

Alejandro Fernandez Canosa

National Renewable Energy Laboratory

Chuck Booten

Bethany Sparn

Jeff Maguire

Sivasathya Balamurugan

Oak Ridge National Laboratory

Jeffrey Munk

Teja Kuruganti

Jian Sun

Boroi Cui

Jin Dong

July 2020

This report was prepared as an account of work sponsored by an agency of the United States Government. Neither the United States Government nor any agency thereof, nor any of their employees, makes any warranty, express or implied, or assumes any legal liability or responsibility for the accuracy, completeness, or usefulness of any information, apparatus, product, or process disclosed, or represents that its use would not infringe privately owned rights. Reference herein to any specific commercial product, process, or service by trade name, trademark, manufacturer, or otherwise, does not necessarily constitute or imply its endorsement, recommendation, or favoring by the United States Government or any agency thereof. The views and opinions of authors expressed herein do not necessarily state or reflect those of the United States Government or any agency thereof.

This research was supported by the Grid Modernization Initiative of the U.S. Department of Energy (DOE) as part of its Grid Modernization Laboratory Consortium, a strategic partnership between DOE and the national laboratories to bring together leading experts, technologies, and resources to collaborate on the goal of modernizing the nation's grid.

Acknowledgments

The authors would like to acknowledge the valuable guidance and input provided during the preparation of this report. In particular, the authors are grateful to Rob Pratt and Hayden Reeve from Pacific Northwest National Laboratory.

Contents

1.0	Electric Vehicles.....	1.1
2.0	Electric Water Heaters.....	2.1
3.0	Commercial Refrigeration Systems	3.1

Part 1

1.0 Electric Vehicles

Argonne National Laboratory
Michael Duoba
Alejandro Fernandez Canosa

Acronyms and Abbreviations

AC	alternating current
ANL	Argonne National Laboratory
BEV	battery electric vehicle
BMS	battery management system
CAN	controller area network
DC	direct current
DER	distributed energy resources
EV	electric vehicle
EVSE	electric vehicle supply equipment
GMLC	Grid Modernization Laboratory Consortium
MY	model year
OEM	original equipment manufacturers
REx	range extender
SAE	Society of Automotive Engineers
SoC	state of charge
V2G	vehicle to grid

Table of Contents

1.1	Introduction	1.7
1.2	Electric Vehicle Model.....	1.7
1.2.1	Main Assumptions and Scope	1.8
1.2.2	Modeling Physics of Battery and Losses During Charging.....	1.9
1.2.3	Modeling Transient Response to Charging Rate Changes	1.10
1.2.4	Energy Consumption During Driving	1.11
1.3	Test Vehicles and Hardware.....	1.12
1.3.1	Battery Electric Vehicles Tested	1.12
1.3.2	Testing Hardware and Data Acquisition Setup.....	1.12
1.4	Test Procedures.....	1.17
1.4.1	Relevant Standards and Test Methods.....	1.17
1.4.2	Variable Charge Rate Tests	1.18
1.4.3	Driving and Charging Schedule Tests	1.18
1.5	Experimental Results and Model Validation.....	1.19
1.5.1	Resistance and V_o	1.19
1.5.2	Variable Charge Rate Tests	1.20
1.5.3	Dynamometer Driving and Charging Results.....	1.30
1.5.4	Validation Models with Simulations	1.33
1.6	Conclusions/Observations	1.39
1.7	References	1.40

Figures: Part 1

Figure 1. Schematic description of the fleet generation process.....	1.8
Figure 2. Simple ohmic model of the EV battery pack.....	1.9
Figure 3. Modeling transient response.....	1.11
Figure 4. ANL’s patented Smart Charge Adapter.....	1.13
Figure 5. ANL’s custom-built EVSE with cloud-based controls.....	1.14
Figure 6. Hioki 3390 Power Analyzer meters (four channels each). The main display shows the values of voltages, current, and power of the selected nodes. The data is logged and saved in csv format, which is then merged with the vehicle CAN data.	1.15
Figure 7. Clamp-on current probe measuring total accessory losses	1.15
Figure 8. Example of transient recharge test schedule segment	1.18
Figure 9. Four-day test schedule to emulate typical EV operation	1.19
Figure 10. Nissan Leaf open circuit voltage and resistance results from testing	1.19
Figure 11. BMW i3 open circuit voltage and resistance results from testing	1.20
Figure 12. Chevy Bolt open circuit voltage and resistance results from testing	1.20
Figure 13. Transient response of the EVs of study. From left to right: MY2014 BMW i3, MY2017 Chevrolet Bolt, and MY2012 Nissan Leaf.	1.21
Figure 14. Transient response of the EVs of study when the battery is almost full. From left to right: MY2014 BMW i3, MY2017 Chevrolet Bolt, and MY2012 Nissan Leaf. Note that the request is poorly tracked at the levels of charge presented here.	1.22
Figure 15. Experimental results and polynomial fitting of AC to DC power losses as a function of the AC power at different voltage levels for the MY2014 BMW i3 REX.....	1.23
Figure 16. Experimental results and polynomial fitting of AC to DC power losses as a function of the AC power at different power levels for the MY2017 Chevrolet Bolt	1.24
Figure 17. Experimental results and polynomial fitting of AC to DC power losses as a function of the AC power at different power levels for the MY2012 Nissan Leaf	1.25
Figure 18. Power losses (left) and AC-DC power conversion efficiency (right) for the three vehicles of study.....	1.26
Figure 19. Experimental results and polynomial fitting of slew rate as a function of the variation of the current commanded at different power levels for the MY2014 BMW i3 REX.....	1.27
Figure 20. Experimental results and polynomial fitting of slew rate as a function of the variation of current commanded at different power levels for the MY2017 Chevrolet Bolt	1.28
Figure 21. Experimental results and polynomial fitting of slew rate as a function of the variation of current commanded at different power levels for the MY2012 Nissan Leaf.....	1.29
Figure 22. Slew rate (left), negative response times (center), and positive response times (right) models for the three vehicles of study.....	1.30
Figure 23. Drive cycles of various lengths from Lee and Filipi (2011) used to determine consumption as a function of average trip speed.....	1.31
Figure 24. Rate of energy consumption per unit of mile as a function of the average speed for the 2014 BMW i3 REX, 2017 Chevrolet Bolt, and 2012 Nissan Leaf.....	1.32

Figure 25. Time plot of the MY2014 BMW i3 REx charger transient model validation: AC power commanded (solid line), DC experimental power (dashed line), and DC modeled power (dashdot line).....	1.33
Figure 26. Details of the time plot of the MY2014 BMW i3 REx charger transient model validation: AC power commanded (solid line), DC experimental power (dashed line), and DC modeled power (dashdot line)	1.34
Figure 27. Time plot of the MY2017 Chevrolet Bolt charger transient model validation: AC power commanded (solid line), DC experimental power (dashed line), and DC modeled power (dashdot line).....	1.34
Figure 28. Details of the time plot of the MY2017 Chevrolet Bolt charger transient model validation: AC power commanded (solid line), DC experimental power (dashed line), and DC modeled power (dashdot line)	1.35
Figure 29. Time plot of the MY2012 Nissan Leaf charger transient model validation: AC power commanded (solid line), DC experimental power (dashed line), and DC modeled power (dashdot line).....	1.35
Figure 30. Details of the time plot of the MY2017 Chevrolet Bolt charger transient model validation: AC power commanded (solid line), DC experimental power (dashed line), and DC modeled power (dashdot line)	1.36
Figure 31. Comparison of charging energy between experimental results and models for the three vehicles studied.....	1.36
Figure 32. Time plots of the driving cycle and the total energy consumed (experimental and modeled) while driving for the MY2014 BMW i3 REx. A 5 miles driving cycle is shown on the left and a 25 miles driving cycle is shown on the right.	1.37
Figure 33. Time plots of the driving cycle and the total energy consumed (experimental and modeled) while driving for the MY2017 Chevrolet Bolt. A 5 miles driving cycle is shown on the left and a 25 miles driving cycle is shown on the right.	1.38
Figure 34. Time plots of the driving cycle and the total energy consumed (experimental and modeled) while driving for the MY2012 Nissan Leaf. A 5 miles driving cycle is shown on the left and a 25 miles driving cycle is shown on the right.	1.38

Tables: Part 1

Table 1. Stated Physical Performance Characteristics of the Battery Electric Vehicles Tested.....	1.12
Table 2. Parameters of the Power Losses Mathematical Model and Coefficient of Determination at Different Voltage Levels for the MY2014 BMW i3 REx	1.23
Table 3. Parameters of the Power Losses Mathematical Model and Coefficient of Determination at Different Voltage Levels for the MY2017 Chevrolet Bolt	1.24
Table 4. Parameters of the power losses mathematical model and coefficient of determination at different voltage levels for the MY2012 Nissan Leaf	1.25
Table 5. Parameters of the slew rate mathematical models and coefficient of determination at different voltage levels for the MY2014 BMW i3 REx	1.27
Table 6. Parameters of the slew rate mathematical models and coefficient of determination at different voltage levels for the MY2017 Chevrolet Bolt.....	1.28
Table 7. Parameters of the slew rate mathematical models and coefficient of determination at different voltage levels for the MY2012 Nissan Leaf	1.29
Table 8. Parameters of the energy consumption models for the 2014 BMW i3 REx, 2017 Chevrolet Bolt, and 2012 Nissan Leaf	1.32

1.1 Introduction

In order to validate distributed energy resource (DER) models operated with grid services in the GMLC 1.4.2 team's February (GMLC 2019a) and July (GMLC 2019b) reports, a test and measurement program using actual DER devices was conducted by national laboratories for three devices: (1) electric vehicles (EVs), (2) water heaters, and (3) commercial refrigeration. Test procedures were developed and carried out to identify the mathematical models and their parameters that describe the operational function, characterize the physics, and obey transient response of the devices. This report focuses on the experimental results obtained to develop and verify simulations of three specific EV models. This section summarizes elements of the mathematical model and shows the necessity data collected from the EVs while charging and discharging (driving). In the course of the study, we found it necessary to make some modifications to the model to deal with observed transient behavior. Section 1.2 details the model assumptions and equations, Section 1.3 provides details of the EVs tested, Section 1.4 outlines the test procedures developed for the projects, and Section 1.5 presents the experimental results obtained for the three different EVs tested and how these results compare to the models running the same test profiles.

For further information about the model, how it is used in simulating larger subfleets, and how the generic "battery-equivalent model" is used to generically describe a number of different DER types, see "Grid Services from DER Device Fleets: Volume 1 – Battery Equivalent Models of Device and Fleets" report (GMLC 2019a).

1.2 Electric Vehicle Model

This section describes the model that represents the physics of EV recharge and driving discharge of specific vehicle models. For grid service simulations, subfleets are defined for a specific vehicle model. Each vehicle model has individual characteristics of the battery, the charging rate limits, charger efficiency, and driving discharge rates. As mentioned earlier, details of the model and its integration with grid service models are found in the GMLC (2019a) and Duoba and Fernandez Canosa (2019) reports. The purpose of this test program is to model the physical parameters of the EVs from actual laboratory vehicle testing. Figure 1 shows the model components circled in red that were sought in this testing program within the context of the other parts of the EV GMLC model.

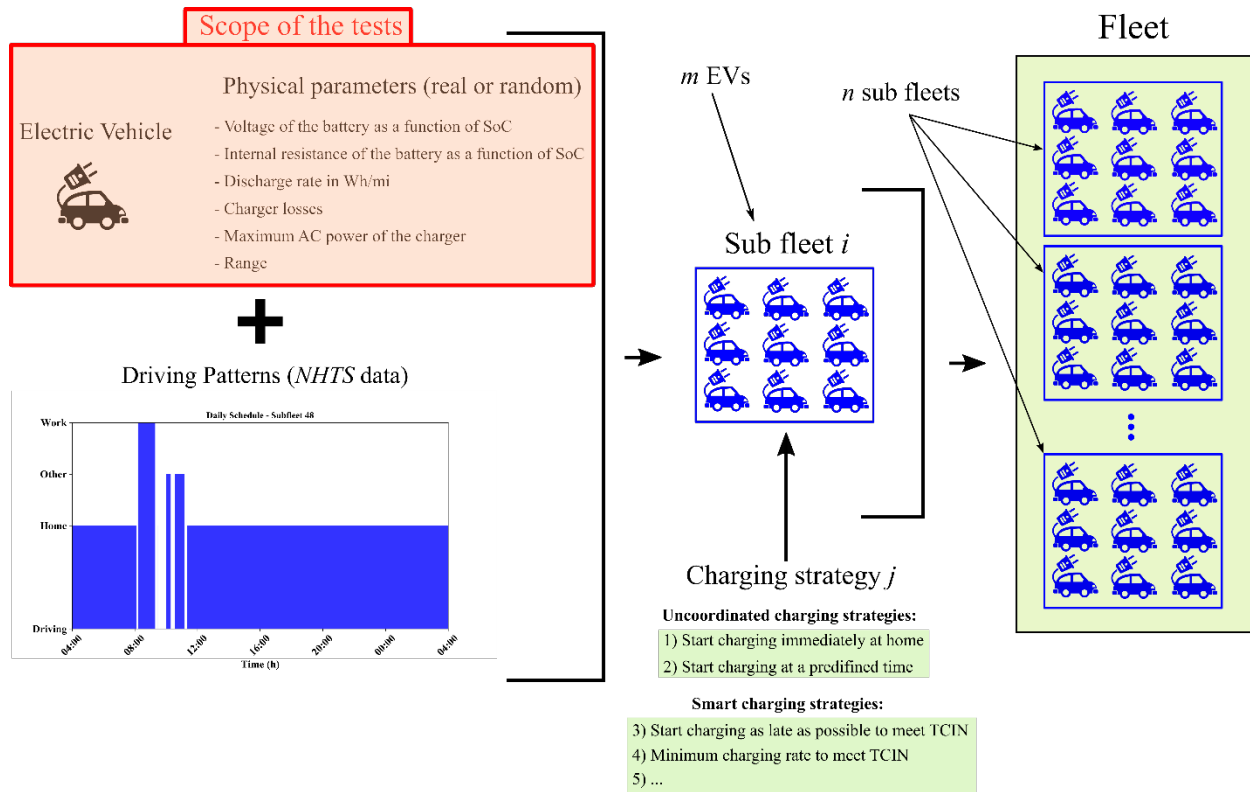


Figure 1. Schematic description of the fleet generation process

1.2.1 Main Assumptions and Scope

The main assumptions followed in this model are:

- Groups of identical vehicles are clustered together in entities called subfleets and will share the same physics and response to central recharge rate commands
- Only battery electric vehicles (BEVs) are considered
- Vehicle to grid (V2G) is not considered
- Direct current (DC) fast charging is not considered
- During charging, the current is tracked and changes in battery state of charge (SoC) are tracked using an equivalent circuit model for the battery
- During discharge (driving), a simple model of consumption as a function of speed is defined based upon dynamometer test results of “real-world” driving cycles for each specific vehicle.
- Voltage levels were varied (240, 208, 120 VAC), which provides different efficiencies and charging power levels.

1.2.2 Modeling Physics of Battery and Losses During Charging

The sequence of calculations in the model start with a known alternating current (AC) power level. For a given AC power level there is an amount of DC power flow to the battery. The total losses in the onboard charger and from the vehicle standby losses are lumped as a single “charging loss” calculation in Eq. 1. In our experience, modeling loss functions are more robust numerically than modeling efficiency curves because loss functions are somewhat linear and do not have numerical instabilities near zero power flow.

$$P_{AC} - P_{DC} = C_0 + C_1 \cdot P_{AC} + C_2 \cdot P_{AC}^2 \quad (1)$$

Where:

- P_{AC} is the total AC power flowing into the charger from the plug, expressed in W
- P_{DC} is the total DC power flowing to the battery, expressed in W
- C_0 , C_1 , and C_2 are experimentally derived coefficients found for each vehicle model and may be different for varying AC charging voltage (120, 208, and 240 VAC).

In order to track battery SoC correctly at different recharge power levels, a simple Ohmic model of the battery was chosen, described in Figure 2.

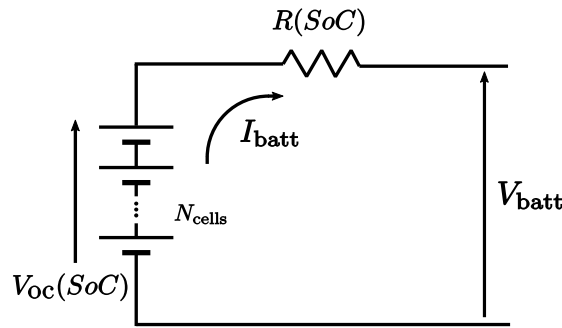


Figure 2. Simple ohmic model of the EV battery pack

During charging, for a given SoC level, the open circuit voltage and resistance are calculated using Eq. 2 and Eq. 3.

$$R = R_0 + R_1 \cdot SoC + R_2 \cdot SoC^2 \quad (2)$$

$$V_{OC} = V_0 + V_1 \cdot SoC + V_2 \cdot SoC^2 \quad (3)$$

Where:

- R is the full pack resistance, expressed in Ω .
- R_0 , R_1 , and R_2 are experimentally derived coefficients found for each vehicle model
- SoC is the state of charge, a dimensionless quantity from 0 to 1
- V_{OC} is the full battery pack open circuit voltage
- V_0 , V_1 , and V_2 are experimentally derived coefficients found for each vehicle model

Once the voltage and resistance states are determined, the current is calculated with calculation derived from the equivalent circuit of the battery pack equation as shown in Eq. 4

$$I_{batt} = \frac{V_{oc} - \sqrt{V_{oc}^2 - 4R \cdot P_{DC}}}{2R} \quad (4)$$

Where:

- I_{batt} : is the full pack current, expressed in A.

The integrated battery current (in units of ampere-hours) is used to track battery SoC. The fleet models have charging strategies based upon the battery SoC state.

1.2.3 Modeling Transient Response to Charging Rate Changes

Because large-scale “smart charging” equipment has not rolled out yet, for our testing the charging rate is controlled by the EV supply equipment (EVSE) function that limits charge rate to protect the supply side of the circuit (more details are given later in this report). Essentially, a command is sent by our test equipment to the vehicle’s charger that in turn responds by changing its power level. For an EV to be useful for grid services, the change in power level needs to be responsive. For this project we first analyzed the data before we set out to model the expected transient response for each vehicle. In many cases the dominant characteristic was simply a slew rate limit in AC current. For all the vehicles tested, the reduction in current ($-dI/dt$) was much more rapid than the increase in current—an obvious safety feature. These characteristics are depicted in Figure 3.

In some cases, there were significant and less predictable lags in achieving commanded power. An important note, the lag in time from when the test computer sends a message through the internet to command a new charge rate was not included because that may vary depending upon the upstream hardware employed for this task. The vehicle model characterizes the response once the command is detected at the vehicle.

Once the transient data for each vehicle were collected and processed, a model that relates the AC current slew rate with the commanded variation of commanded current was fitted. We assumed that the slew rate only depends on the commanded variation of current, and a second-order polynomial is considered to estimate the slew rate as shown in Eq. (6) and Figure 2.

$$\Delta I_c / t_r = \alpha_0 + \alpha_1 \Delta I_c + \alpha_2 \Delta I_c^2 \quad (6)$$

Where:

- $\Delta I_c / t_r$: is the slew rate measured in A/s
- α_0 , α_1 , and α_2 : are the coefficients of the model from least squares regression of the experimental data
- ΔI_c : is the commanded variation of current measured in A

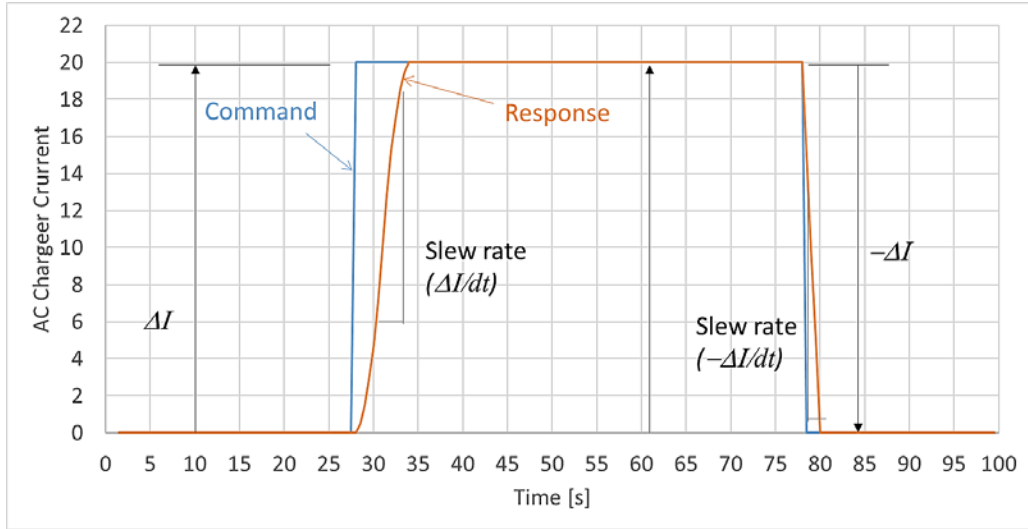


Figure 3. Modeling transient response

1.2.4 Energy Consumption During Driving

The part of the activity schedules that describe driving only have three key pieces of information: start time, end time, and distance. Thus, the only information about the trips that can differentiate a variation in consumption rate is the average trip speed. During the test program, dynamometer experiments were run with “realistic” driving schedules to find a relationship between average speed and energy consumption rate by distance (Wh/mi). The simple expression defining the consumption energy during driving is shown in in Eq. 7. More information about the testing is given in Section 1.4.

$$E_c = E_0 + E_1 \cdot V_{TripAve} \quad (7)$$

Where:

- E_c : is the energy consumption rate, expressed in Wh/mi
- E_0 and E_1 : and are experimentally derived coefficients found for each vehicle model
- $V_{TripAve}$: is the average speed of the trip being calculated for energy consumption.

1.3 Test Vehicles and Hardware




1.3.1 Battery Electric Vehicles Tested

Three BEVs of different original equipment manufacturers (OEMs) with different battery sizes were tested. The vehicles available at the Advanced Mobility and Grid Integration Technology Laboratory of Argonne National Laboratory (ANL) that were used in this testing program include:

1. Model year (MY) 2014 BMW i3 with range extender (REx)
2. MY 2017 Chevrolet Bolt
3. MY 2012 Nissan Leaf

Note that although the BMW i3 had a range extender, the BEV version has identical hardware and we are assuming in the fleet model that the vehicle is a BEV. All three test vehicles are Level 2 charging capable. More specifications are shown in Table 1.

Table 1. Stated Physical Performance Characteristics of the Battery Electric Vehicles Tested

Vehicle	Model Year	Range (mi) ¹	Nominal Capacity (kWh) ¹	Charger Power (kW) ¹	Charge Time (h) ¹
 <p>BMW i3 (REx)</p>	2014	72	22	7.7	4
 <p>Chevrolet Bolt</p>	2017	238	60	7.4	9.3
 <p>Nissan Leaf</p>	2012	84	24	3.3	7

1.3.2 Testing Hardware and Data Acquisition Setup

Testing was conducted at Argonne’s Advanced Mobility Technology Laboratory. The lab has been performing extensive data acquisition on EVs (and many other advanced powertrain technologies) operating on-road and on chassis dynamometers for decades. The experimental piece of this project focuses on collecting signals from the vehicle and measuring principal power flows while the vehicles are charging and discharging (driving). Conducting the vehicle

¹ Manufacturer’s range claims

tests required a combination of: (a) control systems with automation capabilities, (b) measurements of physical properties from different sensors (analog signals and controller area network [CAN] bus digital signals), and (c) automated data synchronization to merge and time-align data from different sources. This section details the hardware used and the data acquisition setup employed to control the experiment and collect the data.

1. *Smart Charge Adapter*: The physical layer to control charge and modulate charging rate for most of the tests was ANL's patented Smart Charger Adapter device. This device, shown in Figure 4, receives Wi-Fi commands to intercept and make changes to the Society of Automotive Engineers (SAE) J1772 pilot signal. The SAE J1772 pilot signal is read by the EV's battery management system (BMS) and limits the maximum AC current that the vehicle can draw from the AC electric circuit. The BMS of the EV is ultimately in control of the charging rate, but this pilot signal provides way power that can be modulated by a grid service request.



Figure 4. ANL's patented Smart Charge Adapter

2. *Electric Vehicle Supply Equipment*: Most of the testing used a normal EVSE with the Smart Charge Adapter, but some others were tested using an experimental, custom EVSE that received cloud-based commands from a custom program (Figure 5). For these tests, the custom EVSE changed the pilot signals for testing. It is worth noting that both the EVSE and the Smart Charge Adapter ran into some problems with the vehicle in performing long, unattended tests. Depending on how the vehicle was designed, sometimes the vehicle would go to a "sleep" mode that required a physical re-plugging in of the J1772 plug. We hope in the future when *ISO 15118 Road vehicles—Vehicle to grid communication interface protocols* is deployed, these types of issues will be eliminated and the charging rates of large fleets of vehicle can be reliably controlled.



Figure 5. ANL's custom-built EVSE with cloud-based controls

3. *Power Analyzer*: The lab has several power analyzers designed specifically for electrified vehicle testing. The most appropriate device is the four-channel Hioki 3390 shown in Figure 6. Each channel monitors a single node of voltage and current in the high and low voltage EV electric circuits. A voltage tap and a current probe is mounted in the EV or the AC wall plug (Figure 7) to sense the power flows. The data logged and/or calculated for each respective node are voltage, current, active and reactive power, integrated current, integrated active power, frequency, and power factor.

All standby idle power consumed (not going to the battery) is accounted for in the “charger” losses model, but the vehicles were instrumented to separate the charge losses from the vehicle standby losses in case in the future that distinction between the two power flows became necessary.



Figure 6. Hioki 3390 Power Analyzer meters (four channels each). The main display shows the values of voltages, current, and power of the selected nodes. The data is logged and saved in csv format, which is then merged with the vehicle CAN data.

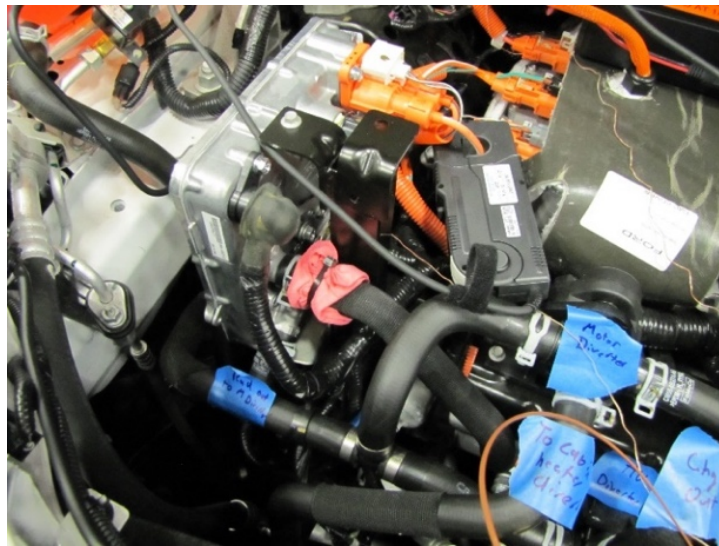


Figure 7. Clamp-on current probe measuring total accessory losses

4. *Charger Command Software*: Edge computing/“Internet of Things” software was used to control the charge rates in the experiments. For the Smart Charge Adapter, existing IBM’s Node-RED Javascript API (see Node-Red N.D.) was used to run the various test sequences. Predefined charger current schedules were developed and loaded into the Node-Red control

software for tests, which lasted from 1 hour to more than 14 hours. To run the Smart EVSE, a Labview program loaded a charge profile file and sent cloud-based commands over the lab Wi-Fi network.

5. *Vehicle Spy*: This commercial CAN bus software/hardware interface system is used to collect important vehicle information from the vehicle's own communication busses. The easiest way to collect this data is to locally log the data with the Vehicle Spy system and then later merge the data with the Hioki-measured power flow data. The most important piece of information from the CAN bus is the vehicle-reported battery SoC. The rest of the information does not include critical measurements but will be very useful in the analysis of the results.
6. *Chassis Dynamometer*: For some of the tests, the vehicles were tested by running an emulated, realistic duty cycle over several days that included chassis dynamometer driving. Data were logged for both driving and then during charging afterward using our data acquisition and control system for the chassis dynamometer. As performed in all our other chassis dynamometer tests, the road load was matched to EPA-listed load coefficients and the EPA test class weight was used. Drive cycles came from "real-world" driving studies (Lee and Filipi 2011). More detail is given later in the test descriptions.
7. *Data Acquisition*: Tests run in the dyno lab used the main facility "host computer" to collect data at 10 Hz. For testing not conducted in the dyno lab, the Hioki power analyzer meter was run in an internal logging mode at 5Hz (in order to reduce file size). The timestamped data were later merged with the Vehicle Spy CAN data for analysis.

1.4 Test Procedures

Various transient tests, as well as simulated charging schedules, were conducted to characterize the physical characteristics of the three EV test articles.

1.4.1 Relevant Standards and Test Methods

There are very few standards available for guidance in test methodology of EV charging efficiency and model parameterization. There are simple concepts to follow in SAE J2841 that make references to charger efficiency. There are other SAE and ISO documents that specify interoperability standards, but again, do not provide test procedure guidance. Good engineering practice was followed to develop test procedures and to control and measure power flows to achieve the goals of the test program. Following are relevant documents to charging and charging interoperability standards:

1. *SAE J1772 Electric Vehicle and Plug-in Hybrid Electric Vehicle Conductive Charge Coupler*: This describes the plug and communication from the EVSE to the vehicle. The pilot signal defined in J1772 will be the primary method of charger power control.
2. *SAE J2847/1 Communication Between Plug-in Vehicles and the Utility Grid*: This SAE Recommended Practice J2847 establishes requirements and specifications for communication between plug-in EVs and the electric power grid, for energy transfer and other applications. Where relevant, this document notes (but does not formally specify) interactions between the vehicle and vehicle operator.
3. *SAE J2894/1 Power Quality Requirements for Plug-in Vehicle Chargers*: There are three main purposes. (1) To identify those parameters of a plug-in EV battery charger that must be controlled in order to preserve the quality of the AC service. (2) To identify those characteristics of the AC service that may significantly impact the performance of the charger. (3) To identify values for power quality, susceptibility, and power control parameters which are based on current U.S. and international standards. These values should be technically feasible and cost-effective to implement into plug-in EV battery chargers.
4. *SAE J2894/2 Power Quality Test Procedures for Plug-In Electric Vehicle Chargers*: This recommended practice provides test procedures for evaluating plug-in EV chargers for the parameters established in SAE J2894/1. A system boundary is established that defines the tested elements and the measurement points.
5. *ISO 15118 Road vehicles—Vehicle to grid communication interface*: This is an international standard defining a vehicle to grid (V2G) communication interface for bidirectional charging/discharging of EVs. ISO 15118 is one of the International Electrotechnical Commission's group of standards for electric road vehicles and electric industrial trucks, and is the responsibility of Joint Working Group 1 (JWG1 V2G) of IEC Technical Committee 69 (TC69) (GMLC 2019a) together with subcommittee 31 (SC31) (GMLC 2019b) of the International Organization for Standardization's Technical Committee 22 (TC22) (Duoba and Fernandez Canosa 2019) on road vehicles. The user-convenient and secure Plug & Charge feature that comes with ISO 15118 enables the EV to automatically identify and authorize itself to the charging station on behalf of the driver to receive energy for recharging its

Actual time	7:00	8:00	9:00	10:00	11:00	12:00	13:00	14:00	15:00	16:00	17:00	18:00	19:00	20:00	21:00	22:00	23:00	0:00	1:00	2:00	3:00	4:00	5:00	6:00
20 mi no work				5, 30min, 5		on charge			10															
Actual time	7:00	8:00	9:00	10:00	11:00	12:00	13:00	14:00	15:00	16:00	17:00	18:00	19:00	20:00	21:00	22:00	23:00	0:00	1:00	2:00	3:00	4:00	5:00	6:00
20 mi no work	on charge			5, 30min, 5		on charge			10	on charge														
Actual time	7:00	8:00	9:00	10:00	11:00	12:00	13:00	14:00	15:00	16:00	17:00	18:00	19:00	20:00	21:00	22:00	23:00	0:00	1:00	2:00	3:00	4:00	5:00	6:00
45 mi no work		15		2.8		2.8	on charge		25	on charge														
Actual time	7:00	8:00	9:00	10:00	11:00	12:00	13:00	14:00	15:00	16:00	17:00	18:00	19:00	20:00	21:00	22:00	23:00	0:00	1:00	2:00	3:00	4:00	5:00	6:00
Deep Discharge		10, 15, 25							15, 25, 40, 15															
		3-5 min pause between cycles					3-5 min pause between cycles																	

Figure 9. Four-day test schedule to emulate typical EV operation

1.5 Experimental Results and Model Validation

1.5.1 Resistance and V_o

The simple equivalent circuit model proved to be sufficient to characterize the EV battery in the simulations. Test data was fed into a custom analysis program that finds the polynomial fits for open circuit voltage (V_o) and resistance (R) as a function of SoC. Within the normal range of SoC, V_o varied some, but R varied very little. The polynomial fit coefficients in the model are stored as an array such that in the future the battery parameters can be modeled as a more complex function or less complex with a linear relationship SoC or even a constant without changing the code, only the coefficient parameters for a given vehicle.

1.5.1.1 Nissan Leaf

The Nissan Leaf, V_o varied by over 50 volts in the test data, the resistance (R) varied very little in the testing. The results from testing are shown in Figure 10.

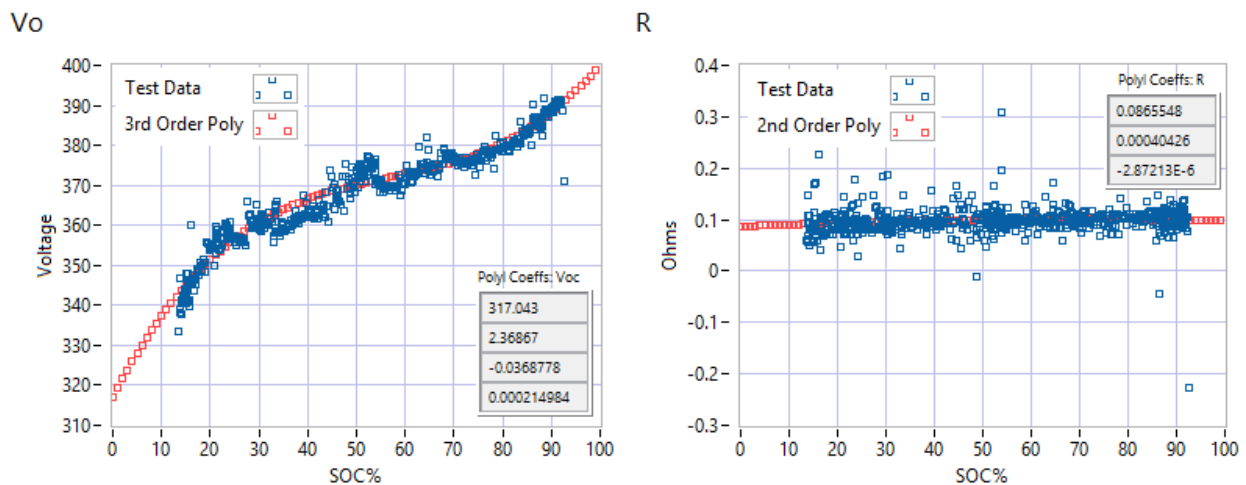


Figure 10. Nissan Leaf open circuit voltage and resistance results from testing

1.5.1.2 BMW i3

The BMW i3, V_o varied by over 80 volts and had a different curve shape compared to the Nissan Leaf, again, the resistance varied very little in the testing. The results from testing are shown in Figure 11.

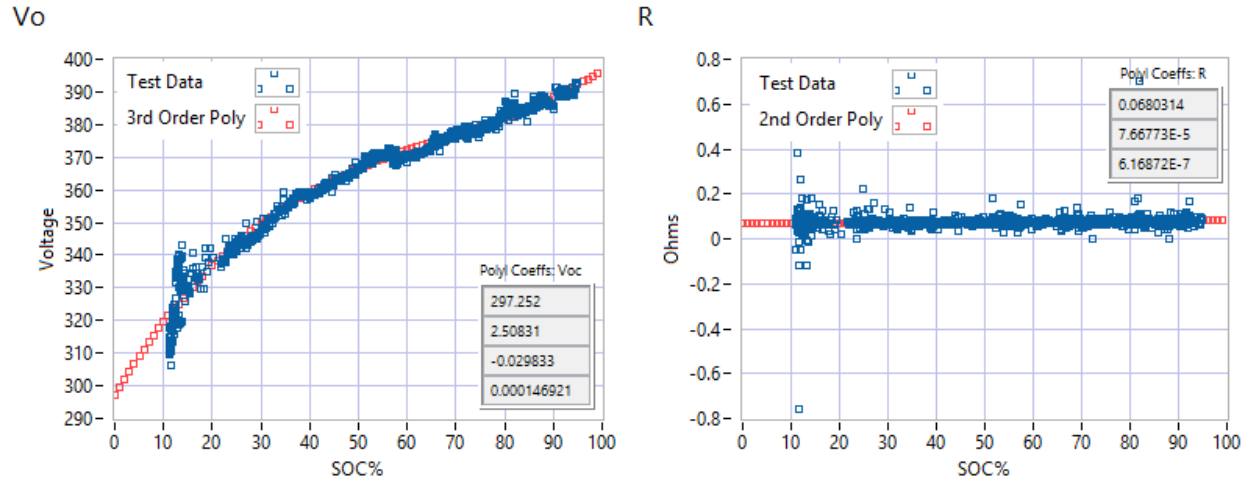


Figure 11. BMW i3 open circuit voltage and resistance results from testing

1.5.1.3 Chevy Bolt

The Chevy Bolt, V_o varied by roughly 80 volts and the resistance varied very little in the testing. The results from testing are shown in Figure 12.

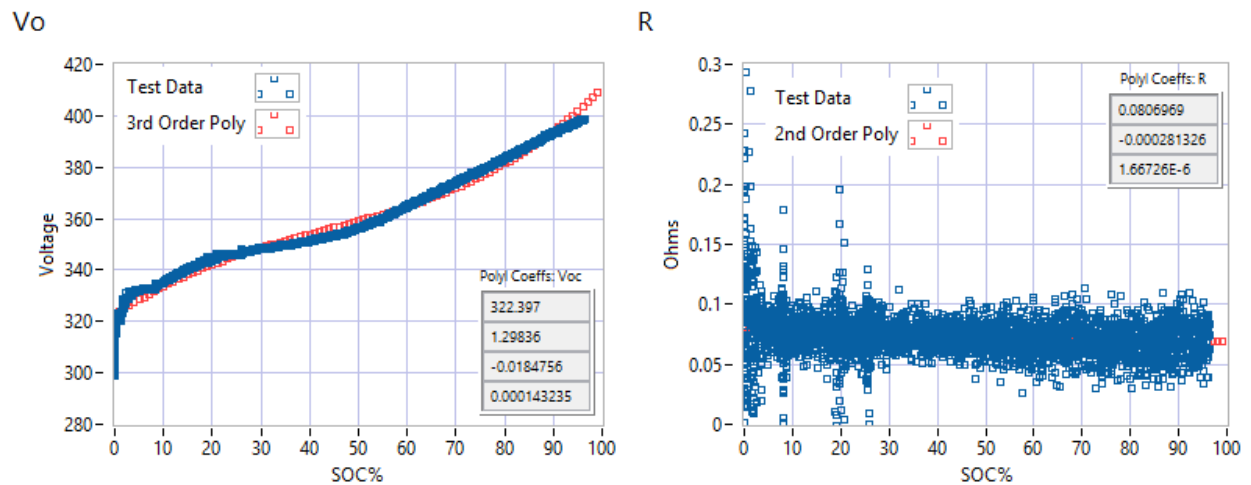


Figure 12. Chevy Bolt open circuit voltage and resistance results from testing

1.5.2 Variable Charge Rate Tests

1.5.2.1 Qualitative Analysis

Although the models describing the physics of the devices proposed in this report were chosen to be as general as possible, some qualitative differences were not captured in the models are seen in the time plots of the transient responses.

1. Time plots

Figure 13 shows selected fragments of the performed transient tests for the three EVs studied. The tests consisted of various step changes in commanded pilot duty cycle, which is read by the vehicle's on-board charger as a current command. In Figure 13, the BMS of the three vehicles appear to loosely track the commanded current in different ways. A prevalent characteristic of the three responses is that the BMS follows positive current increases than negative steps likely for safety reasons (a reduction of power quickly is a protection mode, whereas increasing power is not). Aside from this, the current responses are significantly different for the three test vehicles. The BMW i3 presents the most erratic response when positive requests are commanded: it starts increasing current, then it decreases power for two seconds and goes up again very fast until a first plateau is reached. Finally, after 10–12 seconds, the current raises again until it reached the steady-state with significant steady-state error. On the contrary, the Chevrolet Bolt and the Nissan Leaf present more straightforward responses. In the case of the Bolt, the BMS responds fast with a constant slew rate until it reaches the steady-state for positive requests, while negative requests are tracked almost instantaneously. The Nissan Leaf, on the other hand presents the fastest response, with almost zero lag (a slew rate so fast it is hard to observe with our 5–10 Hz data collection rate) for both positive and negative requests. However, some steady-state error (high) is seen when the requested AC current is 18 A.

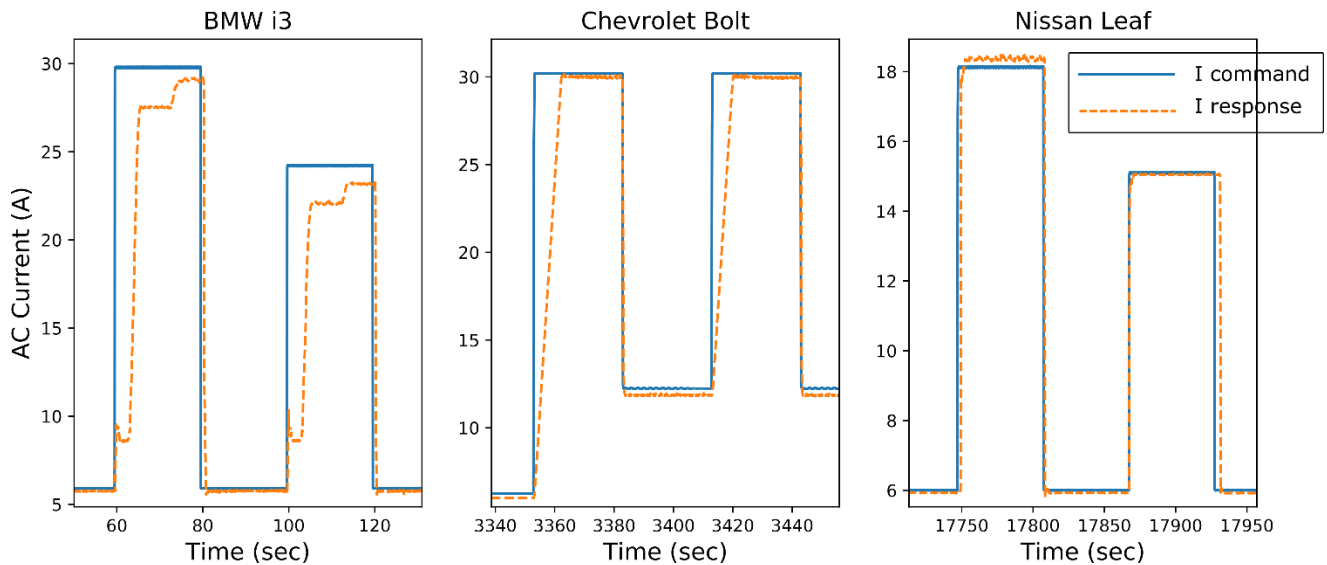


Figure 13. Transient response of the EVs of study. From left to right: MY2014 BMW i3, MY2017 Chevrolet Bolt, and MY2012 Nissan Leaf.

Although the responses differ significantly, a unified mathematical model is proposed to describe the response of the three vehicles of study. Some characteristics, such as the erratic behavior of the BMW i3 for positive requests are not captured in the mathematical models. As the response model will be representing many vehicles, this unified model presents an elegant, common solution while being as precise as possible.

2. State-of-Charge limits

The original model implemented for a fleet of BEVs developed for the February GMLC report (2019a) made an initial assumption that the charger can be turned on/off in 1 second regardless of the battery SoC. Judging from the behavior observed in Figure 13, this assumption is inaccurate and will not capture realistic behavior, at least with respect to the three vehicles used in this testing program.

As shown in Figure 14, a second assumption also in need of addressing is what happens near the end of charge. Therefore, a conservative SoC upper bound must be identified for each vehicle that limits grid service because the response begins to poorly track the request. Although all three vehicles did respond within a reduced charge limit profile, Figure 14 shows that this period is small and not well predicted. Of course, it is not known if the upper bound changes over the life of the vehicle; perhaps parameters like this could be studied in further work.

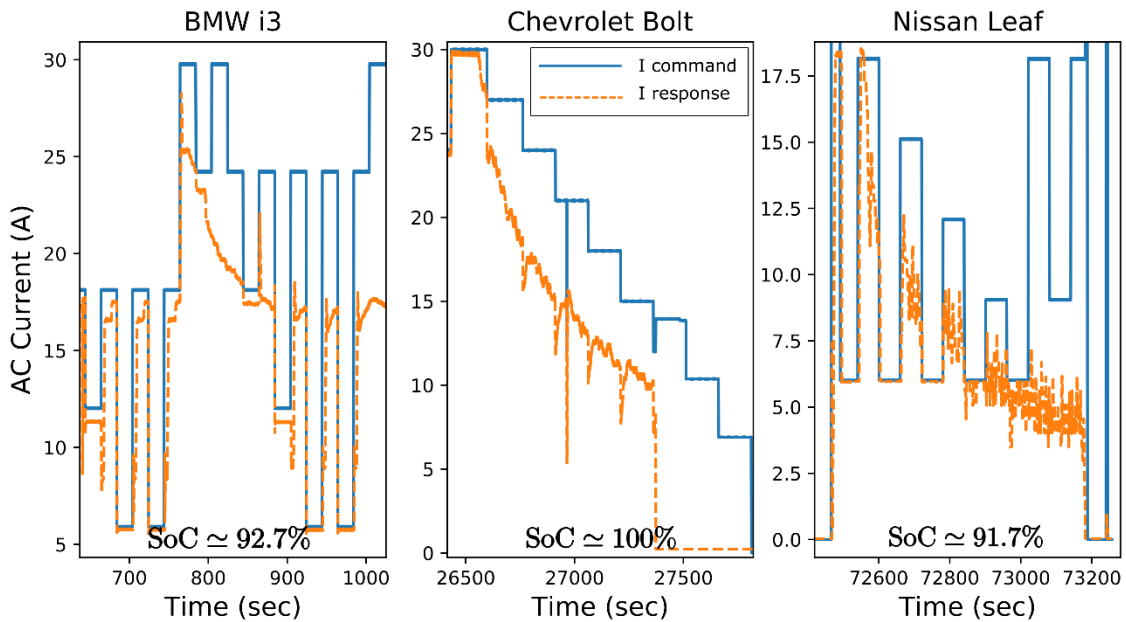


Figure 14. Transient response of the EVs of study when the battery is almost full. From left to right: MY2014 BMW i3, MY2017 Chevrolet Bolt, and MY2012 Nissan Leaf. Note that the request is poorly tracked at the levels of charge presented here.

1.5.2.2 AC-DC Power Losses Results

Once the transient data for each vehicle are collected and processed, the next important model parameter to quantify is the net power losses (the difference between the charger AC power from the plug and the DC power flowing at the battery terminals). Only steady-state power tests were analyzed to find these results. Also, the mathematical model assumes the power losses only depend on the AC charger power, and a second-order polynomial is considered to estimate the power losses as a function of AC power input, see Eq. (8):

$$P_4 - P_1 = \beta_0 + \beta_1 P_4 + \beta_2 P_4^2 \quad (8)$$

Figure 15, Figure 16, and Figure 17 show the experimental data as well as the model results for power losses as a function of the AC charger power at different voltage levels. Note that for the BMW i3 and the Nissan Leaf, only level 2-208 V charging level was tested, whereas for the Chevrolet Bolt, results included Level 1-120 V, Level 2-240 V, and Level 2-208 V charging levels. Tables 2, 3, and 4 include the parameters of the models and the coefficients of determination for the vehicles tested. Note that although there is some spread in the data (likely from temperature and SoC effects), the losses monotonically increase with the AC charger power in an expected manner with high determination coefficients (R^2).

1. BMW i3 REX

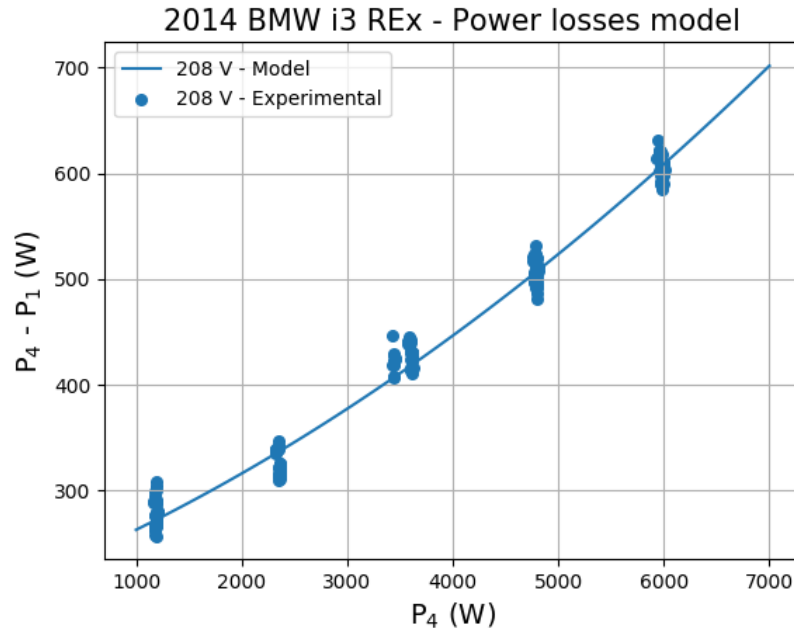


Figure 15. Experimental results and polynomial fitting of AC to DC power losses as a function of the AC power at different voltage levels for the MY2014 BMW i3 REX

Table 2. Parameters of the Power Losses Mathematical Model and Coefficient of Determination at Different Voltage Levels for the MY2014 BMW i3 REX

Model Parameters	Charger Voltage
	Level 2
	208 V
β_0	217.67
β_1	4.13186532e-02
β_2	3.97614852e-06
R^2	0.988

2. Chevrolet Bolt

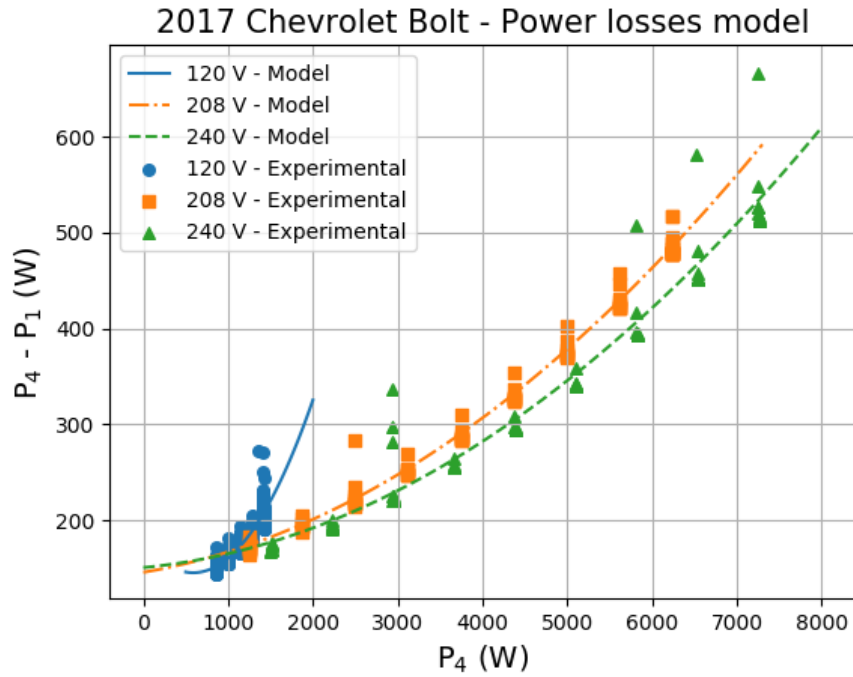


Figure 16. Experimental results and polynomial fitting of AC to DC power losses as a function of the AC power at different power levels for the MY2017 Chevrolet Bolt

Table 3. Parameters of the Power Losses Mathematical Model and Coefficient of Determination at Different Voltage Levels for the MY2017 Chevrolet Bolt

Model Parameters	Charger Voltage		
	Level 1	Level 2	
	120 V	208 V	240 V
β_0	176.61	145.62	150.56
β_1	-1.066e-01	1.498e-02	8.407e-03
β_2	9.047e-05	6.322e-06	6.121e-06
R^2	0.812	0.990	0.941

3. *Nissan Leaf*

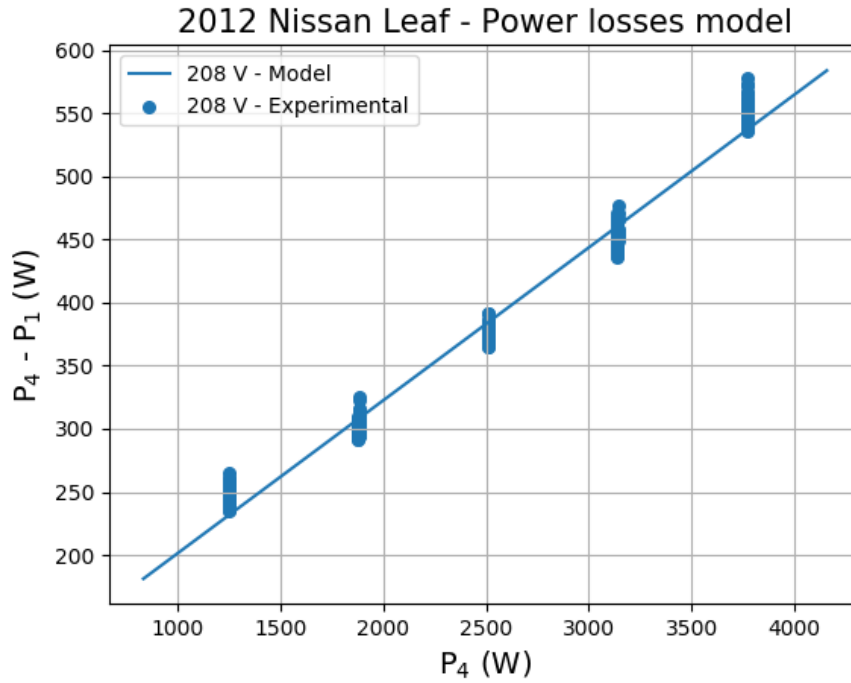


Figure 17. Experimental results and polynomial fitting of AC to DC power losses as a function of the AC power at different power levels for the MY2012 Nissan Leaf

Table 4. Parameters of the power losses mathematical model and coefficient of determination at different voltage levels for the MY2012 Nissan Leaf

Model Parameters	Charger Voltage
	Level 2
	208 V
β_0	80.40
β_1	1.211e-01
β_2	0
R^2	0.987

Figure 18 shows the power losses models of the three vehicles of study obtained from the transient tests data as well as the AC to DC efficiency calculated from the power losses models. As expected, the calculated efficiency of the AC-DC conversion increases until roughly 85%–

95% for the three vehicles of study. Also, the ranking in efficiency follows the vehicles age, it is perhaps unsurprising that the newest vehicles have the lowest losses with charging hardware cost and efficiency improving from year to year.

Because higher charge rates yield higher efficiency, this was taken into account in the initial modeling part specified in the GMLC February report (2019a) to allow the EVs to be always charged at their maximum charge rate. However, the data suggest that reducing the charging rate within an acceptable window of 3 kW to 7 kW can benefit the grid service flexibility without suffering from unnecessary inefficiencies.

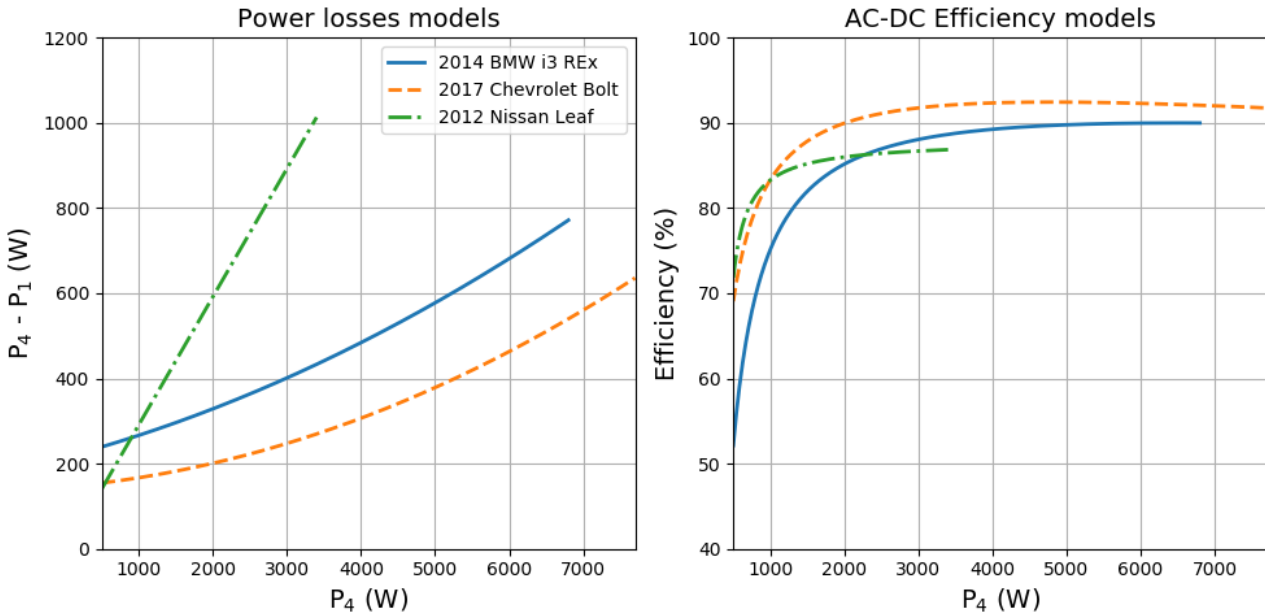


Figure 18. Power losses (left) and AC-DC power conversion efficiency (right) for the three vehicles of study

1.5.2.3 Transient Response Characterization

Figure 19, Figure 20, and Figure 21 represent the experimental data and models for the slew rate as a function of commanded AC charger current at the various voltage levels tested. Table 5, Table 6, and Table 7 include the parameters of the models and the coefficients of determination of the models for the vehicles tested. High R^2 were determined in the three cases.

The BMW i3 and Chevrolet Bolt negative requests are tracked very fast (high slew rate in absolute value), while positive requests are tracked at a slower rate as the magnitude of the request increases. In the case of the Chevrolet Bolt, results for 208 V and for 240 V charging levels are almost identical. On the contrary, the Nissan Leaf (Figure 21) presents a symmetrical slew rate, tracking both positive and negative requests at the same fast rate. The models confirm the assumption introduced in the qualitative analysis shown earlier, that the Nissan Leaf slew rate does not present negative quadratic term that reduces the slew rate for positive requests. Apart from all of these aspects, the experimental results for the BMW i3 and the Nissan Leaf present considerably more variation than the experimental results obtained for the BMW i3,

therefore more variables such as the SoC might affect the response time of the charger for these two vehicles.

1. *BMW i3 REx*

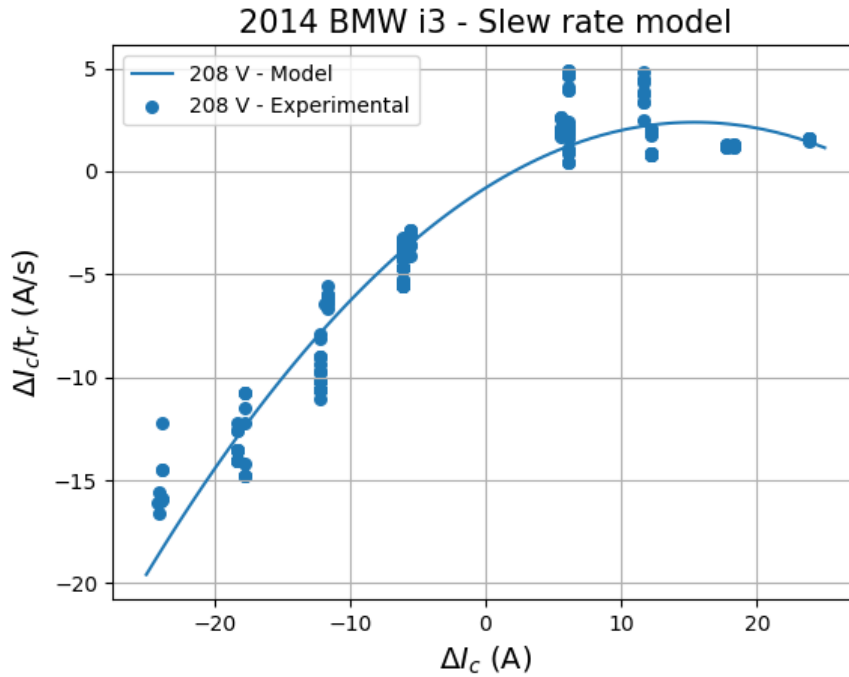


Figure 19. Experimental results and polynomial fitting of slew rate as a function of the variation of the current commanded at different power levels for the MY2014 BMW i3 REx

Table 5. Parameters of the slew rate mathematical models and coefficient of determination at different voltage levels for the MY2014 BMW i3 REx

Model Parameters	Charger Voltage
	Level 2
	208 V
α_0	-0.8084
α_1	0.4144
α_2	-0.01346
R^2	0.928

2. Chevrolet Bolt

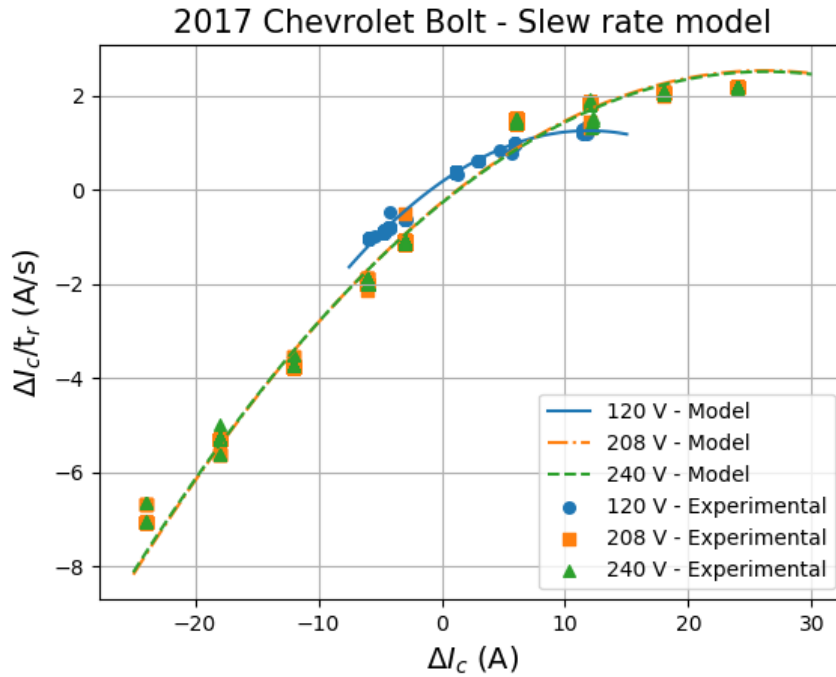


Figure 20. Experimental results and polynomial fitting of slew rate as a function of the variation of current commanded at different power levels for the MY2017 Chevrolet Bolt

Table 6. Parameters of the slew rate mathematical models and coefficient of determination at different voltage levels for the MY2017 Chevrolet Bolt

Model Parameters	Charger Voltage		
	Level 1	Level 2	
	120 V	208 V	240 V
α_0	0.169	-0.266	-0.281
α_1	0.183	0.214	0.213
α_2	-0.007696	-0.004087	-0.004043
R^2	0.996	0.983	0.982

3. *Nissan Leaf*

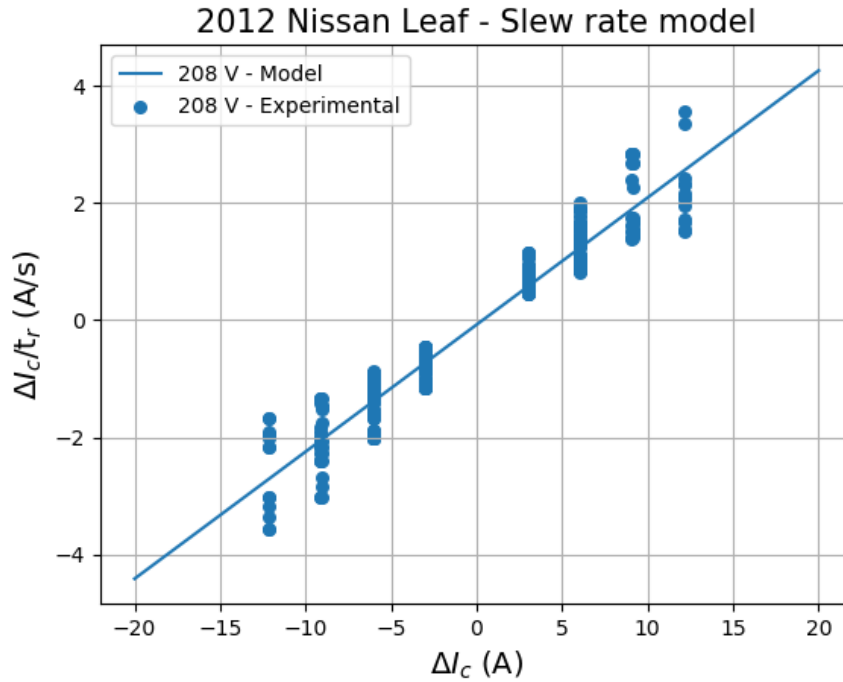


Figure 21. Experimental results and polynomial fitting of slew rate as a function of the variation of current commanded at different power levels for the MY2012 Nissan Leaf

Table 7. Parameters of the slew rate mathematical models and coefficient of determination at different voltage levels for the MY2012 Nissan Leaf

Model Parameters	Charger Voltage
	Level 2
	208 V
α_0	-0.0752
α_1	0.2172
α_2	0
R^2	0.921

We observed (Figure 22) that for decreasing step size in power requests, the response time is practically constant and small; thus, the charge power is tracked very fast. On the other hand, for increased power requests, the response time grows with the requested magnitude for the BMW i3 and the Chevrolet Bolt while for the Nissan Leaf, the response time is constant and very similar

to the one obtained for decreasing power requests. Figure 22 shows the slew rate and the response time models for the three vehicles of study. Although there may be fundamentally different controls methods used by the OEMs in their vehicles to modulate power during a change in current command, this unified slew rate model provides a common method for both positive and negative slew rate responses for all vehicles.

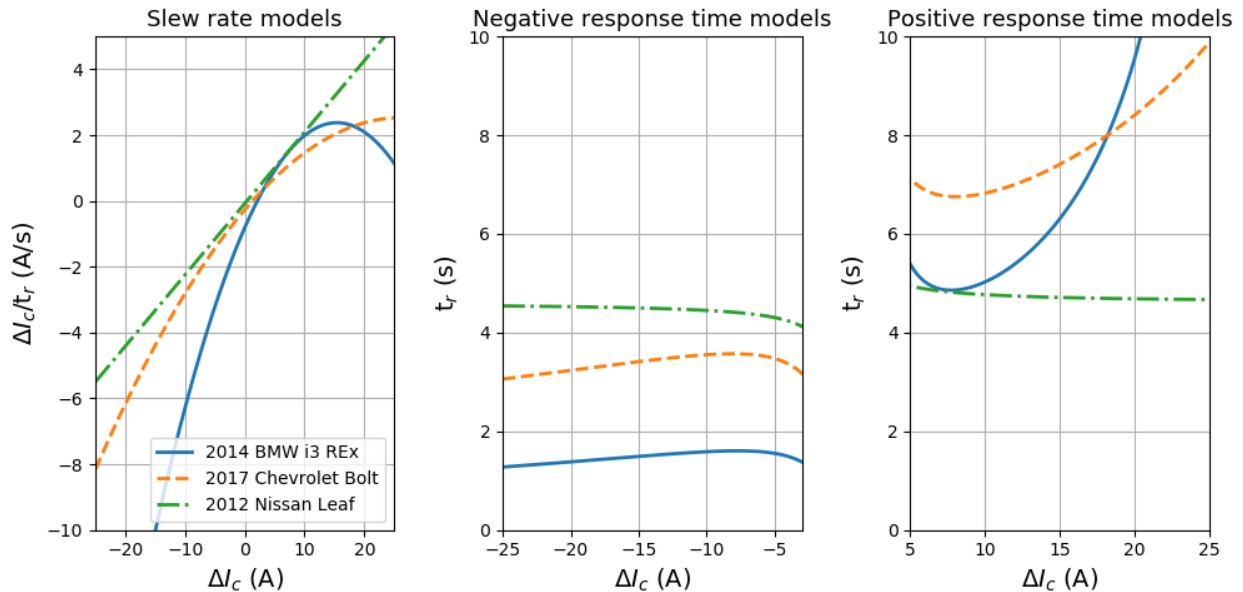


Figure 22. Slew rate (left), negative response times (center), and positive response times (right) models for the three vehicles of study

1.5.3 Dynamometer Driving and Charging Results

Whereas the step change profiles discussed earlier are good to isolate parameters in the model, this test phase represents realistic driving (discharging) and recharge duty cycles that are useful to check the fidelity of the models in a realistic duty cycle. If the models can track SoC, energy, and power over the course of a long, representative duty cycle, then there is confidence that simulation results of actual activity schedules will provide good results.

1.5.3.1 “Real-World” Drive Cycles for Dynamometer Testing

There is much controversy over what is considered “real-world” driving. In this study it is not critical that the cycles be a perfect aggregate of all drivers, but we did want to vary trip lengths and needed cycles that vary their principal characteristics in realistic ways. We found the cycles from University of Michigan to be a citable source to proceed with the chassis dynamometer testing. These cycles have realistic correlations between trip length, stop frequency, and average speed. The speed schedule plots are shown in Figure 23. Notice as the trip length increases, more highway driving style is present.

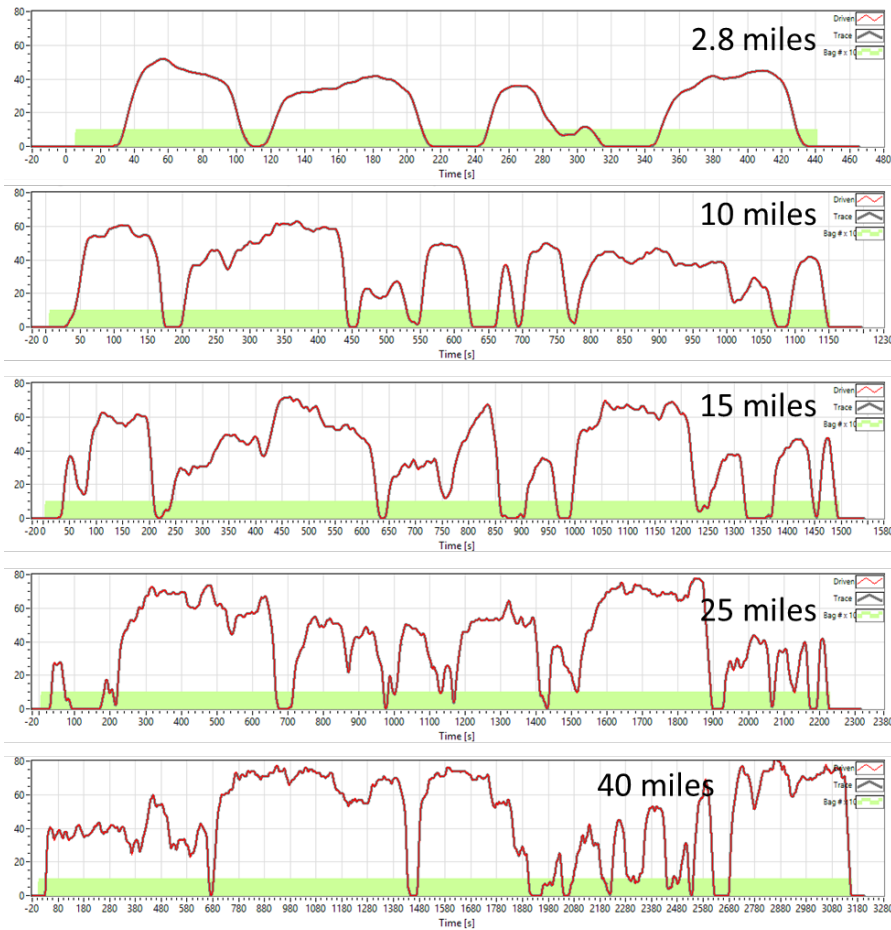


Figure 23. Drive cycles of various lengths from Lee and Filipi (2011) used to determine consumption as a function of average trip speed

1.5.3.2 Energy Consumption Results

Rather than providing one value for vehicle energy consumption rate, more sophistication was desired. However, in the driving portion of the activity schedule of the fleet model, only trip length and distance are known. Thus, we only have a choice of developing a model of consumption as a function of trip length or as a function of average speed. Average speed was found to predict consumption better than trip length. Because of that, a simple linear regression model was found from the data to define the consumption rate as a function of average speed:

$$E_c = a_0 + a_1 \bar{V} \tag{9}$$

Where:

- E_c : is the rate of energy consumption per unit of mile measured in DC Wh/mi
- a_0 and a_1 : are the coefficients of the model from least squares regression of the experimental data collected from chassis dynamometer testing
- \bar{V} : is the average speed of the driving cycle, measured in miles per hour.

Figure 24 shows the experimental results and the models for the three vehicles tested in this testing program, while Table 8 summarizes the parameters of the model and the coefficients of determination compared with the experimental data. As it is expected for a BEV, the energy consumption rate increases with the average speed because of higher losses but also because less regenerative braking is available on higher speed highway driving.

Comparing the different vehicles studied, for a given average speed, the MY2012 Nissan Leaf had the highest energy consumption per unit of distance and the MY2014 BMW i3 REX the least. The reasons for the differences are varied, weight, motor efficiency, aerodynamics, rolling resistance are all factors. Accuracy in these empirical models can then be used to improve the energy tracking of the model presented in GMLC 2019a, GMLC 2019b, and Duoba and Fernandez Canosa 2019.

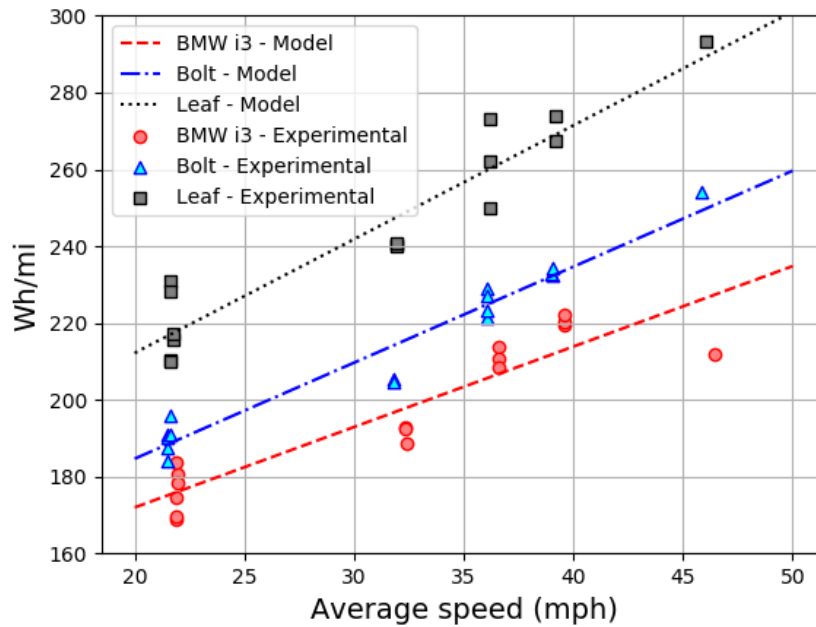


Figure 24. Rate of energy consumption per unit of mile as a function of the average speed for the 2014 BMW i3 REX, 2017 Chevrolet Bolt, and 2012 Nissan Leaf

Table 8. Parameters of the energy consumption models for the 2014 BMW i3 REX, 2017 Chevrolet Bolt, and 2012 Nissan Leaf

Parameter	Vehicle		
	2014 BMW i3 REX	2017 Chevrolet Bolt	2012 Nissan Leaf
a_0	130.133600	134.724745	152.981894
a_1	2.093715	2.498634	2.961289
R^2	0.849625	0.954314	0.905033

1.5.4 Validation Models with Simulations

1.5.4.1 Transient Models

In Section 1.5.1, the transient models of the vehicle chargers for the three vehicles studied were shown. Although some characteristics of the chargers were not completely captured by the models (such as the singularities of the BMW i3 response), the models were intended to conserve the energy and capture the generalities such as the power losses (or charger overall efficiency) and the slew rate (or response time). In this section, we show time plots to compare the experimental DC power response with the modeled DC power response as a function of time.

1. BMW i3

Figure 25 and Figure 26 show the validation results for a particular test sequence applied in the BMW i3 REx. The steady-state power losses present an insignificant error for both negative and positive steps commands. Although, the irregular “double-step” response for the positive commands are not well modeled, this does not severely affect the accuracy of tracking energy and SoC over the course of a long simulation.

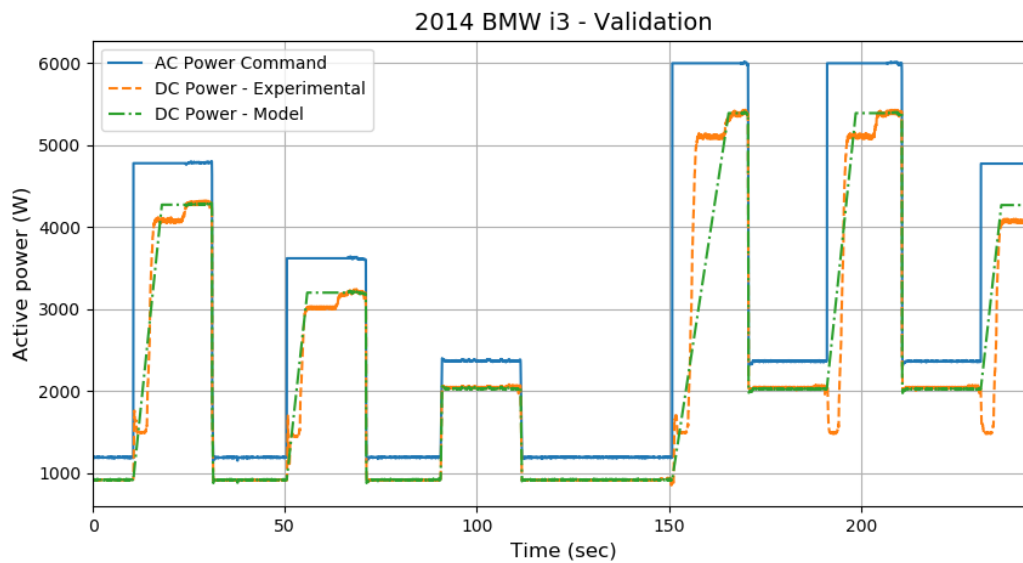


Figure 25. Time plot of the MY2014 BMW i3 REX charger transient model validation: AC power commanded (solid line), DC experimental power (dashed line), and DC modeled power (dashdot line)

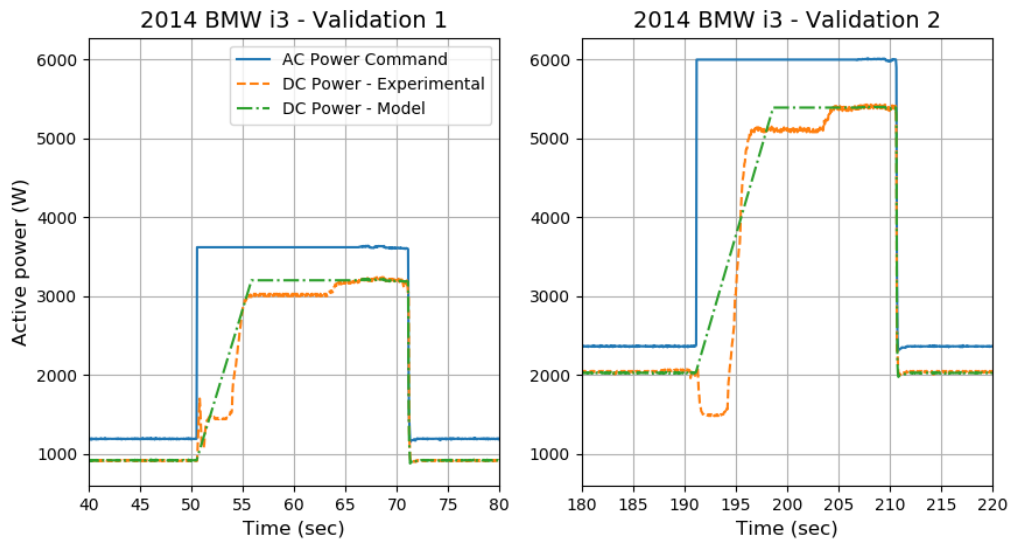


Figure 26. Details of the time plot of the MY2014 BMW i3 REx charger transient model validation: AC power commanded (solid line), DC experimental power (dashed line), and DC modeled power (dashdot line)

2. Chevrolet Bolt

Figure 27, Figure 28, Figure 29, and Figure 30 illustrate the validation results for the Chevrolet Bolt and the Nissan Leaf. In these two cases, the charger responds in a much more predicabile manner and the models perfectly capture both negative and positive steps.

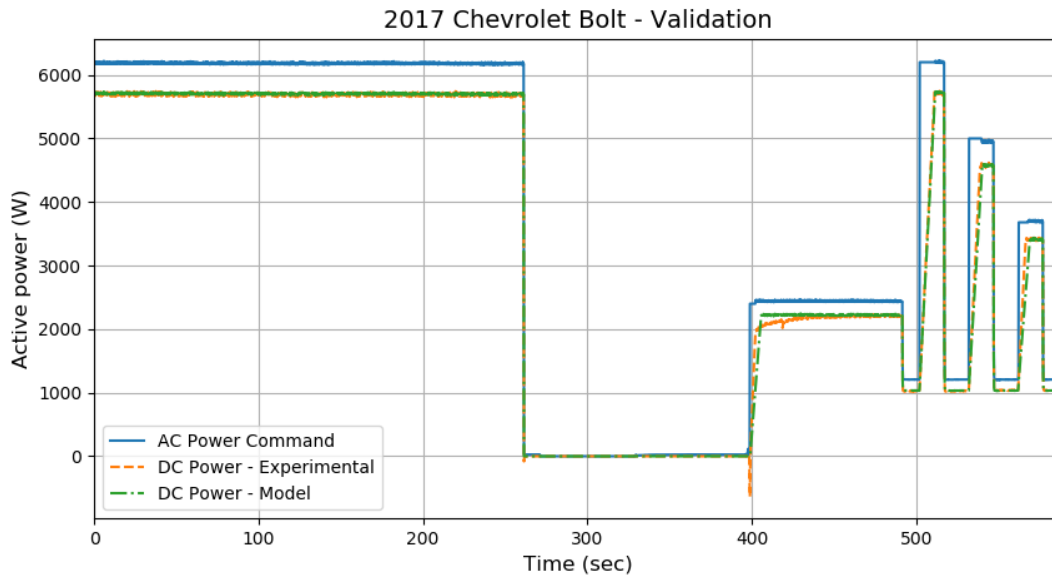


Figure 27. Time plot of the MY2017 Chevrolet Bolt charger transient model validation: AC power commanded (solid line), DC experimental power (dashed line), and DC modeled power (dashdot line)

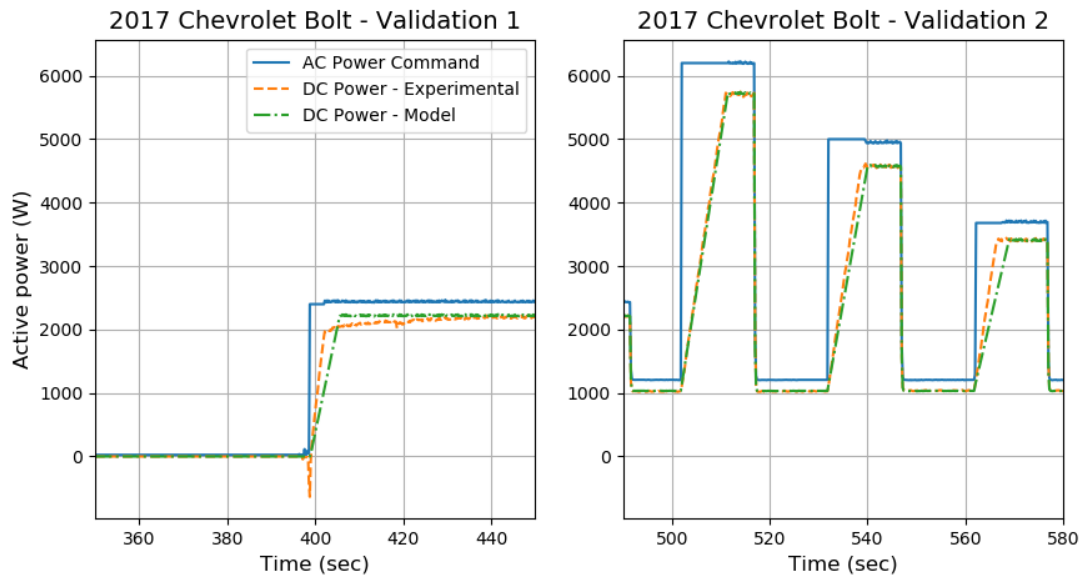


Figure 28. Details of the time plot of the MY2017 Chevrolet Bolt charger transient model validation: AC power commanded (solid line), DC experimental power (dashed line), and DC modeled power (dashdot line)

3. Nissan Leaf

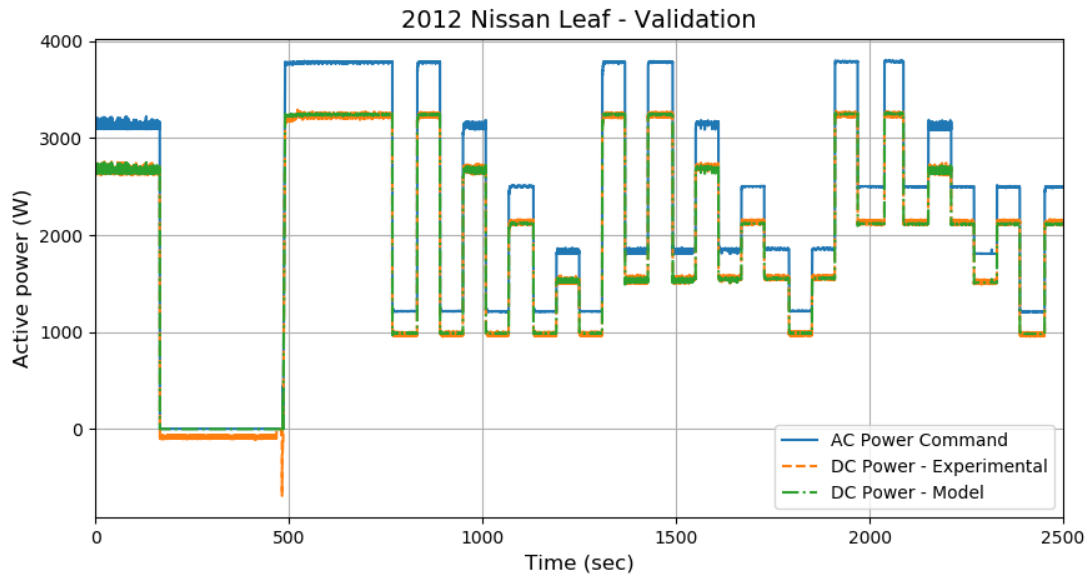


Figure 29. Time plot of the MY2012 Nissan Leaf charger transient model validation: AC power commanded (solid line), DC experimental power (dashed line), and DC modeled power (dashdot line)

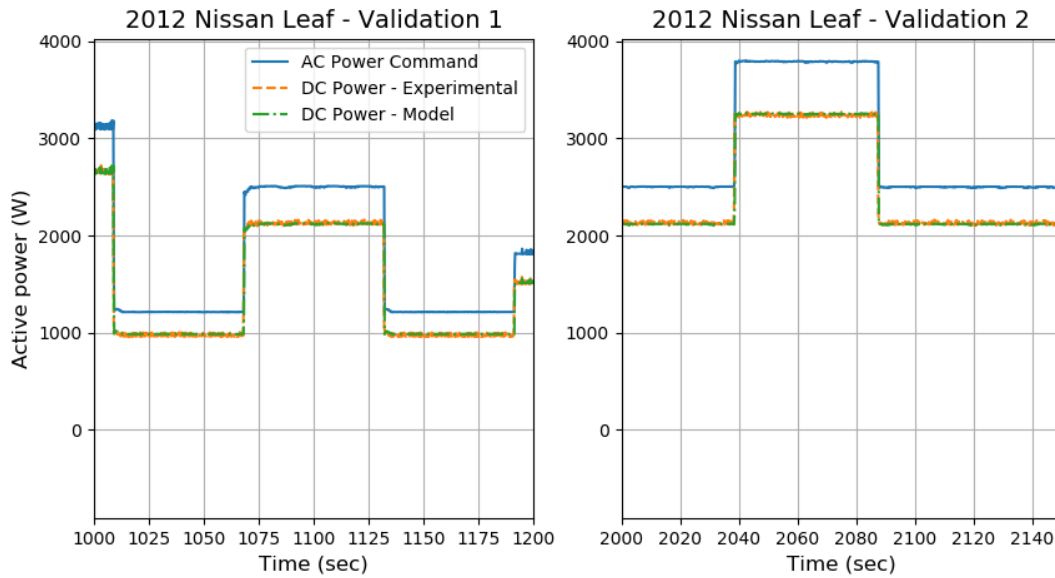


Figure 30. Details of the time plot of the MY2017 Chevrolet Bolt charger transient model validation: AC power commanded (solid line), DC experimental power (dashed line), and DC modeled power (dashdot line)

In order to compare the total charging energy between the experimental results and the models, the DC power is integrated over the entire test (the profile shown in Figure 29 is repeated for 8–12 hours) to see if there is an appreciable difference. As it seen in Figure 31, the total energy is tracked quite well for the three EVs studied in this work and, thus, the models are good representations of actual operation.

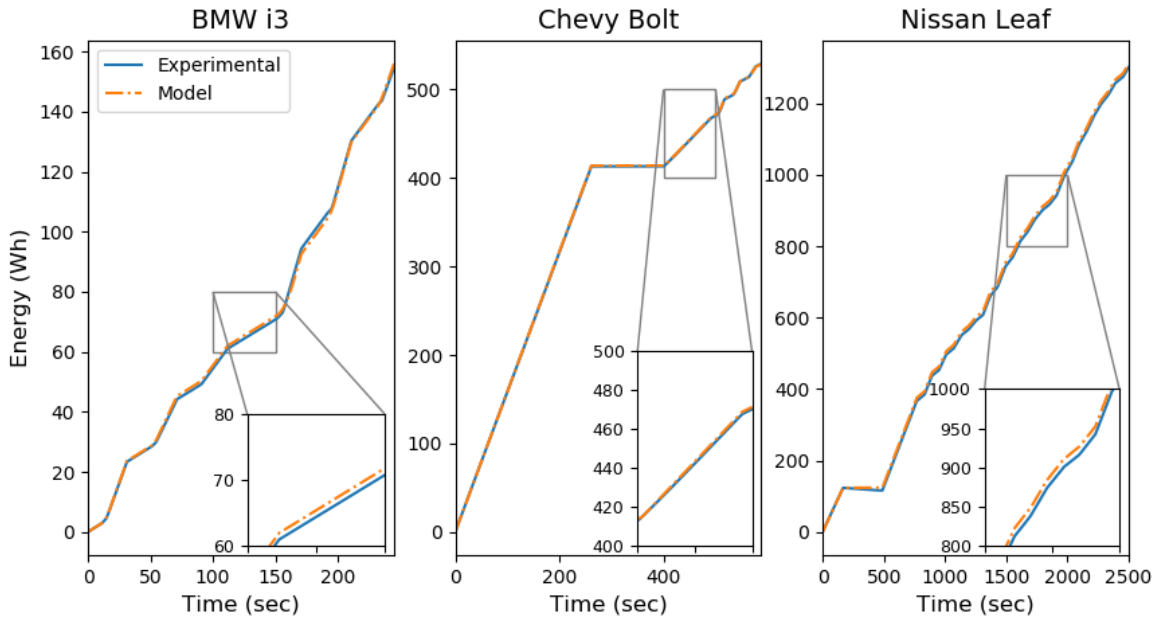


Figure 31. Comparison of charging energy between experimental results and models for the three vehicles studied

1.5.4.2 Discharge (Driving) Models

The other side of energy tracking is the energy consumption per unit distance for of each vehicle while driving as a function of the average speed of the driving cycle. The model proposed does indeed predict the rate of discharge of each vehicle satisfactorily. In order to validate these models, time plots for two particular driving cycles of each vehicle are shown in this section.

Figure 32 shows the experimental and modeled energy consumed as a function of time and the driving cycle for the BMW i3 REx. Although this model clearly does not capture the energy profile during regenerative braking and large accelerations, on average the model accurately predicts the rate of energy consumed for an entire trip. Figure 33 shows the results for the Chevrolet Bolt and, in this case, the results are even better, which corresponds to the coefficient of determination shown in Table 8. Finally, Figure 34 shows the results for the Nissan Leaf. In this case, it presents a larger error in the driving cycle of 5 miles compared with the other two vehicles, and it predicts extraordinarily well the total energy consumed in the 25 miles driving cycle.

1. BMW i3

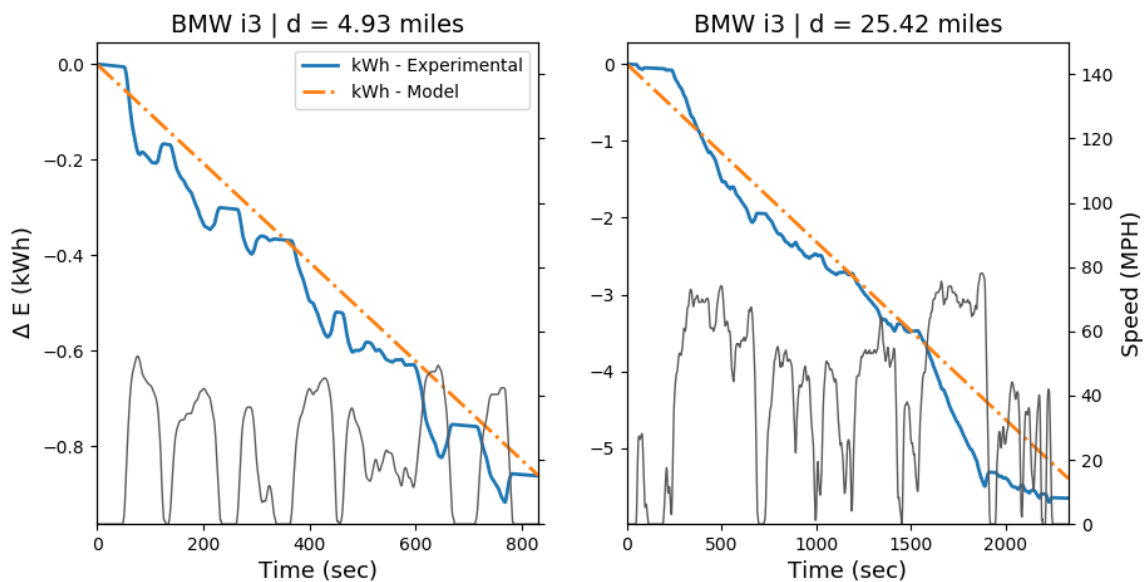


Figure 32. Time plots of the driving cycle and the total energy consumed (experimental and modeled) while driving for the MY2014 BMW i3 REx. A 5 miles driving cycle is shown on the left and a 25 miles driving cycle is shown on the right.

2. Chevrolet Bolt

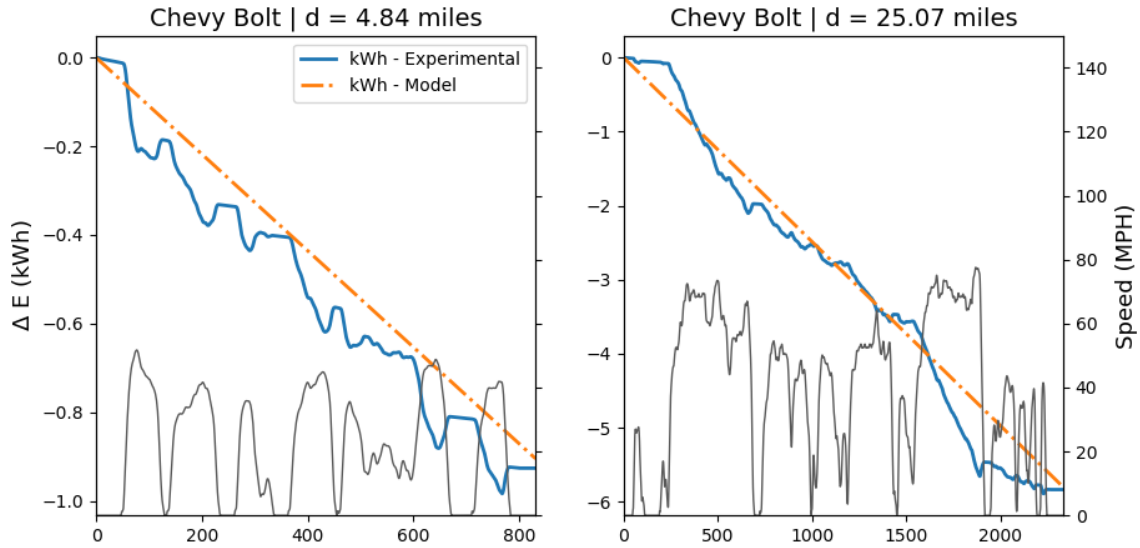


Figure 33. Time plots of the driving cycle and the total energy consumed (experimental and modeled) while driving for the MY2017 Chevrolet Bolt. A 5 miles driving cycle is shown on the left and a 25 miles driving cycle is shown on the right.

3. Nissan Leaf

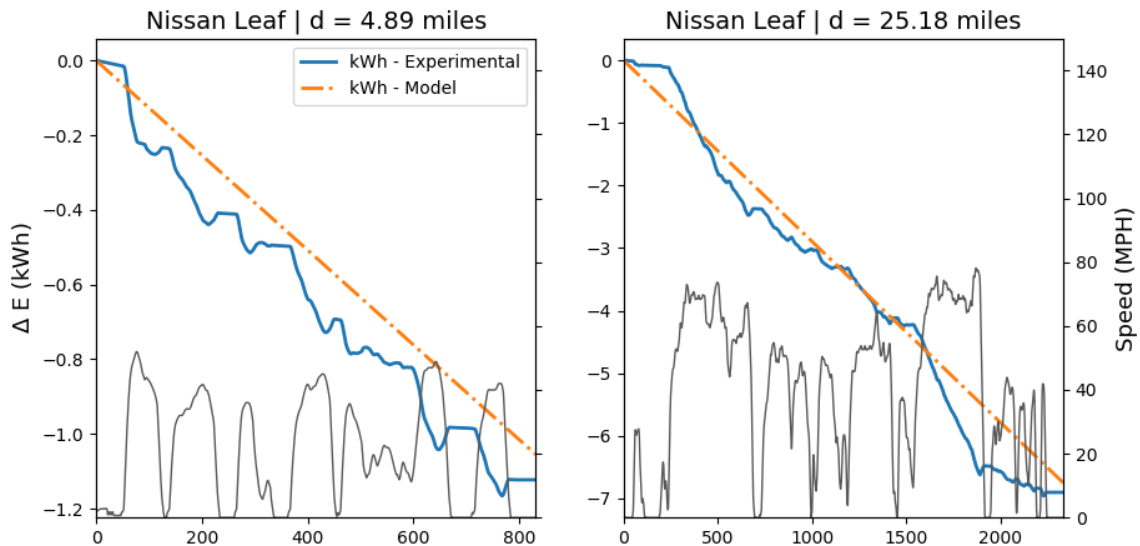


Figure 34. Time plots of the driving cycle and the total energy consumed (experimental and modeled) while driving for the MY2012 Nissan Leaf. A 5 miles driving cycle is shown on the left and a 25 miles driving cycle is shown on the right.

1.6 Conclusions/Observations

We developed a simple, elegant EV model by identifying the relevant parameters needed to account for the physics of a large fleet of EVs simulating an activity schedule of driving and recharging from the grid. The model is designed to provide realistic responses to grid service power modulations by accurately tracking battery SoC and losses. Three EVs from different manufactures with highly varied characteristics were selected for testing. Transient response was added to the original model (GMLC 2019a) and parameters populated from results of data analysis. The models simulated the activities captured in the tests and provided a satisfactory match. We believe that this model could be used to provide realistic behavior of large EV fleet/grid interactions by allowing researchers to find optimized recharge strategies allowing maximum flexibility in grid service requests that help make the grid more reliable and efficient.

This report concludes with a list of notable observations made over the course of the study:

- We were able to efficiently capitalize on the use of various tools, devices, and software infrastructure built by the grid team at Argonne. This allowed the use of more realistic hardware (rather than custom-built experimental setups) that can be used in the near term to control a fleet of EVs for grid service.
- It was also beneficial to use existing Argonne test vehicles because the CAN communication signals have all been decoded and available for logging during testing. These parameters are important for the analysis, the most important of which is the vehicle-reported SoC%.
- Although defining a specific test procedure was not a goal of the study, it is recommended that a charge profile like the one shown in Figure 8 be repeated from zero to 100% of the usable SoC range. The profile captures both the transient response and on/off response throughout the SoC range.
- We experienced some specific challenges of testing vehicles over long periods of time. The equipment used internet-of-things devices and WiFi communication, and sometimes the internet connection would be broken after ~4 hours; we adapted but could not trace the source of the problem. Other times the vehicle that would go to “sleep” in a zero current command state until the vehicle was unplugged and plugged back in. For future testing we will try a modified setup or perhaps move on to use ISO 15118 to control recharging.
- Dynamometer testing was helpful for understanding realistic energy usage in this pilot study, but in the future, vehicle characteristics could be used to estimate the necessary consumption rate as a function of average trip speed using known vehicle parameters and simple EV consumption models. Of course, this approach is confounded when the model includes much more complex plug-in hybrid EV operation.
- We found by analyzing the data that transient behavior most important to characterize was the slew rate. From the perspective of the grid, knowing how fast a large fleet will react to a step change in power levels is most important, and it would be interesting to take another look at this in the future with a fleet of EVs responding together to step change in requested power to observe the aggregate slew rate.
- Informal discussions with other researchers have resulted in a consensus that early designs of EVs were not particularly responsive to J1772 pilot signal changes. As observed in the BMW i3, the on-board charger seemed confused at first by a step increase in recharge current by first dropping the current before ramping it up in steps, eventually

meeting the command. This should not be considered a design flaw; the original purpose of the pilot signal is to ensure the vehicle will not overload the AC circuit, not necessarily to provide continuously variable recharge rate commands.

- The approach of characterizing losses instead of efficiency curves appeared to be the better choice. Indeed, the losses as a function of input power was almost a straight line and thus with limited data, additional vehicle future models could be populated with educated guesses and that do not exaggerate uncertainty at low power levels.

1.7 References

GMLC 2019a. “Grid Services from DER Device Fleets: Volume 1 – Battery Equivalent Models of Device and Fleets.” U.S. Department of Energy draft report by the GMLC 1.4.2. Team. February 2019.

GMLC 2019b. “Grid Services from DER Device Fleets: Volume 2 – Trial Analysis.” U.S. Department of Energy draft report by the GMLC 1.4.2. Team. July 2019.

M. Duoba and A. Fernandez Canosa. 2019. "Mesoscopic Approach to Modeling Electric Vehicle Fleets based upon Driving Activity Data to Investigate Recharge Strategies' Impact on Grid Loads." *2019 IEEE Transportation Electrification Conference and Expo (ITEC)*, Detroit, MI. pp. 1-6. doi: 10.1109/ITEC.2019.8790617.

T.-K. Lee and Z. S. Filipi. 2011. “Synthesis of real-world driving cycles using stochastic process and statistical methodology.” *International journal of vehicle design*, vol. 57, no. 1, pp. 17–36.

Node-RED. N.D. <https://nodered.org/about/>.

Millner, Alan. 2010. "Modeling lithium ion battery degradation in electric vehicles." *2010 IEEE Conference on Innovative Technologies for an Efficient and Reliable Electricity Supply*, pp. 349-356. IEEE.

Part 2

2.0 Electric Water Heaters

National Renewable Energy Laboratory

Chuck Booten

Bethany Sparr

Jeff Maguire

Sivasathya Balamurugan

List of Acronyms

COP	coefficient of performance
DER	distributed energy resource
ERWH	electric resistance water heater
GE	General Electric
GMLC	Grid Modernization Laboratory Consortium
HPWH	heat pump water heater
TRNSYS	Transient System Simulation Tool
WH	water heater

Table of Contents

2.1	Introduction	2.7
2.2	Water Heater Model	2.8
2.2.1	Overview	2.8
2.2.2	Boundary Conditions.....	2.9
2.2.3	Physical Model and Mathematical Representation.....	2.10
2.3	Experimental Hardware.....	2.12
2.3.1	External Controller	2.14
2.4	Test Procedures.....	2.17
2.4.1	Grid Service Tests	2.17
2.4.2	Custom Controls for Improved Grid Services	2.23
2.5	Model Validation.....	2.29
2.6	Conclusions	2.36
2.7	References	2.37

Summary

This report is a deliverable for the Grid Modernization Laboratory Consortium (GMLC) Project 1.4.2—Definitions, Standards, and Test Procedures for Grid Services from Devices. The focus of this project is to develop standard modeling frameworks for various device fleets and grid services, represent these in a standard battery-equivalent format, and demonstrate the potential of these battery-equivalent device fleets to meet advanced grid service needs. This report builds on previous work in this project that developed the battery-equivalent interface and the initial fleet model for electric water heaters. In particular, this report includes additional details related to:

- Experimental characterization of an electric water heater (in electric resistance and heat pump mode)
- Development/improvements to a physics-based model for individual water heater performance
- Comparison between the experimental data and the model.

The experimental characterization provided a means for individual water heater model validation as well as demonstrating capabilities of existing heat pump water heaters (HPWHs). The test article also allowed for the development and characterization of advanced HPWH controls that could be incorporated into the model.

The model development focused on HPWH modeling with a two-node tank. The addition of a two-node tank model is critical for accurate modeling of the performance of the heat pump itself and the complex controls of a HPWH.

Following are summaries of some of the important results from this work:

- HPWHs have the ability to shed load for a period of several hours without preheating under a typical residential draw profile, although preheating reduces the recovery time after the event.
- HPWHs can add load as well, and if the setpoint is reduced in advance of the event, the backup electric resistance elements may be used, which substantially increases the amount of load added without changing the operating mode of the unit.
- Advanced controls can increase the amount of load-add provided, reduce the recovery time after a load-shed event, and can enable more advanced controls such as duty cycling of the heat pump. The duty cycles should have an on time of at least 5 minutes to ensure stable operation of the heat pump, but longer on times (10 minutes or more) will result in more tank heating for the same energy usage.
- The two-node HPWH model shows good agreement with experimental data under a variety of conditions.
- Energy use from simulations matches experimental data adequately and captures transient operation; discrepancies in timing of cycle starts is moderate and a result of simplifications in the modeled control strategy and tank dynamics.

Figures: Part 2

Figure 1. Schematic of a HPWH (Maguire, Burch, Merrigan, and Ong, 2013)	2.8
Figure 2. Example daily hot water events from the Building America Domestic Hot Water Event Schedule Generator compared to the average residential hot water usage	2.9
Figure 3. Schematic of the HPWH model. The tank is split into 2 isothermal nodes, each with a heating element. The lower node is also heated by the heat pump.....	2.11
Figure 4. Low volume draw profile schedule	2.13
Figure 5. Medium volume draw volume schedule.....	2.14
Figure 6. High volume draw profile schedule.....	2.14
Figure 7. GE HPWH with external controls	2.15
Figure 8. Control board and relays for external controls	2.15
Figure 9. Comparison of hybrid mode controls from the original GE controller and the controls implemented on the external controller	2.16
Figure 10. Comparison of electric resistance mode controls from the original GE controller and the controls implemented on the external controller.....	2.16
Figure 11. Setpoint schedules for the morning load shed cases.....	2.18
Figure 12. Setpoint schedules for the midday load add cases.....	2.18
Figure 13. Hybrid Mode: Load Shed Schedules 1A, 1B and 1C. The green shaded band from 4-6am indicates the preheat period and red shaded band from 6-10am indicates the load shed period.	2.20
Figure 14. Hybrid Mode: Load Add Schedules 3A, 3B and 3C. The red shaded band from 6-10am is the deferred heating period and green shaded band from 10am-2pm is the load-add period.	2.21
Figure 15. Electric Mode: Load Shed Schedules 1A and 1C. The green shaded band from 4-6am indicates the preheat period and red shaded band from 6-10am indicates the load shed period.....	2.22
Figure 16. Electric Mode: Load Add Schedules 3A and 3C. The red shaded band from 6-10am is the deferred heating period and green shaded band from 10am-2pm is the load-add period.	2.23
Figure 17. Impact of adding a lower element deadband	2.25
Figure 18. Impact of reduced heat pump deadband during shed event. The shed event is denoted by the red shaded period at the start of the test.....	2.26
Figure 19. Impact of superboost mode during load add event.....	2.27
Figure 20. Impact on tank temperature from the duty cycle tests.....	2.28
Figure 21. Model validation results for the medium use case with default controls.....	2.30
Figure 22. Model validation results for the high use case with default controls.....	2.31
Figure 23. Model validation results for the medium use case with default controls, electric mode	2.32
Figure 24. Model validation results for load shed with preheating.....	2.33
Figure 25. Model validation results for load add with deferred heating.....	2.34
Figure 26. Model validation results for “superboost” mode	2.35
Figure 27. Model validation results for duty cycling.....	2.36

Tables: Part 2

Table 1. Summary Results from Grid Service Tests in Hybrid and Electric Resistance Modes. 2.19

Table 2. Impact of Adding a Lower Element Deadband 2.25

Table 3. Impact of Reduced Heat Pump Deadband During Shed Event..... 2.26

Table 4. Impact of Superboost Mode During Load Add Event 2.27

Table 5. Summary of Duty Cycle Tests 2.28

Table 6. Impact from Duty Cycle Tests 2.28

2.1 Introduction

There is a growing desire to understand the capabilities of various distributed energy resources (DERs) on the U.S. electric grid for providing flexibility in energy usage that could enable increased integration of renewable generation, as well as efficient, low-cost distributed generation. The focus of this GMLC 1.4.2 project is to develop standard modeling frameworks for various device fleets and grid services, represent these in a standard battery-equivalent format, and demonstrate the potential of these battery-equivalent device fleets to meet advanced grid service needs.

This battery-equivalent model is designed to be modular and readily incorporated in grid planning and operational tools. It is simple and generic to use, representing a variety of device types (across the residential and commercial sector) together with only a single, simple dispatch algorithm for each grid service, rather than a custom algorithm for each device class. Such a model is useful for the tools used to plan and design new and modernized grid infrastructure, to operate transmission- and distribution-level grid management/control systems and markets, and to properly account for the roles and functions of DER devices in the future grid.

Developing a unified modeling approach for evaluating the performance of grid services from DER devices is the basis for achieving the project's overall strategic outcomes:

- Enable utilities and grid-operating entities to accurately assess the contribution of DER devices at the planning and operational timescales by using models of their performance that can be incorporated into the tools used to plan and operate the grid.
- Encourage device manufacturers to add the capabilities needed to supply existing and new grid services by clearly articulating the performance characteristics required and by providing a means for evaluating their devices' engineering and economic potential in various regions of the United States.

The efforts detailed in this report are from the third year of the project, related to electric water heater experimental characterization and modeling. The experimental results were used for model validation as well as highlighting potential areas for improvement in device controls. The experiments also demonstrated advanced control strategies that could be used in the future to increase the ability of the water heaters to meet grid needs without impacting comfort, though there may be lifetime impacts if duty cycling or high tank temperatures are used heavily.

The model development described in this report relates to the improved accuracy of electric resistance water heater (ERWH) models developed in the previous two years of this project as well as the development of a two-node heat pump water heater (HPWH) model capable of simulating both existing controls and potential advanced responses to grid needs.

2.2 Water Heater Model

2.2.1 Overview

We simulated two different water heating technologies: an electric resistance water heater (ERWH) and a heat pump water heater (HPWH). The ERWH model has been described in detail in the previous year's report (Pratt et. al. 2019). For the ERWH, the storage tank model consisted of a single, isothermal node. HPWHs are considerably more complex than ERWHs. They feature an integrated heat pump that pulls heat from the ambient air and adds it into the bottom half of the tank, with the heat pump performance depending on the ambient air wet-bulb temperature and the temperature in the bottom half of the tank. In addition, HPWHs also feature backup electric resistance elements (see Figure 1 for a schematic of a typical HPWH), one near the top and one near the bottom. Although the heat pump is more efficient than the elements (with typical coefficients of performance [COPs] in the range of 2–4), it has a lower capacity (1–2 kW) and adds heat to the bottom of the tank. The backup electric resistance elements have a much higher capacity (typically in the range of 4–5.5 kW for residential water heaters) but lower efficiency (COP=1).

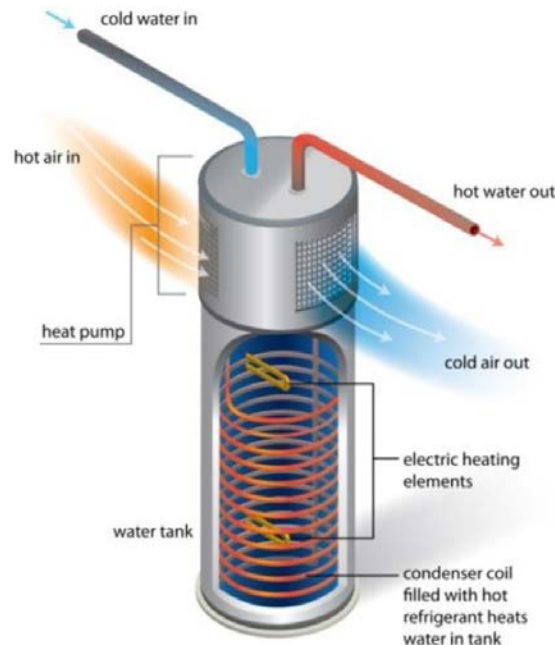


Figure 1. Schematic of a HPWH (Maguire, Burch, Merrigan, and Ong 2013)

This additional complexity of multiple heat sources, performance depending on the water temperature in part of the tank, and the control logic that dictates which heat source is used necessitates a model with multiple nodes. Traditionally, HPWHs have been modeled using 1D models with multiple nodes (12 is a common assumption) to capture stratification, which affects the control logic and the heat pump performance. However, multiple node models can require long run times because of iteration between the control logic and the tank node temperatures. For these grid-level models, we utilized a simplified two-node approach to model the performance of the HPWH.

2.2.2 Boundary Conditions

In order to model water heaters, a few key boundary conditions also need to be modeled. These include the hot water draw profile, the incoming mains water temperature, and the ambient air temperature and humidity (for HPWHs).

Because this project focused on residential electric water heaters, the usage patterns considered here are consistent with “typical” residential hot water usage and would not apply to most commercial buildings. The residential draw patterns used here were developed using the Building America Domestic Hot Water Event Schedule Generator (Hendron, Burch, and Barker 2010). This tool creates a full year of discrete hot water usage events for each end use typically found in a home: showers, baths, sinks, clothes washers, and dishwashers. Showers, sinks, and baths are treated as mixed water use events, where the homeowner tempers the hot water with mains water to reach a useful temperature of 110°F, as specified in the latest version of the Building America House Simulation Protocols (Wilson et al. 2014). Clothes washers and dishwasher draws are treated as hot-only events, where all the water drawn comes directly from the water heater. The discrete events, when averaged over a whole year, match the typical hot water usage pattern for each end use. Draw profiles include weekday and weekend variation in hot water use and two weeks of vacation per year. An example day of hot water usage and the average residential net hot water usage (across all end uses) are shown in Figure 2.

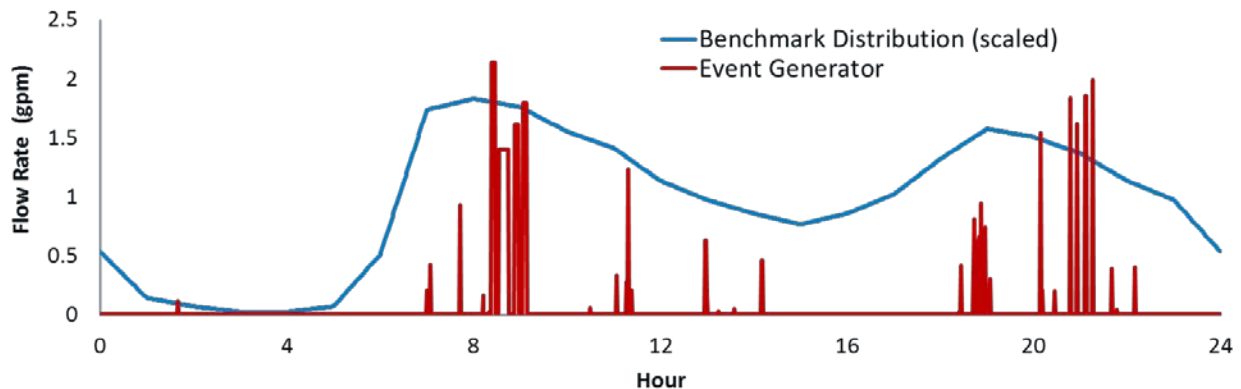


Figure 2. Example daily hot water events from the Building America Domestic Hot Water Event Schedule Generator compared to the average residential hot water usage

An algorithm for determining the mains water temperature as a function of climate was used for incoming water temperature (Burch and Christensen 2007). This algorithm predicts a smooth, sinusoidal mains water temperature based on monthly average outdoor air temperatures. It has become the de facto standard for calculating incoming cold water temperatures, having been adopted by major building energy simulation engines (EnergyPlus® and TRNSYS) as the default. Ambient air conditions (temperature and humidity) were determined by running annual whole building simulations using [BEopt™](#) and EnergyPlus, then exporting the resulting ambient conditions for each zone in which the water heater can be located. This approach ignores the potential impact of the water heater on the space conditions (which can be particularly impactful for HPWHs) but provides reasonable inputs for this water-heater-focused project. In terms of the installation location in the home, 67% of water heaters are assumed to be installed in unconditioned space and 33% are installed in conditioned space. “Unconditioned space” varies

by climate, with warmer climates installing in the garage and colder climates in the basement (if present).

2.2.3 Physical Model and Mathematical Representation

For ERWHs, a single node is sufficient to simulate the performance of the water heater, because the performance of the electric elements is less dependent on tank stratification. The fundamental equation governing the performance of the water heater is an energy balance on the tank. The energy balance is:

$$m_{tank}c_p \frac{dT}{dt} = Q_{loss} + Q_{del} + Q_{heat}$$

The individual heat flow terms are calculated as:

$$Q_{loss} = UA \cdot (T_{tank} - T_{amb})$$

$$Q_{del} = m_{draw} \cdot c_p \cdot t (T_{tank} - T_{mains})$$

$$Q_{heat} = \eta_{heat} \cdot E_{cons}$$

At each timestep, the heat removed from the tank because of tank losses and draws are calculated. If enough heat is removed for the tank temperature to fall below the water heater setpoint minus the deadband, the element will turn on. The element will stay on over multiple timesteps until the setpoint temperature is achieved (and, if necessary, operate for part of the timestep to avoid overshooting the setpoint). Specific controls and response during a request for grid services are described below.

To model a HPWH, a two-node approach to modeling the tank was developed to account for the complexity of a HPWH. A schematic representation of the two-node approach is shown in Figure 3. Each node is modeled as accounting for half of the total volume of the tank. Each node can be heated by a separate electric resistance element and the lower node can also be heated by the heat pump.

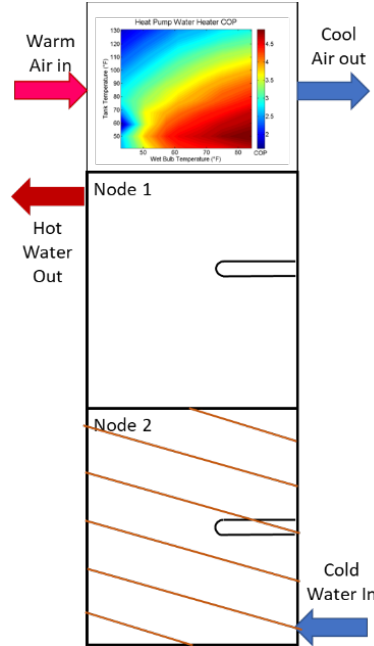


Figure 3. Schematic of the HPWH model. The tank is split into two isothermal nodes, each with a heating element. The lower node is also heated by the heat pump.

For the two-node approach, the same overall energy balance dictates the performance of the entire water heater. However, for this case, the heat balance for each node is expanded to include conduction between nodes:

$$m_{node}c_p \frac{dT}{dt} = Q_{loss,node} + Q_{del,node} + Q_{heat,node} + Q_{cond}$$

The individual heat flow terms are calculated as:

$$Q_{loss,node} = U \cdot A_{node} \cdot (T_{node} - T_{amb})$$

$$Q_{del} = m_{draw} \cdot c_p \cdot t (T_{n1} - T_{mains})$$

$$Q_{heat} = \eta_{heat} \cdot E_{cons}$$

$$Q_{cond,n1-2} = \frac{k_{water} \cdot A_{top}}{d_{nodes}} \cdot (T_{n1} - T_{n2})$$

Heat losses are calculated in the same manner, but now reflect the node surface area rather than the entire tank. Delivered energy is calculated in a similar way but reflects that the outlet temperature is the upper node temperature. When a flow occurs, it is necessary to determine whether that flow impacts the upper or lower node. To do this, an empirical “flow fraction” was simulated as part of this model. This flow fraction represents how much of the incoming cold water goes to the lower node out of the total flow from the tank. During times when the lower node temperature is higher than the mains water temperature, the flow fraction is 0.95, reflecting that most of the cold water goes into the bottom of the tank. If the bottom node temperature reaches the mains water temperature (indicating that a large draw has occurred and that the tank

has not yet recovered), then the flow fraction is set to 0 and all flow goes to the top node. The high flow fraction (used most of the time) captures the small amount of mixing that occurs between nodes because of draws, while the change once the bottom node is sufficiently depleted captures situations where the thermocline in the tank has moved into the upper node. Heat is added to the tank in the same way as the ERWH case, but the efficiency of the heat pump now varies. The conduction equation shown here is for heat transferred from node 1 to node 2.

One of the most complicated things to model for HPWHs is the control logic. The physical HPWH used for the laboratory portion of the project uses only one temperature measurement near the top of the tank to determine the operating mode of the HPWH. The controls also consider the rate of change of temperature in determining which heat source to use. In simulation, the node volume is large, so the rate of change is not a good prediction variable. Instead, a setpoint-based control logic was derived from the laboratory testing, assuming that the model has setpoints based on both the upper and lower node temperatures. This assumes direct measurement of the lower node temperature rather than inference based on the rate of change of temperature in the upper half of the tank, but performs a similar function of dispatching the element(s) when the heat pump is unable to keep up with the load. During hybrid mode, the heat pump always turns on first. If the heat pump is unable to keep up with the load, the HPWH will then transition to the lower element. If temperature drops even further, the upper element will turn on, then it will transition back to the lower element. If the heat pump comes on, it will remain on until either the tank is back at setpoint or the lower element is triggered. Once the lower element comes on, the heating cycle will be completed by that element (and the upper element, if triggered) without ever reverting to the heat pump.

This control logic was derived based on several of the lab tests described later in this report and was found to reasonably predict the water heater control logic. Validation results of the model are presented in Section 2.5.

2.3 Experimental Hardware

The laboratory portion of this project included a modified GE HPWH (model GEH50DFEJSRA), as shown in Figure 7. The following sensors were installed to monitor the performance of the HPWH:

- Real and reactive power meter
- Inlet and outlet air temperature and relative humidity sensor
- Inlet and outlet water temperature thermocouples
- 11 internal tank temperature thermocouples
- Water flow meter on outlet
- Surface-mounted temperature measurement next to upper resistance element (adjacent to temperature sensor used by GE control board for control).

In order to simulate usage of the water heater, a solenoid valve and variable control valve were installed on the outlet of the water heater. The variable valve was used to control flow rate and the solenoid valve actuated the draws. Both valves were controlled by the laboratory's data acquisition system and could be set to run on schedules developed to mimic different types of users.

Three draw profiles with different hot water usage levels were defined using the Domestic Hot Water Even Schedule Generator (Hendron, Burch, and Barker 2010), with daily hot water draw volumes close to the means of the clusters from domestic hot water field research (Lutz 2012). The three schedules, shown in Figure 4– 6, were: low (28.5 gallons), medium (69.5 gals), and high (97.8 gals). These schedules were used to study the GE controls and to run the 24-hour tests described below.

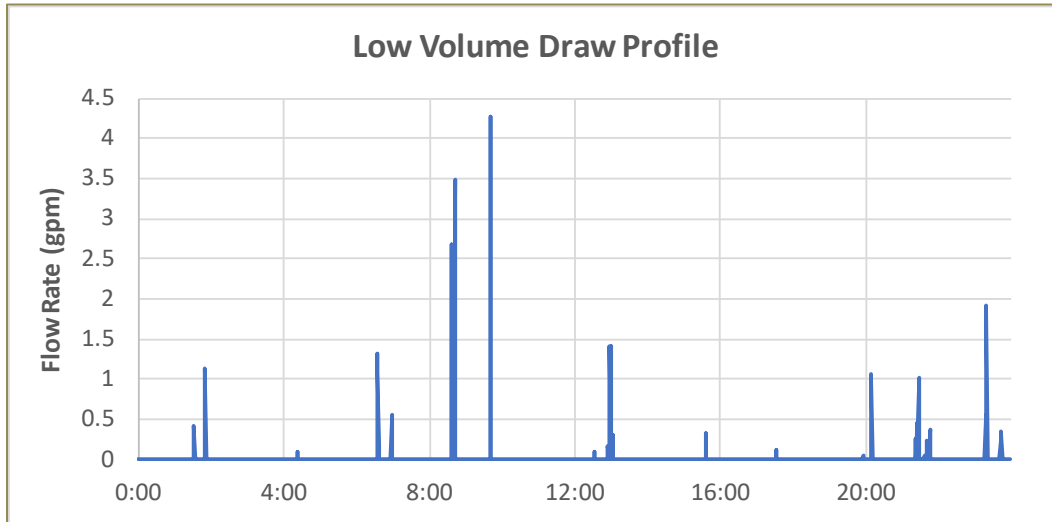


Figure 4. Low volume draw profile schedule

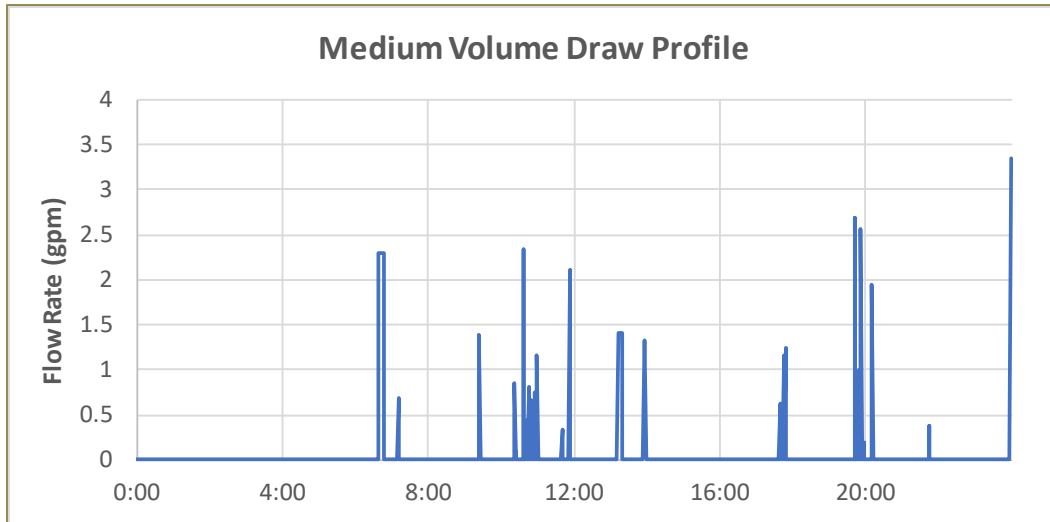


Figure 5. Medium volume draw volume schedule

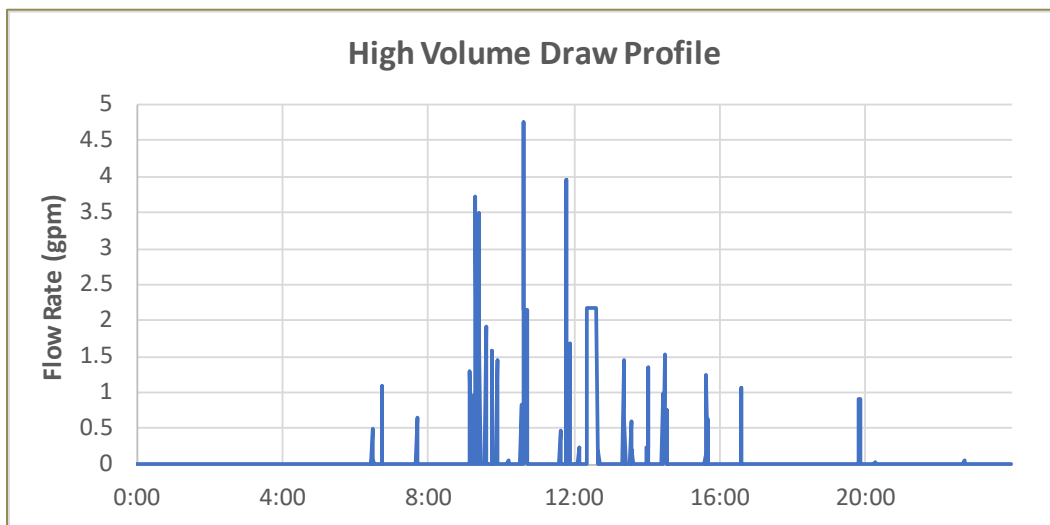


Figure 6. High volume draw profile schedule

2.3.1 External Controller

The water heater’s controls were modified to allow external control of the water heater. In the first set of tests (Section 2.4.1), the ability to change the water heater’s setpoint on schedule was needed to impose simple demand response commands. The second set of tests (Section 2.4.2) included some changes to the basic controls to improve the response to load-add and load-shed demand response commands. The controls included simple actions such as changing the setpoint on a schedule as well as more complex controls such as duty cycling the heat pump.

In order to replicate the controls, the HPWH was run in hybrid mode (using the heat pump and the back-up electric elements) and electric resistance mode across the three draw profiles (Figures 4-6) using the onboard controller. Data from those runs were used to approximate the controls that dictate when the heat pump turns on and when the backup elements turned on when

operating in hybrid mode. The electric resistance mode controls were also approximated based on the data collected from in this phase.



Figure 7. GE HPWH with external controls



Figure 8. Control board and relays for external controls

An external controller was installed with a set of relays that allowed the water heater to switch back and forth between the GE control board and the custom controls on a BeagleBone single-board controller, as shown in Figure 8. The same tests performed with the GE controller were repeated using the external controller. Comparisons between the water heater's behavior with the GE controller and the external controller are shown for hybrid mode (Figure 9) and electric resistance mode (Figure 10), both running with the medium use draw profile.

In hybrid mode, when the GE controller was used, 6.21 kWh were used over the course of the day, versus 5.96 kWh with the external controller, which corresponds to a difference of 4%. Despite the agreement in overall energy use, the timing of the heat pump and electric elements is different between the original GE controller and external controller, mostly because of slight differences in initial conditions and small variations in the draw profiles. The first draw was slightly bigger in the custom controls test, which led to the heat pump operating longer in that case. In the GE control case, the heat pump did not run as long after the first set of tests, which meant the tank was colder after another large draw, causing the upper element to come on earlier in the day than in the custom control case. In electric resistance mode, the GE controller resulted in 14.94 kWh for the day, versus 15.07 kWh with the external controller, which is less than a 1% difference. Similar to the hybrid mode tests, slight differences in initial conditions and draw volumes led to differences in timing for the elements, even though the overall energy use between the custom controller and GE controller was nearly identical.

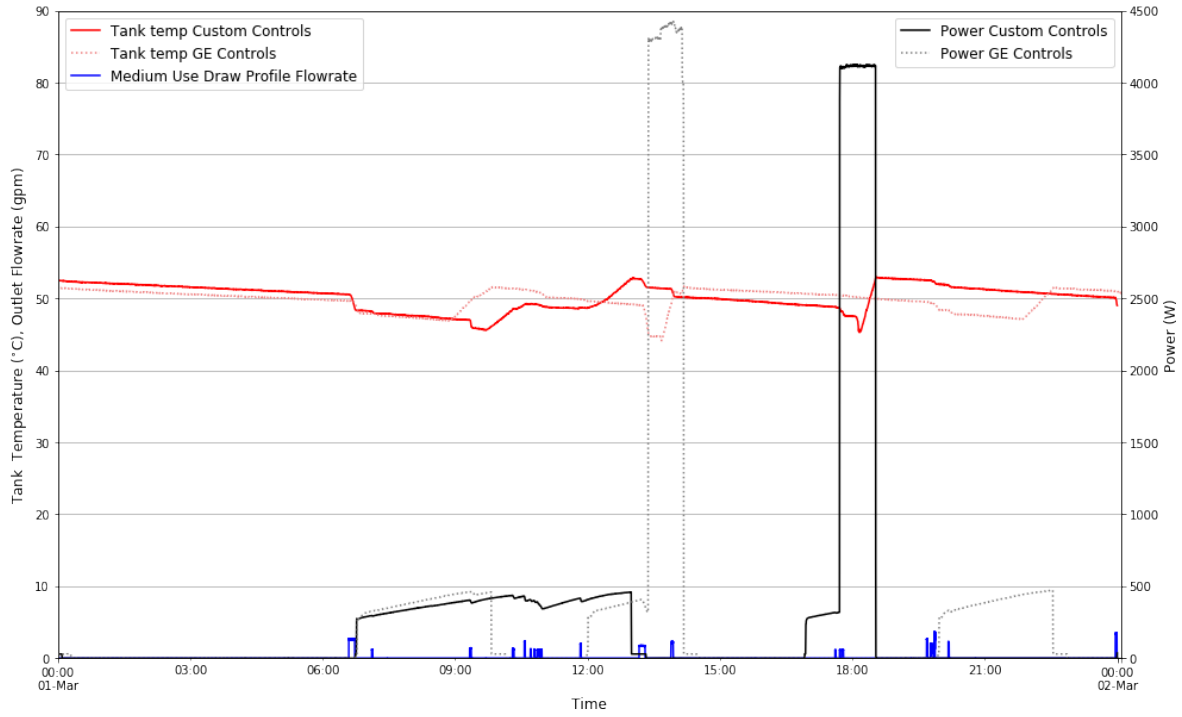


Figure 9. Comparison of hybrid mode controls from the original GE controller and the controls implemented on the external controller

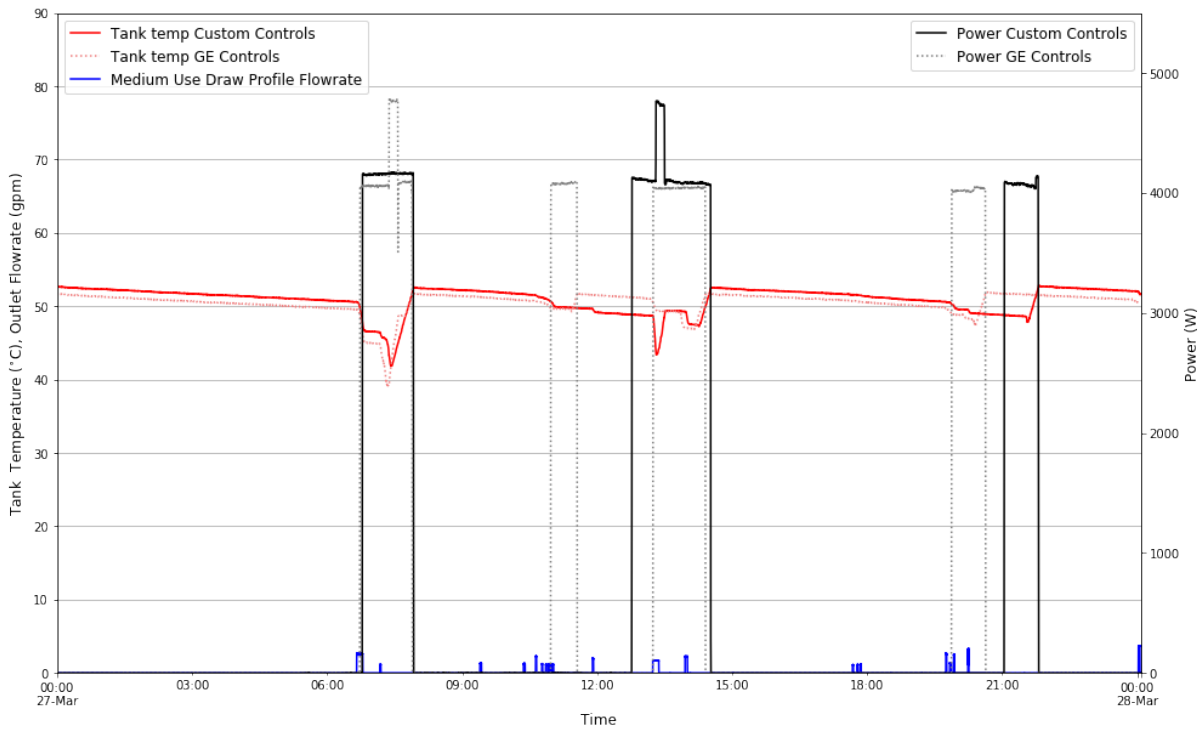


Figure 10. Comparison of electric resistance mode controls from the original GE controller and the controls implemented on the external controller

Despite some temporal variation in when heating elements were used, the performance of the external controller matched the GE controller well enough to move forward. All of the tests described in Sections 2.4.1 and 2.4.2 were performed using the external controller.

2.4 Test Procedures

2.4.1 Grid Service Tests

A series of four grid service use cases were identified: morning load shed, late afternoon load shed, midday load add, and midnight load add. A setpoint schedule was used to define the load add and load shed events: a load add event was accomplished by raising the setpoint and a load shed event was accomplished by lowering the setpoint. Each use case also included a more advanced case in which the setpoint was adjusted in preparation the event (preheating before a load shed, or deferred heating before a load add).

Because of the amount of time that would have been required to run through all the grid service use cases, a subset of use cases was tested: the morning load shed and midday load add cases with the medium draw profile. The hybrid mode tests included both the base load shed and load add cases (setpoint only adjusted during the event time) and the more advanced load shed and load add schedules that include preheating or deferred heating, respectively. The electric mode tests only included the more advanced load shed and load add cases.

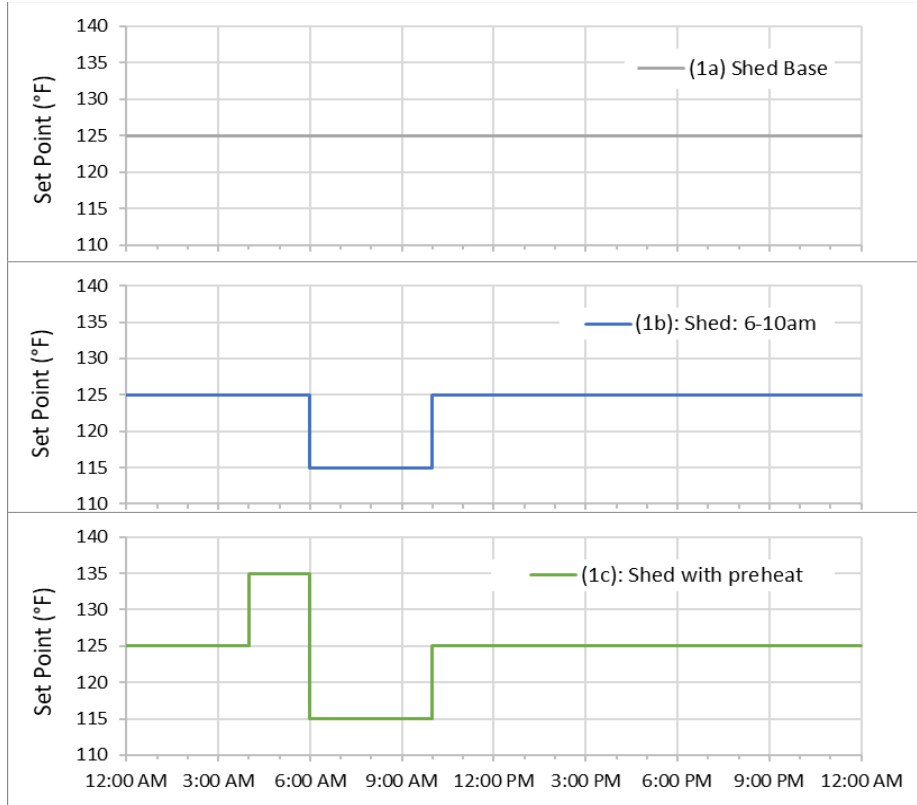


Figure 11. Setpoint schedules for the morning load shed cases

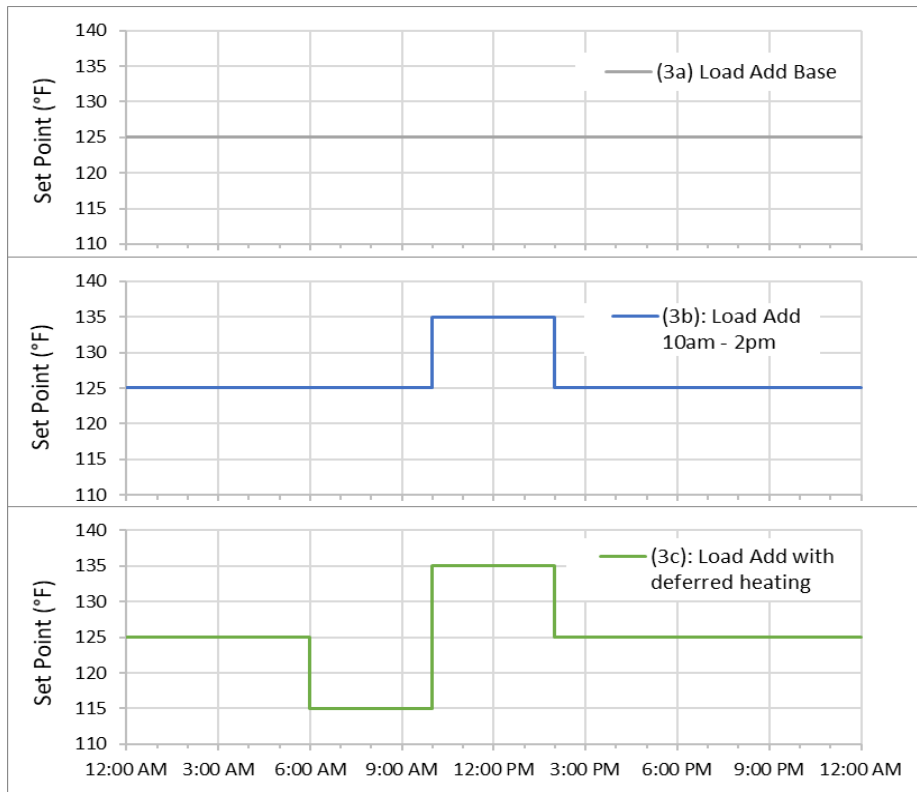


Figure 12. Setpoint schedules for the midday load add cases

A summary of the results from those tests is given below, along with graphs in Figures 13–16 that show power consumption and tank temperature during each test.

Table 1. Summary Results from Grid Service Tests in Hybrid and Electric Resistance Modes

Mode	Schedule	Total Energy (kWh)	Energy during DR period (kWh)	Min outlet water temp (°C)
Hybrid	1a (no schedule)	5.96	1.12	47
	1b - Load Shed	7.48	0	36.2
	1c - Load Shed w/ preheat	8.05	0	48.4
Hybrid	3a (no schedule)	5.96	1.27	47
	3b - Load Add	6.32	1.59	44.3
	3c - Load Add w/ deferred heat	11.82	7.11	36
Electric	1a (no schedule)	15.07	4.71	44.2
	1c - Load Shed w/ preheat	15.07	0	45.7
Electric	3a (no schedule)	15.07	5.15	44.2
	3c - Load Add w/ deferred heat	13.79	5.11	46.7

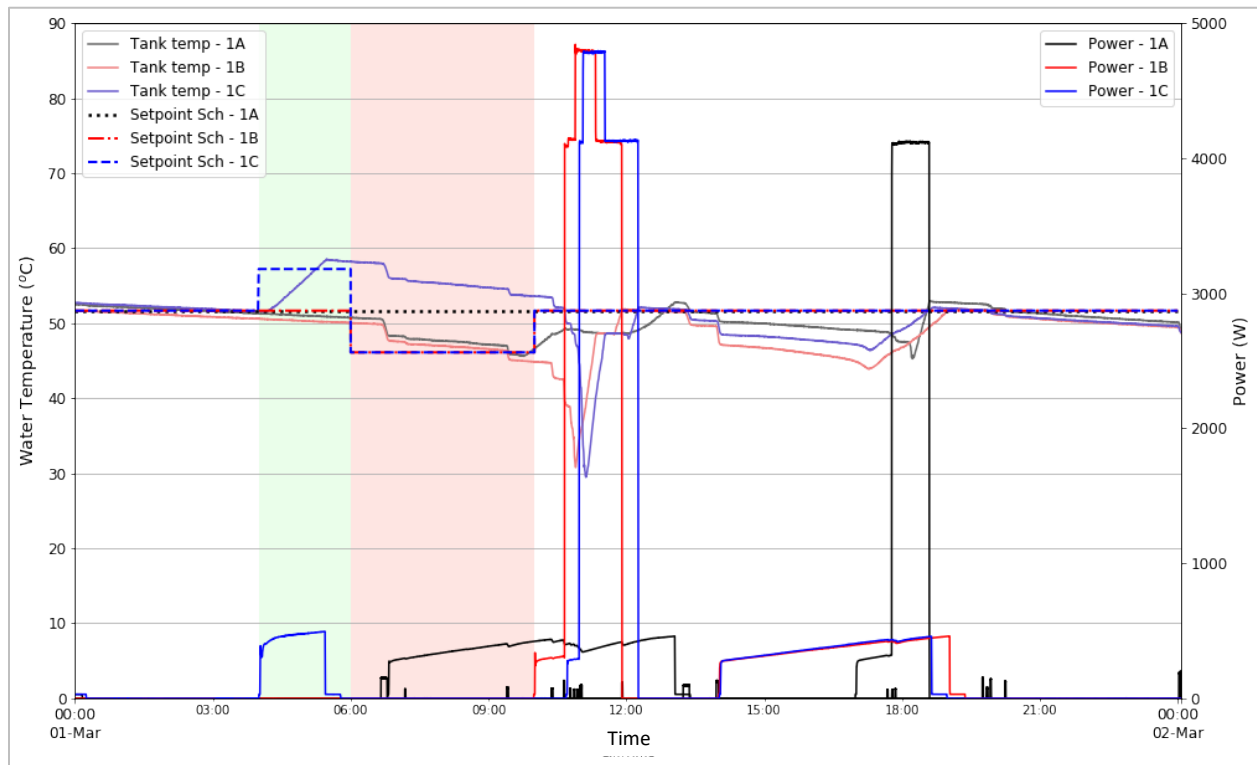


Figure 13. Hybrid Mode: Load Shed Schedules 1A, 1B and 1C. The green shaded band from 4–6 a.m. indicates the preheat period and red shaded band from 6–10 a.m. indicates the load shed period.

In the hybrid load shed cases, both the simple load shed schedule and load shed with preheating result in a complete elimination of energy use during the load shed period, at the cost of an increase in overall daily energy. The simple load shed case resulted in a 25% increase in daily energy use and the outlet water temperature dropped to 36°C (97°F), which is considered uncomfortable. The minimum delivered water temperature to satisfy comfort for mixed use events (handwashing and bathing) is 43.3°C (110°F). The load shed with preheat case resulted in a larger increase in daily energy use, 35% above the base case, but the outlet water temperature was maintained at a comfortable temperature throughout the test.

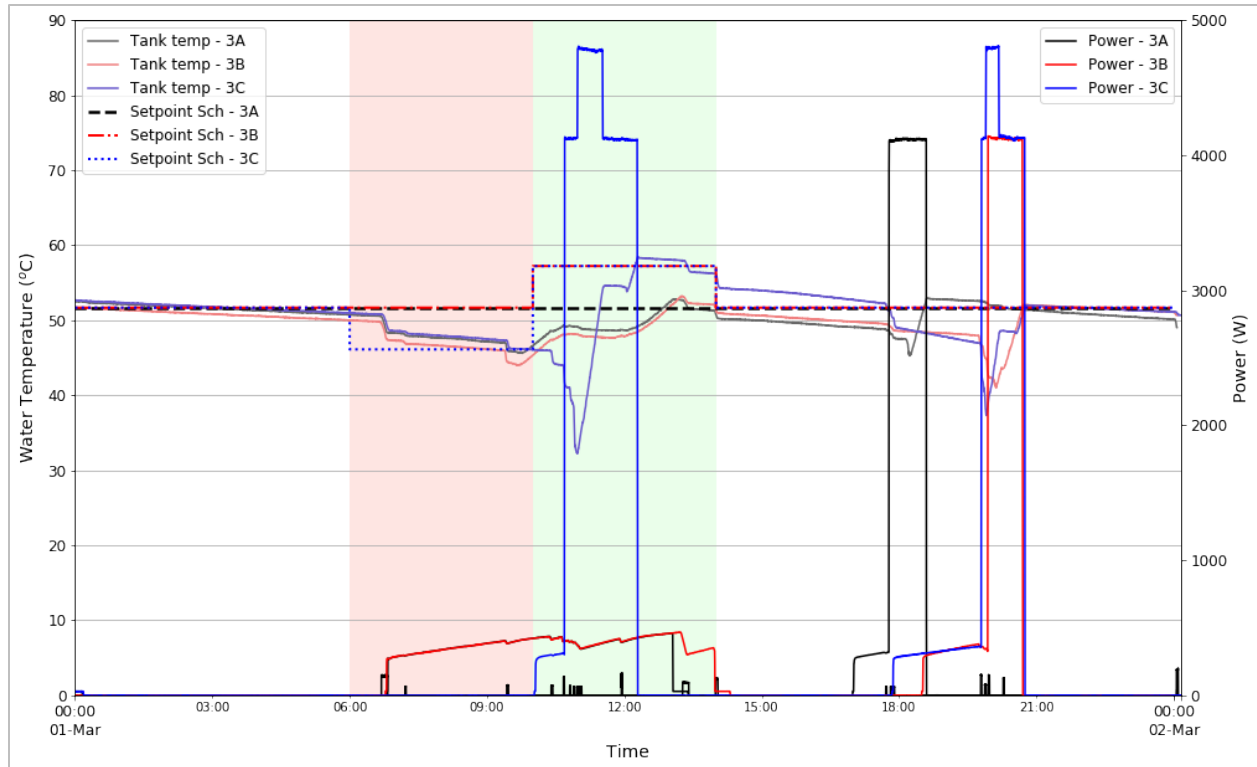


Figure 14. Hybrid Mode: Load Add Schedules 3A, 3B and 3C. The red shaded band from 6–10 a.m. is the deferred heating period and green shaded band from 10 a.m.–2 p.m. is the load add period.

The hybrid load add cases, both the simple load add schedule and load add with deferred heating, resulted in higher energy use during the load add period and higher daily energy use, but to different degrees. The simple load add case resulted in a 6% increase in daily energy and a 25% increase during the load add period. The outlet water temperature did not go below the minimum comfortable temperature, but came close. Load add with deferred heating led to doubling of the daily energy use and a 500% increase in energy use during load add period. However, the minimum outlet temperature dropped below 43°C, despite the increase in energy use because of the timing of the recovery.

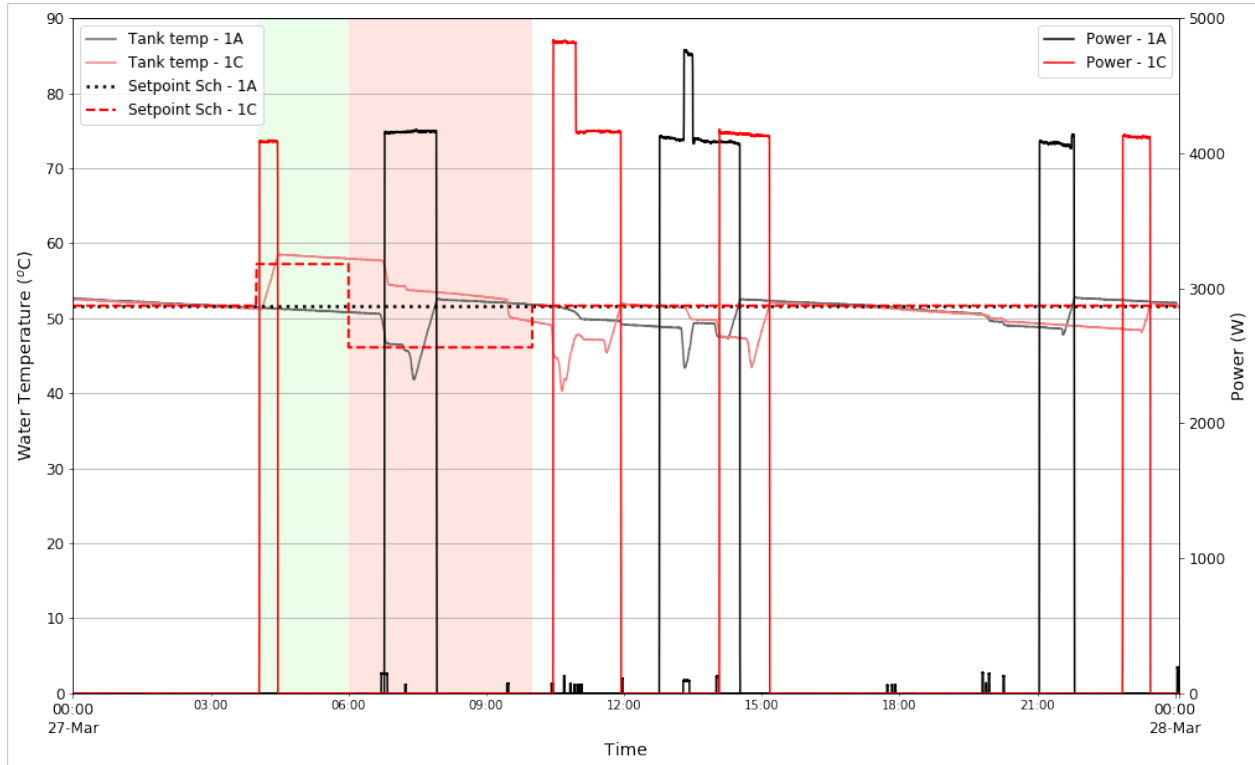


Figure 15. Electric Mode: Load Shed Schedules 1A and 1C. The green shaded band from 4–6 a.m. indicates the preheat period and red shaded band from 6–10 a.m. indicates the load shed period.

The electric mode load shed case was successful in that the daily energy use was unchanged when the load shed schedule was applied, all the energy use during the load shed period was eliminated and the outlet water temperature was always well above the minimum temperature for comfort.

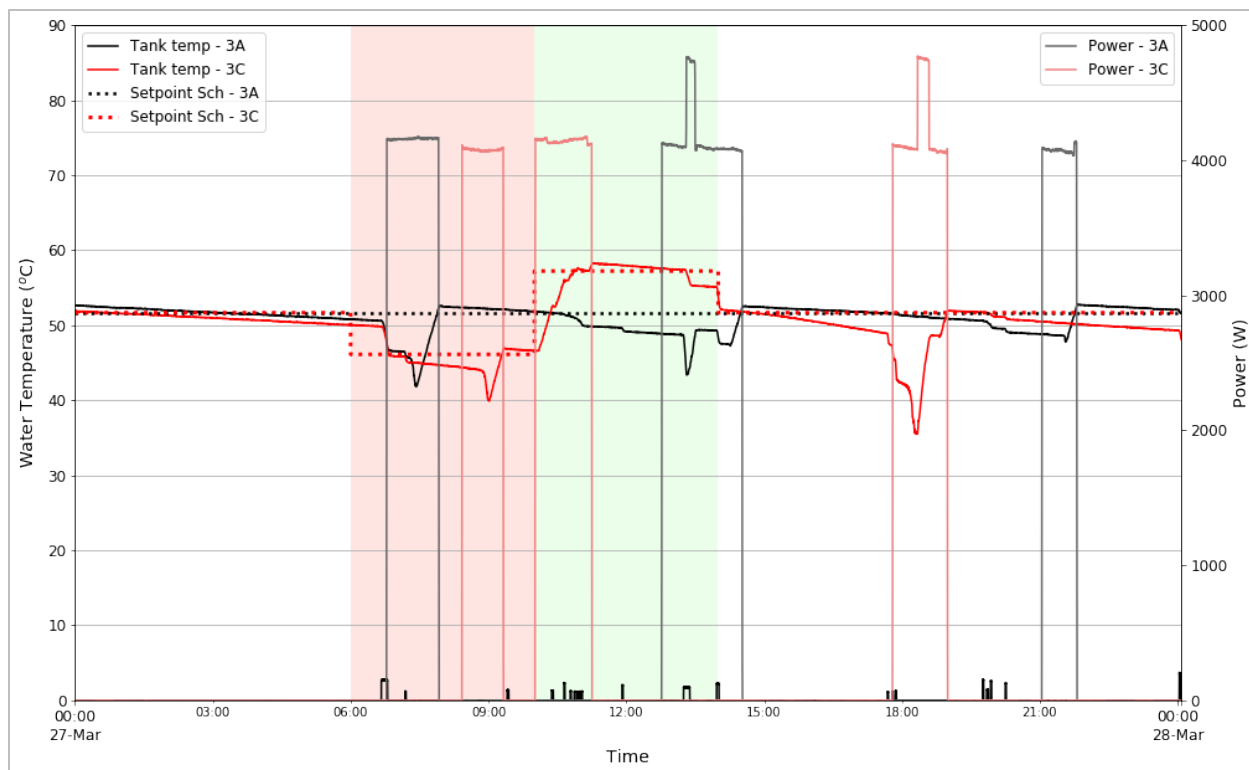


Figure 16. Electric Mode: Load Add Schedules 3A and 3C. The red shaded band from 6–10 a.m. is the deferred heating period and green shaded band from 10 a.m.–2 p.m. is the load add period.

The electric load add case was largely unsuccessful because the setpoint schedule resulted in a slight reduction (8%) in daily energy use and no change in energy use during load add period. The setpoint schedule shifted some energy use around but did not increase the energy use during the load add period, which is a reasonable outcome when setpoints are used for control in place of direct control of the heating elements. However, the load add case did shift the load to the start of the event, indicating that setpoint control can add load at specific times. The impact of load add control may be more substantial for shorter load add periods.

2.4.2 Custom Controls for Improved Grid Services

The results from the grid services tests that were implemented using only setpoint schedules indicated that some controls changes could improve the performance—both from the consumer’s perspective and the utility’s perspective. A few cases in hybrid mode saw the outlet temperature dip below what is considered the minimum comfortable outlet temperature for a water heater (43.3°C). We also saw instances where an electric element came on during a load shed as a result of the tank temperature dropping too rapidly. The following changes were being made to the basic GE controls to improve the performance during and after demand response events. We also tested the ability to duty cycle the heat pump or elements with different time periods to determine the minimum reasonable duty cycle.

1. Lower Element Deadband: Add deadband for lower element in hybrid mode that will turn on lower element if tank temperature is significantly below setpoint, even if draw is not actively occurring. This will help speed up recovery, especially following a load shed event. The lower element deadband was set to 10°C for all setpoints.

2. Reduced Heat Pump Deadband for Shed Event: Reduce deadband for heat pump during shed event. The deadband for the heat pump was set to 1°C for all setpoints, but only while in “load shed” event. (Under normal operation, the deadband varied with setpoint but was above 3°C for setpoints above 48.9°C/120°F.) This will ensure that the heat pump comes on more quickly to prevent the tank from getting too cold, which may lead to the use of electric elements. This may result in slightly more energy use during load shed events but should reduce overall energy use on days when load shed events occur.
3. Superboost: Create “superboost” mode for load add events during hybrid mode that combines the use of the heat pump and lower element, reduces the deadband to 1°C, and increases the setpoint to 71°C (160°F). If the tank temperature drops below the deadband temperature, the heat pump and lower element will turn on together. This mode only applies to hybrid mode during load add events.
4. Duty Cycle: Duty cycle control in both hybrid and electric modes. The duty cycle is defined by % on-time and duration of each on period. Hybrid mode duty cycle only applies to the heat pump and keeps fan on the entire time. (Under normal operation, the fan comes on before the compressor and stays on after the compressor turns off, so the fan was kept on during duty cycling tests.) Electric-mode duty cycle only applies to the lower element.

These modes were each tested to confirm that the changes had the desired impact and could be replicated in simulation. The day-long load add and load shed tests were not repeated. A summary of the tests performed, and the impact of the custom controls are given in the follow subsections, along with a graph showing the results for each change.

2.4.2.1 Lower Element Deadband

In hybrid mode, the heat pump was used to heat tank to 45°C. Once heating cycle was finished, the setpoint was changed to 55°C. This process was followed with original controls and with the modified controls. Each test was stopped once heating was complete.

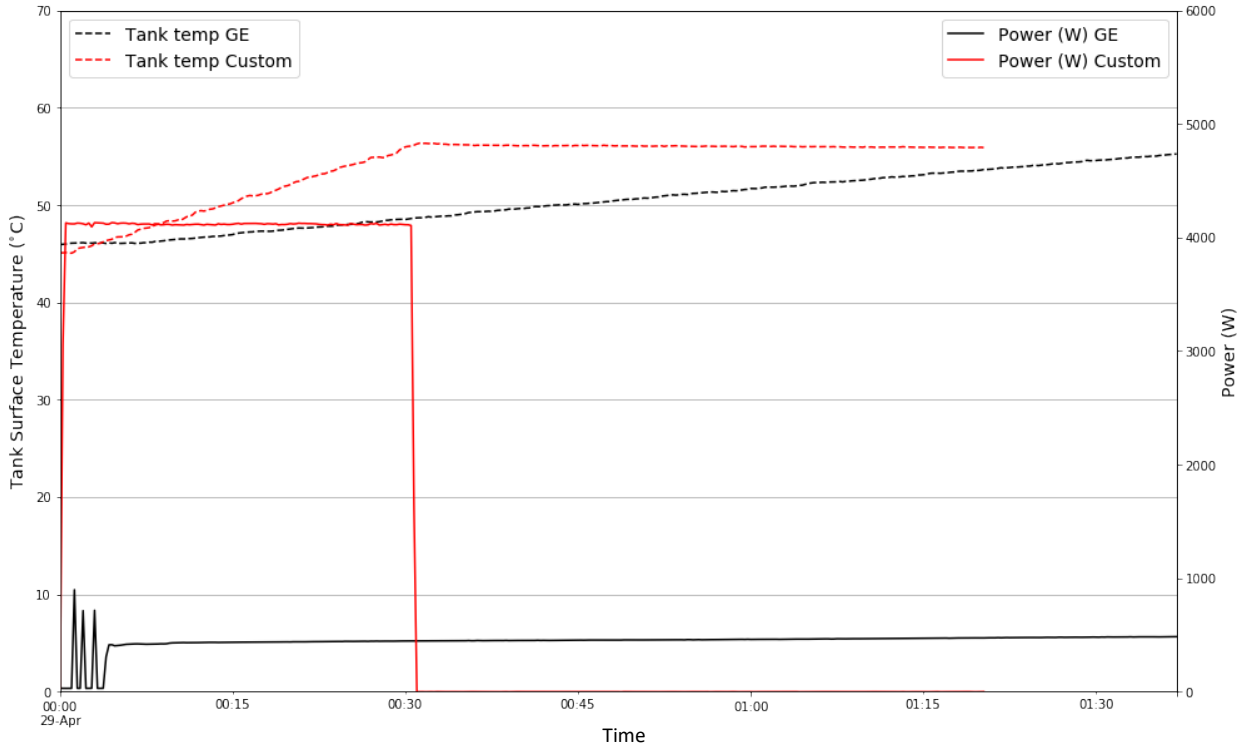


Figure 17. Impact of adding a lower element deadband

Table 2. Impact of Adding a Lower Element Deadband

Mode	Control	Test	Total Energy (kWh)	Recovery time
Hybrid	Element Deadband	GE Controls	0.72	90+min
Hybrid	Element Deadband	New Controls	2.09	30 min

The new deadband for the lower element (10°C) in hybrid mode was added so that the element comes on if there is a large increase in setpoint (such as, after a load shed event). The change to the deadband caused the element to come on, which increased energy use, but also reduced recovery time.

2.4.2.2 Reduced Heat Pump Deadband for Shed Event

In hybrid mode, the tank was heated with the heat pump to 51°C. Once the heating was complete, start “shed event” and a high-volume draw profile. Shed event will consist of 4.5°C drop in setpoint with the reduced heat pump deadband to 1°C. After two hours, the event ended and setpoint was returned to 51°C. A heating cycle should begin once event ends, if it was not already heating. This process was followed with original controls and with modified controls, with the test stopping once the heating was complete.

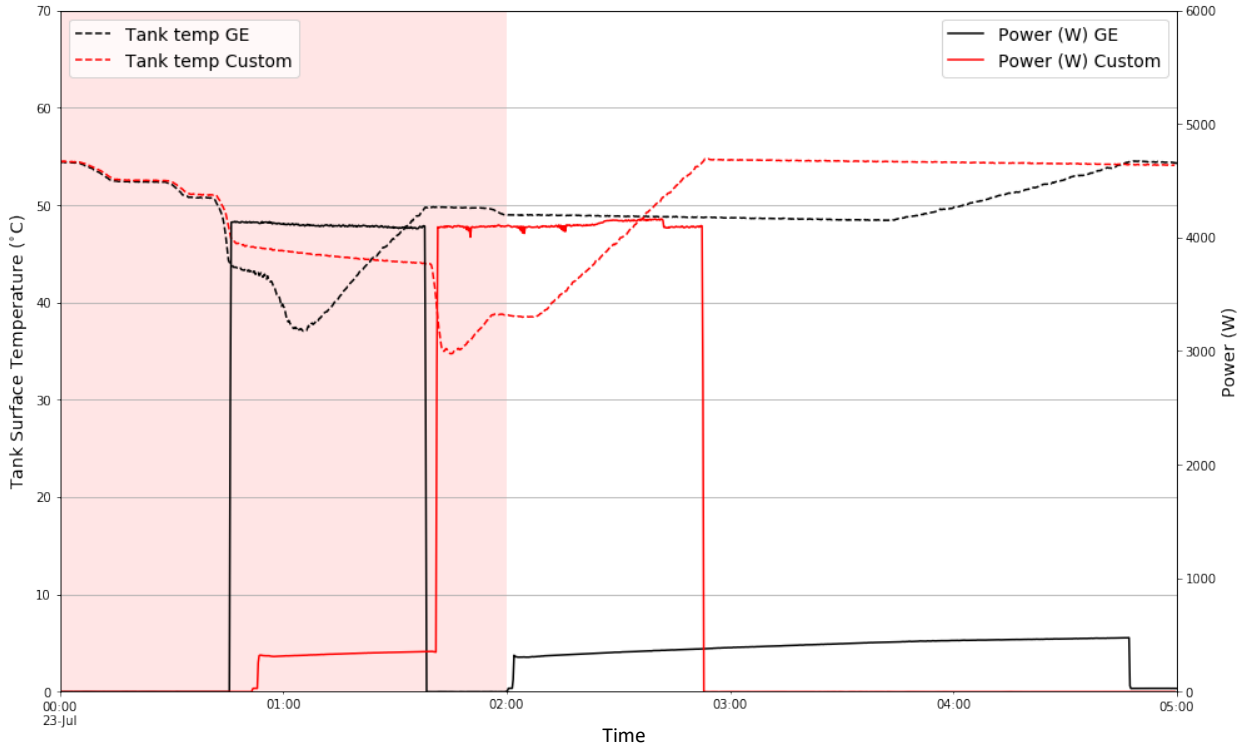


Figure 18. Impact of reduced heat pump deadband during shed event. The shed event is denoted by the red shaded period at the start of the test.

Table 3. Impact of Reduced Heat Pump Deadband During Shed Event

Mode	Control	Test	Total Energy (kWh)	DR period (kWh)	Recovery time
Hybrid	Load Shed Event	GE Controls	4.73	3.6	167 min
Hybrid	Load Shed Event	New Controls	5.16	1.54	53 min

A high-volume draw profile over the 2-hour shed event was implemented. In the GE control case, the draw caused the lower element to come on during the shed event. After the shed event ended, the heat pump came on, which took nearly 3 hours to fully recovery. In the custom control case, the heat pump came on during the shed event, followed by the electric element, which helped the water heater to recover more quickly. Overall, the custom control case used ~10% more energy over the entire test but reduced the energy use during the shed event by more than 50%. The recovery time was also much faster—53 minutes vs. 167 minutes (nearly 3 hours).

2.4.2.3 Superboost

In hybrid mode, heat the tank with the heat pump to 51°C. Once heating is complete, the “superboost load add” event was started. Superboost mode consists of reducing deadband to initiate heating (1°C), turning on the heat pump and lower element together, and changing the

setpoint to 71°C (160°F). The standard load add event consists of increasing the setpoint by 5°C with no change to deadband or heating element controls. The same process was executed with the original controls and with modified controls and the test finished once heating was complete.

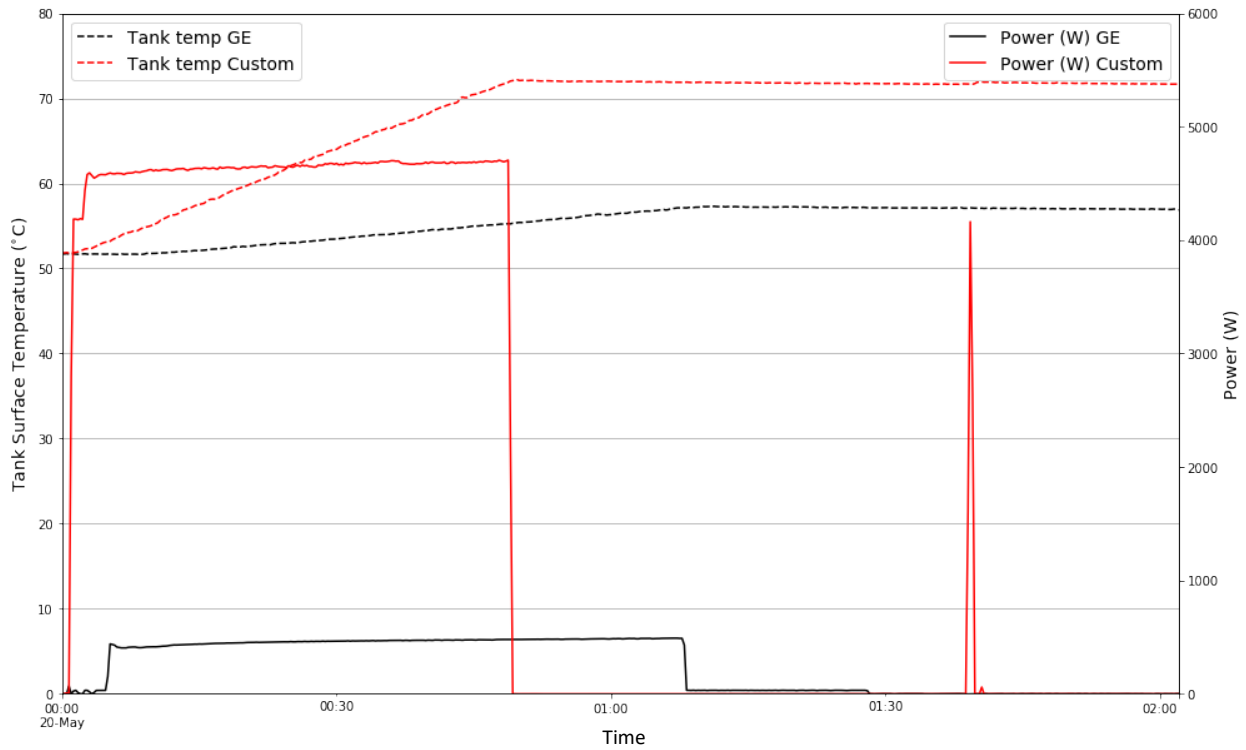


Figure 19. Impact of superboost mode during load add event

Table 4. Impact of Superboost Mode During Load Add Event

Mode	Control	Test	Total Energy (kWh)
Hybrid	Load Add	GE Controls	0.5
Hybrid	Superboost Load Add	New Controls	3.74

Superboost mode forced the heat pump and lower element to operate together, raised the tank setpoint, and reduced the deadband for the combined heating elements to 1°C, which resulted in a significant increase in energy use relative to the GE controls, where a modest setpoint increase was the only control imposed.

2.4.2.4 Duty Cycle Tests

The duty cycle tests were only executed with the heat pump. The test started with the tank at 45°C. Each test, as described in Table 5, was run for an hour with a short pause before moving on to the next duty cycle test.

Table 5. Summary of Duty Cycle Tests

Test #	% On	Time On (min)	Test Duration
1	50	5	1 hour
2	50	7.5	1 hour
3	50	10	1 hour

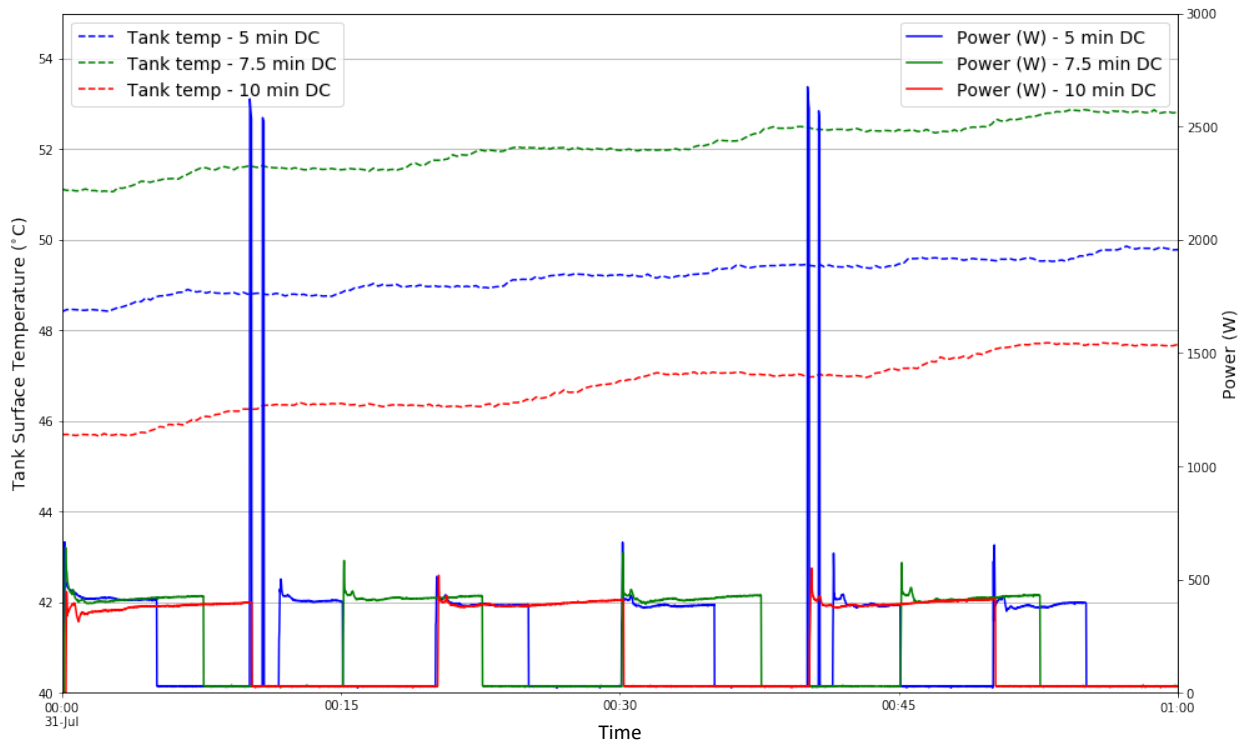


Figure 20. Impact on tank temperature from the duty cycle tests

Table 6. Impact from Duty Cycle Tests

Mode	Control	Test	Total Energy (kWh)	ΔT (°C)
Heat Pump	Duty Cycle	50%, 5 min on	0.21	1.44
Heat Pump	Duty Cycle	50%, 7.5 min on	0.22	1.81
Heat Pump	Duty Cycle	50%, 10 min on	0.21	2.07

Shorter duty cycle tests (1 minute and 2.5 minutes on) were attempted but did not produce stable heating, so were not included in the results. Each test shown above involved a 50% duty cycle, so the total energy use was the same across the three tests. Extending the on-time to 10 minutes resulted in the largest increase in temperature over the hour, and longer cycles would likely lead to larger temperature increases. There is very little heat added to the tank during the first couple

minutes that the heat pump is on, so reducing the number of times that the heat pump turns on improves the heating efficiency.

2.5 Model Validation

The model described in Section 2.2 was validated against several of the lab tests to ensure that the model provided reasonable agreement. The validation focused on the water heater operating in hybrid mode, which is substantially more complex because of the control decisions required. For the validation, the boundary conditions (incoming water temperature, ambient air temperature/humidity, and flow rate) were taken directly from the lab data. Simulation results were then compared to ensure that the tank temperature and power consumption matched. Because the controls implemented on the control board could not be used directly in simulation, mostly because of the two-node tank model (refer to Section 2.2), the control logic was derived by comparing against several of the tests and iterating on simulated control decisions.

In the lab testing, there were 11 thermocouples distributed within the tank to fully capture the stratification. However, the model only has two nodes, each with a temperature representing the average of the entire volume represented by the node. For comparison purposes, only the average tank temperature is shown. Because of the complicated mixing and conduction that occurs within an actual tank, it is expected that there may be some discrepancy between the measured and modeled tank temperatures shown as part of the validation. There were similar problems when trying to recreate the GE controls using a temperature sensor co-located with the sensor used for the default controls—slight variations in initial conditions and draw volumes had a big impact on when heating elements turned on (or did not), which led to differences in tank temperatures and energy consumption.

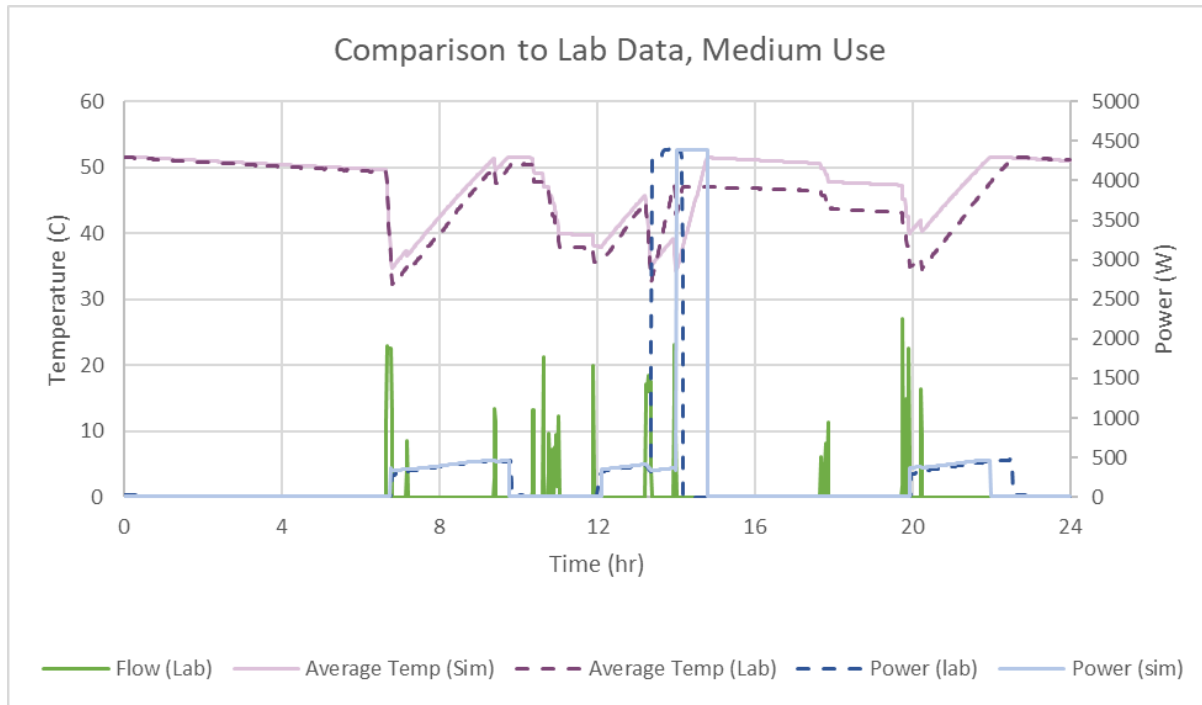


Figure 21. Model validation results for the medium use case with default controls

Figure 21 shows the results of the validation when comparing to a medium hot water use case. The model does a reasonable job of matching the tank temperatures within the expected variation due to using a point temperature as representing the average of a larger volume within the tank. Most importantly, the upper node temperature closely matches, which ensures that the delivered energy of the simulation matches the laboratory results. Although the lower temperature does sometimes deviate, it shows a similar response to draw events. Overall, the simulated power consumption of the water heater matches within 1% (6.26 kWh measured vs. 6.21 simulated), although there are some differences in the timing of events. The vast majority of control decisions within the tank are triggered by hot water draws. The backup electric resistance element is triggered one draw later in simulation than was seen in the lab, causing a shift of about 30 minutes in the element usage. This 30-minute delay in the element usage also means that the tank goes into the third heating event (starting around hour 20 of the test) at a higher average temperature in simulation, which requires less heat to recover from this event. Despite these timing differences, the models match reasonably well given the reduced order of the model.

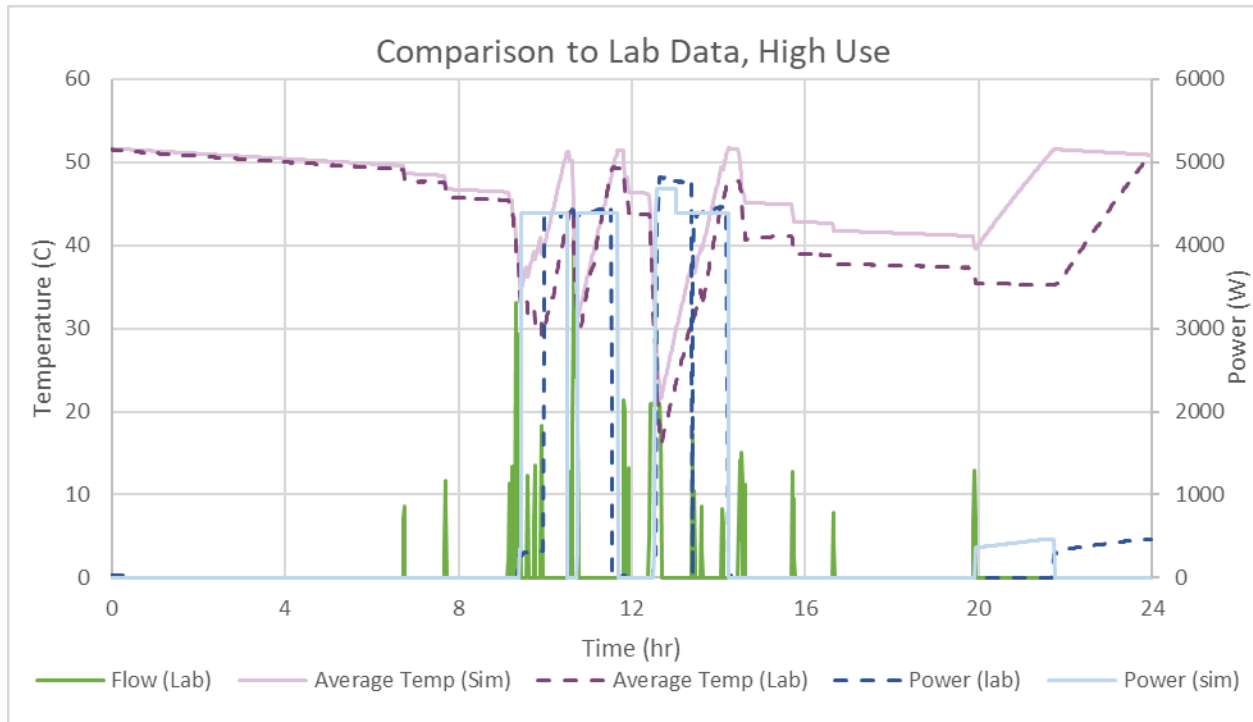


Figure 22. Model validation results for the high use case with default controls

Figure 22 shows the results of the validation when comparing to a high hot water use case. The high use case is more complicated than the medium use case, so temperatures are omitted for clarity. In the high use case, the model triggers the electric element sooner than in the laboratory data. This is likely because of the inherent lag associated with mixing the tank, even during large draws, associated with physical equipment that is difficult to capture in a model. The upper element also does not stay on as long during the second heating event, although it is still triggered and does transition back to the lower element. The final heating event is also triggered by a draw rather than standby, although the duration is comparable. Overall, for the high use case the power consumption varies by 11% (15.4 kWh measured vs. 17.2 kWh simulated), with the timing of heating events also lining up reasonably well with laboratory data.

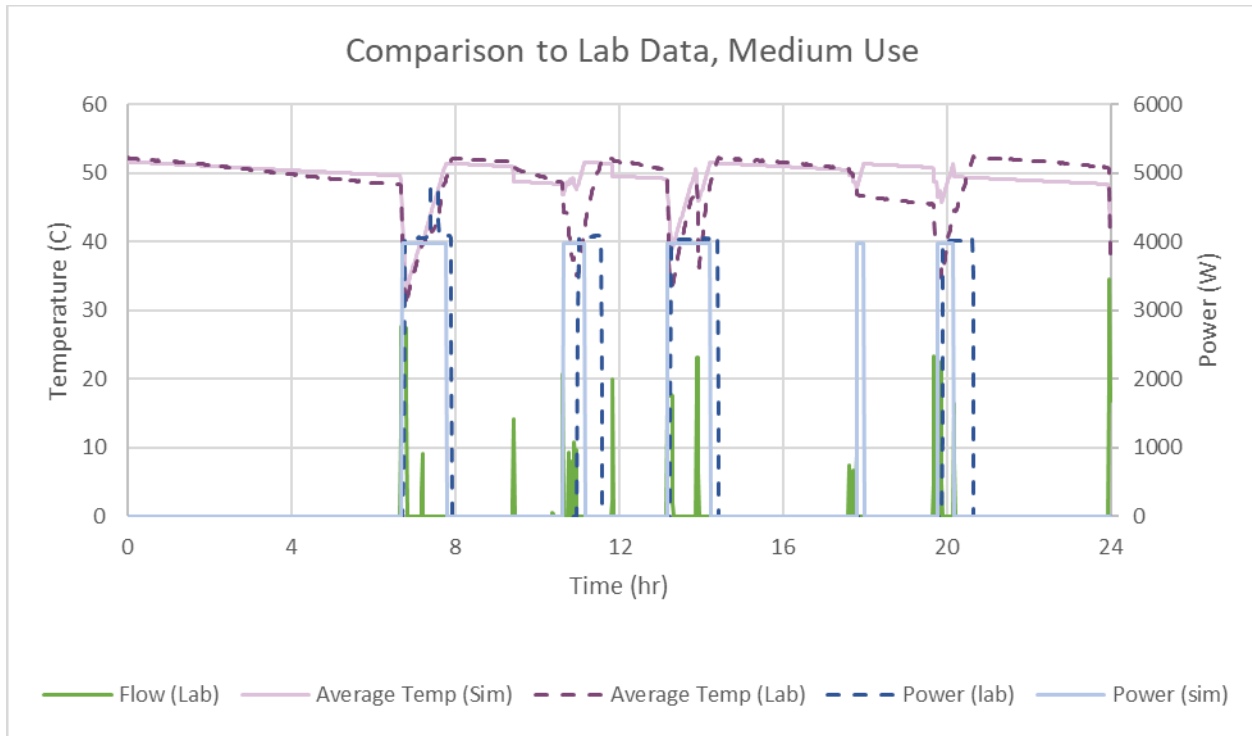


Figure 23. Model validation results for the medium use case with default controls, electric mode

Figure 23 shows the results of the validation when comparing to a medium hot water use case when the HPWH is operating in electric mode. In this case, the timing of element events also roughly agrees, although the model is slightly more sensitive to draws than the actual lab results. This is likely because of the simulation including a lower temperature sensor rather than controlling purely based on the rate of change of temperature for the upper node. This extra sensitivity leads to the element turning on slightly earlier and in one case, near hour 18, turning on in simulation when the water heater did not respond in the lab. However, the overall results are within 13% (15.0 kWh measured vs. 12.9 kWh simulated).

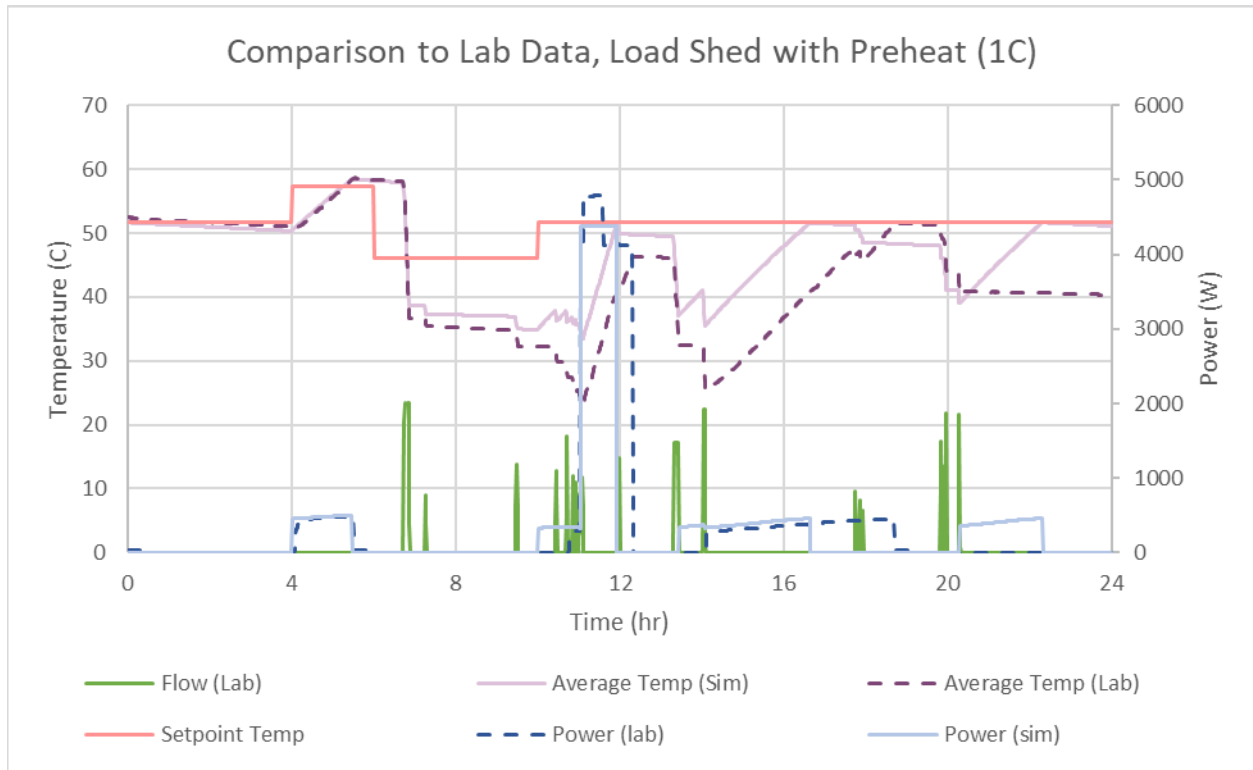


Figure 24. Model validation results for load shed with preheating

Figure 24 shows the results of the validation for the case of load shed with preheating. In this case, the model accurately captures the preheating of the tank starting 2 hours before the shed event. After the shed event ends and the setpoint is raised, the simulated HPWH immediately turns on because of the low tank temperatures, while the actual unit does not turn on until several large draws occur 30 minutes later. This additional heating of the tank in simulation leads to the upper element not coming on during the first element heating event and the event ending earlier in simulation. This earlier end time then further propagates to affect the timing of later events. Despite these timing differences, the model captures the mix of element and heat pump heating, leading to a 12% difference in daily energy (8.05 kWh measured vs. 7.05 kWh simulated).

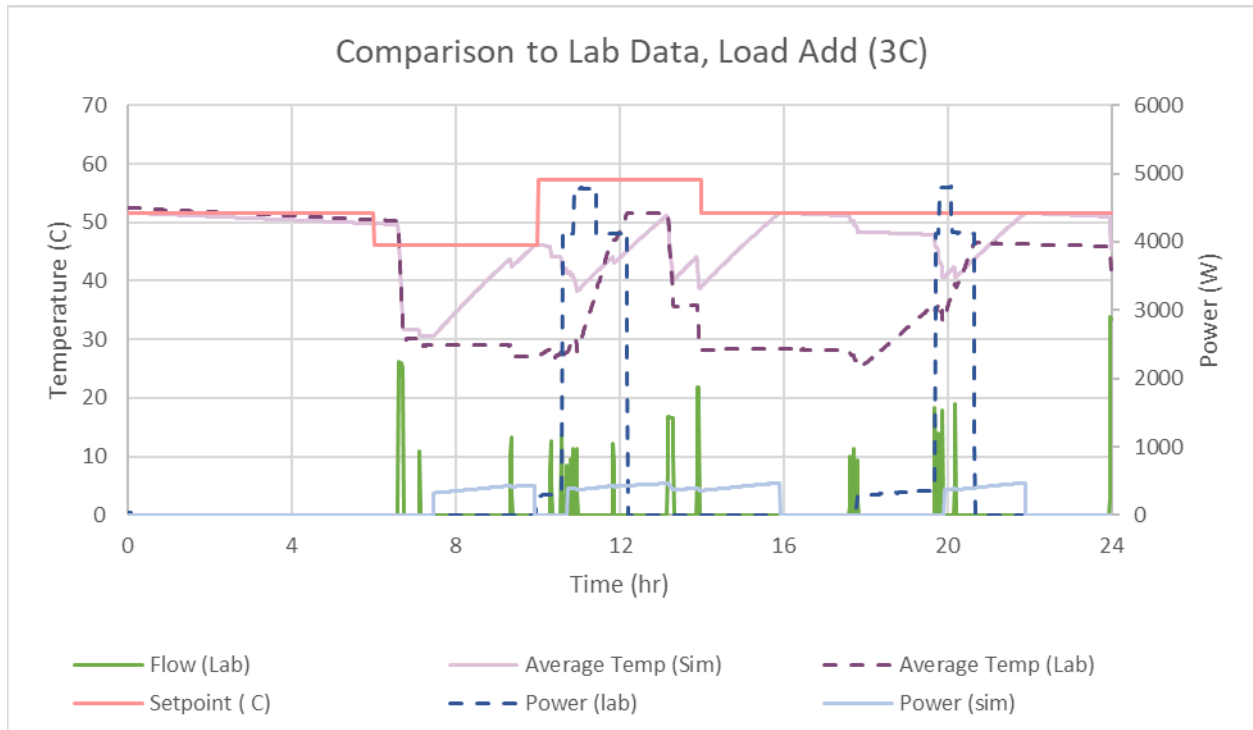


Figure 25. Model validation results for load add with deferred heating

Figure 25 shows the results of the validation for the load add case with deferred heating. This case has the largest discrepancy in daily energy use (67%: 3.96 kWh simulated, and 11.82 kWh measured) of any of the validation efforts, with the model showing distinctly different performance from the lab data. In the measured data, the HPWH was successfully able to fully shift the load out of deferred heating and into the load add period. However, draws during the latter half of the load add period occur at an average temperature below the minimum temperature and are likely to be uncomfortable for the user. The model responds much earlier, during the deferred heating period, but is able to provide water at a comfortable temperature during the shed period. This substantial difference propagates through the results, with the model able to deliver hot water during the load add period using only the heat pump, because the tank is substantially warmer at the end of the deferred heating period. The model does not fully capture the control seen in the lab, but the actual water heater uses controls that do not always sufficient provide hot water. This result is indicative of the challenge of trying to capture controls decisions controlled by complex logic and a single point measurement in a simplified model.

In addition to validating the model under standard operating conditions, validation was done to ensure the model could capture the new controls added as part of this project. Figure 26 shows the simulation results from superboost mode compared to the lab data. There were no hot water draws during this test and the simulation model matches the lab results well. Because the simulation model does not fully capture transients, it gets to the full load power faster, which leads to the tank heating up slightly faster in simulation and the heat sources (lower element and heat pump) turning off sooner. Overall, the model and lab data are in excellent agreement with a 2% difference in energy consumption (3.71 kWh measured vs. 3.64 kWh simulated).

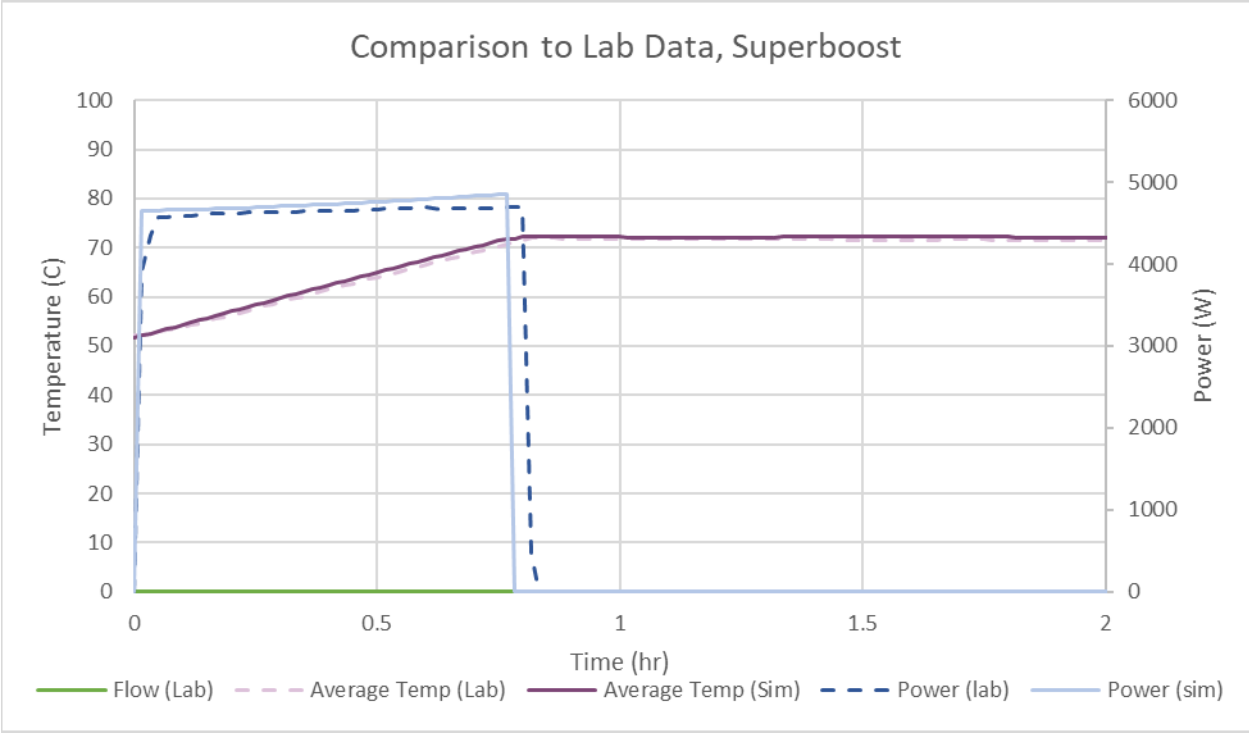


Figure 26. Model validation results for “superboost” mode

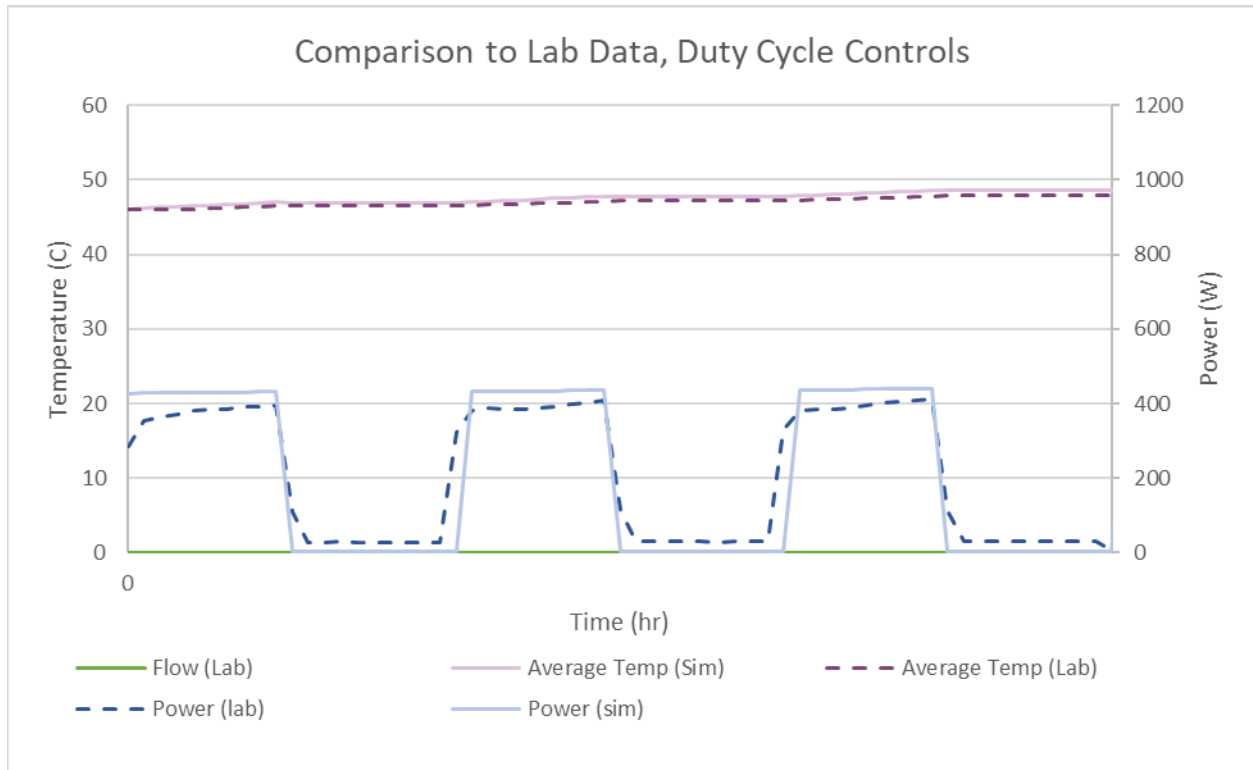


Figure 27. Model validation results for duty cycling

Figure 27 shows the simulation results from duty cycling (50% duty cycle, with a 10 minute on-time) compared to the lab data. This test was also performed without any hot water draws. In this case, the transient aspects of the heat pump performance (namely that it takes a while after turning on to reach steady state) is a bit more pronounced because of the cycling. There is overall a 3% difference in energy consumption (0.21 kWh measured vs. 0.20 kWh simulated) despite the transient performance not fully being captured.

2.6 Conclusions

This report describes detailed laboratory testing of a HPWH focused on the potential to respond to grid events. In addition to characterizing the performance of the HPWH using its existing controls, new controls were implemented and tested in the lab. Based on the laboratory testing, HPWHs are currently capable of responding to grid events and providing services, but they can provide a greater level of service if more flexibility is allowed in the controls. Additional services could be provided by allowing the heat pump to duty cycle (minimum on-time of 5 minutes, but 10 minutes or more of on-time are preferred) or by increasing the maximum allowed thermostat. However, allowing this additional grid response capability may have impacts on the lifetime and hot water provided. Integrating a tempering valve into the HPWH would allow the tank to heat above the existing safety thresholds without impacting users, but duty cycling may reduce the heat pump lifetime and increasing the setpoint temperature may increase the rate of galvanic corrosion, reducing the tank's lifetime. The work performed here could be discussed with a manufacturer to weigh the potential trade-offs associated with these changes.

A model of the HPWH was also created based on the laboratory data. This model is simplified to two nodes while still matching the majority of the laboratory data within 15% of daily energy. This model represents a substantial reduction in complexity when compared to existing models, which usually require a fully stratified tank. This model was able to capture standard performance (both in hybrid and electric-only mode) as well as the advanced grid services tested here.

2.7 References

- Burch, J. and Christensen, C. 2007. *Towards development of an algorithm for mains water temperature*. Cleveland, OH.
- Hendron, B., Burch, J., and Barker, G. 2010. "Tool for Generating Realistic Residential Hot Water Event Schedules." Conference Paper NREL/CP-550-47685. August 2010.
- Lutz, J., and Moya, M. 2012. *Typical hot water draw patterns based on field data*. Berkeley, CA,. Web. doi:10.2172/1127143.
- Maguire, J., Burch, J., Merrigan, T. and Ong, S. 2013. *Energy Savings and Breakeven Cost for Residential Heat Pump Water Heaters in the United States*. Golden, CO. NREL/TP-5500-58594.
- Pratt, R. et. al. 2019. *Battery Equivalent Models for Distribution Energy Resource Devices Ability to Provide Grid Services*. Richland, WA.
- Wilson, E., Metzger, C., Horowitz, S. and Hendron, R. 2014. *2014 Building America House Simulation Protocol*. Golden, CO. NREL/TP-5500-60988.

Part 3

3.0 Commercial Refrigeration Systems

Oak Ridge National Laboratory

Jeffrey Munk

Teja Kuruganti

Jian Sun

Borui Cui

Jin Dong

Table of Contents

3.1	Introduction and Objectives.....	3.9
3.2	Commercial Refrigeration System and Display Case Model	3.10
3.2.1	Background and Main Assumptions.....	3.10
3.2.2	Modeling of Physics of Commercial Refrigeration Systems and Display Cases	3.11
3.3	Test Hardware.....	3.20
3.3.1	Commercial Refrigeration Systems and Display Cases Tested.....	3.20
3.3.2	Testing Hardware and Data Acquisition Setup.....	3.24
3.4	Test Procedures.....	3.26
3.4.1	Relevant Standards and Test Methods.....	3.26
3.4.2	Characterization Test.....	3.30
3.4.3	Baseline Test.....	3.30
3.4.4	Response Characterization to Control Inputs Test	3.31
3.4.5	Manufacturer Tests	3.32
3.5	Experimental Results and Model Validation.....	3.32
3.5.1	Experimental Results.....	3.32
3.5.2	Power Consumption Calibration and Validation.....	3.36
3.5.3	Display Case Temperature Calibration and Validation.....	3.45
3.5.4	System Validation.....	3.50
3.6	Battery-Equivalent Model	3.52
3.7	Conclusions	3.54
3.8	References	3.56

Figures: Part 3

Figure 1. System diagram of commercial refrigeration system	3.10
Figure 2. Generic virtual battery system broken down into components of thermal mass, equipment, and controls.....	3.12
Figure 3. Schematic of simplified CO ₂ supermarket refrigerator display case models.	3.13
Figure 4. Commercial refrigeration system pressure-enthalpy (P-h) diagram.....	3.15
Figure 5. Relationship between ambient temperature and saturated discharge temperature	3.19
Figure 6. Commercial refrigeration system	3.21
Figure 7. Low temperature display case	3.22
Figure 8. Medium temperature display case	3.23
Figure 9. Sample data showing product temperatures of a medium temperature refrigeration case during and after a defrost cycle	3.26
Figure 10. Test simulator dimensions from ASHRAE 72-2005	3.28
Figure 11. Typical test simulator location and filler material in a refrigerated case with shelves from ASHRAE 72-2005	3.28
Figure 12. Example 24-hour test period from ASHRAE 72-2005.....	3.29
Figure 13. Medium temperature (MT) compressor power consumption at different MT suction pressure set points	3.34
Figure 14. Low temperature (LT) compressor power consumption at different low temperature suction pressure set points.....	3.34
Figure 15. Medium temperature (MT) compressor power consumption at different MT display case air temperature set points	3.35
Figure 16. Low temperature (LT) compressor power consumption at different LT display case air temperature set points	3.35
Figure 17. Medium temperature (MT) compressor power consumption at different false loads	3.36
Figure 18. Power consumption calibration for compressor 2KSL-1K.....	3.38
Figure 19. Power consumption calibration for compressor 2MSL-07K.....	3.38
Figure 20. Power consumption calibration and validation data for compressor 4MTC-7K	3.38
Figure 21. Power consumption calibration and validation data for compressor 4MTC-10K	3.39
Figure 22. Low temperature compressor power consumption comparison of simulation and test data from validation test case 1	3.40
Figure 23. Medium temperature compressor power consumption comparison of simulation and test data from validation test case 1	3.40
Figure 24. Low temperature compressor power consumption comparison of simulation and test data from validation test case 1	3.41
Figure 25. Medium temperature compressor power consumption comparison of simulation and test data from validation test case 1	3.41
Figure 26. Low temperature compressor power consumption comparison of simulation and test data from validation test case 2	3.43

Figure 27. Medium temperature compressor power consumption comparison of simulation and test data from validation test case 2	3.43
Figure 28. Low temperature compressor power consumption comparison of simulation and test data from validation test case 2	3.44
Figure 29. Medium temperature compressor power consumption comparison of simulation and test data from validation test case 2	3.44
Figure 30. Comparison of simulated and measured power consumption from validation test case 3	3.45
Figure 31: Open case refrigerator display case model training results from March 1 to March 2, 2019.	3.46
Figure 32. Open case refrigerator display case model validation results from March 3 to March 5, 2019.	3.47
Figure 33. Closed case refrigerator display case model training results from July 22 to July 26, 2019.	3.48
Figure 34. Closed case refrigerator display case model validation results from July 26 to August 1, 2019.	3.49
Figure 35. Closed low temperature (LT) display case air temperature: test vs. prediction.....	3.51
Figure 36. Low temperature (LT) compressor power consumption: test vs. prediction.....	3.51
Figure 37. Open medium temperature (MT) display case air temperature: test vs. prediction.....	3.51
Figure 38. Medium temperature (MT) compressor power consumption: test vs. prediction.....	3.52

Tables: Part 3

Table 1. Compressor Specifications for Laboratory Setup	3.22
Table 2. Specifications for Refrigerated Display Cases.....	3.23
Table 3. Measurement Points and Instrument Specifications	3.25
Table 4. Baseline Test Conditions	3.30
Table 5. Tests for Characterizing System Response to Control Inputs.....	3.31
Table 6. Examples of Manufacturer Performance Test Data.....	3.32
Table 7. Compressor Parameters	3.37
Table 8. Accuracy Indices of the Developed Open/Closed Case RC (Resistance-Capacity) Models	3.50
Table 9. Parameters for the Battery-Equivalent Model	3.53

Abbreviations, Acronyms, and Initialisms

AHRI	Air-Conditioning, Heating, & Refrigeration Institute
ANSI	American National Standards Institute
ASHRAE	American Society of Heating, Refrigerating and Air Conditioning Engineers
CDEC	calculated daily energy consumption
DER	distributed energy resource
DOE	U.S. Department of Energy
EPCA	Energy Policy and Conservation Act
LT	low temperature
MT	medium temperature
PI	proportional integral
PLR	partial load ratio
PSO	particle swarm optimization
PV	photovoltaics
RMSE	root mean square error
SDT	saturation discharge temperature
SMT	saturation middle stage temperature
SOC	state of charge
SST	saturation suction temperature
TDEC	total daily energy consumption

Acknowledgments

Funding for this research was provided by the US Department of Energy, Office of Energy Efficiency and Renewable Energy, Vehicle Technologies Program. The authors would like to thank Lee Slezak, Vehicle Systems and Testing Manager in the Vehicle Technologies Program, for his support of this project.

Executive Summary

The growing demands on the grid in terms of greater resilience and reliability, led by the increased use of distributed and clean energy resources, have led to growing interest in using building equipment as a resource. Building equipment can provide the greater operational flexibility required by the grid by offering a number of valuable services at the bulk system level and local distribution levels.

A challenge associated with the use of building equipment as a distributed energy resource is quantifying the magnitude of power available to dispatch or energy flexibility. One solution to this challenge is to develop standard methods for modeling the ability of individual devices of various equipment classes to respond and provide these services. This study provides a general, standard device model with a battery equivalent interface applicable to one building equipment type: commercial refrigeration systems. This standard device model will be compared to an equivalent battery model to determine the capabilities of devices from different equipment classes and extrapolate their ability to deliver grid services. The main characteristics of the device model for commercial refrigeration systems include the following.

- The device model is simple and generic to use with only a single, simple dispatch algorithm for each grid service, rather than requiring modifications to a custom algorithm.
- The device model can be used with complementary tools used in the planning, design, or modernization of grid infrastructure, or it can be used with tools to operate transmission- and distribution-level grid management and control systems (including market modeling tools) so the roles and functions can be properly represented and evaluated.
- The device model is a unified model for evaluating the performance of grid services.

Along with this development, the commercial refrigeration system characterization protocols are developed and tested to measure the parameters defined by the model to provide evidence of the adequacy and accuracy of the system and battery equivalent interface.

Some useful insights on commercial refrigeration system models and tests are listed below.

- The load flexibility provided by the commercial refrigeration has been tested through several control strategies: modulating the display case ON/OFF, adjusting the display case air temperature set point, and changing the compressor suction pressure/head set point. Among these strategies, the modulation of display case ON/OFF provides the largest amount of load flexibility (but has clear service level impacts).
- Several other control strategies can provide commercial refrigeration system load flexibility, including controlling the variable frequency drive compressor speed and coordinating display case defrost schedules.
- The standard device models of display cases (closed and open display cases) integrated with the commercial refrigeration system reduced model can predict the load flexibility with acceptable accuracy.

3.1 Introduction and Objectives

This report is one of the deliverables for Grid Modernization Laboratory Consortium Project 1.4.2—Definitions, Standards and Test Procedures for Grid Services from Devices.

The focus of this report is to describe the modeling and testing of a commercial refrigeration system. Electric vehicle charging and residential water heaters are covered in separate volumes. The purpose of this testing is twofold: to validate the device models developed in the project's first two years, and as a pilot test of procedures that can be used to obtain the device parameters needed to populate such models. To understand the context for these plans, a short description of the project is presented here.

The overarching goal of the project is to enable a broad range of devices—principally distributed energy resources (DERs)—to provide the operational flexibility required by the grid through delivering valuable services at the bulk system level and local distribution levels. To do this, the project focuses on developing standard methods for modeling the ability of individual devices of various equipment classes to respond to requests for grid backup services. DER devices include responsive load-serving equipment and appliances in buildings, battery storage, electric vehicle chargers and their batteries, smart inverters for photovoltaics (PV) solar and batteries, and fuel cells and electrolyzers.

Existing grid services include ancillary services (regulation, reserves, ramping) that keep the grid in supply-demand balance, managing peak loads to reduce infrastructure capacity requirements while managing wholesale purchase and production costs. Industry has also envisioned new reliability services from DERs such as artificial inertia, participation in remedial action schemes that enhance the reliability and stability of the bulk grid, and new distribution-level services such as mitigating rapid voltage changes and reverse power flows from high solar PV penetrations.

As its primary technical goal, the project will provide a general, standard device model with a battery equivalent interface applicable to each device class. This will be in the form of an equivalent battery model, useful for comparing and aggregating the capabilities of devices from different equipment classes and extrapolating their ability to perform grid services. This model is designed to be modular and readily incorporated in grid planning and operational tools. It will be simple and generic to use, representing all device types together with only a single, simple dispatch algorithm for each grid service, rather than a custom algorithm for each equipment class. Such a model of DER devices is required for the tools used to plan and design new and modernized grid infrastructure and to operate transmission- and distribution-level grid management/control systems and markets, so they can properly represent the roles and functions of DERs in the future grid.

Developing a unified modeling approach for evaluating the performance of grid services from DER devices is the basis for achieving the project's outcomes:

- Enable utilities and grid operating entities to accurately assess the contribution of DER devices at planning and operational time scales by using models of their performance that can be incorporated into the tools used to plan and operate the grid.

- Encourage device manufacturers to add the capabilities needed to supply existing and new grid services by clearly articulating the performance characteristics required and a means for evaluating their engineering and economic potential in various regions of the nation.

3.2 Commercial Refrigeration System and Display Case Model

The device models will be developed to estimate the display case temperature and refrigeration system power consumption. A general, standard device model with a battery-equivalent interface will be developed to predict display case temperature, and the refrigeration system power consumption will be calculated through equipment models, which provides a way to convert the heat transfer to or from the thermal storage to electrical power consumption of the equipment.

3.2.1 Background and Main Assumptions

3.2.1.1 Background

As shown in Figure 1, the commercial refrigeration system is composed of a compressor rack, an air-cooled gas cooler/condenser, medium temperature (MT) and low temperature (LT) display cases, and MT and LT “false” loads. The compressor rack contains two LT compressors (one variable and one fixed speed) and three MT compressors (one variable speed and two fixed speed) to provide an LT cooling capacity of about 31,000 Btu/h and an MT cooling capacity of about 115,500 Btu/h. One four-door vertical display case and a false load provided by a plate heat exchanger and a glycol loop constitute the flexible LT load. The MT flexible load consists of one open vertical display case and a false load provided by a plate heat exchanger and glycol loop.

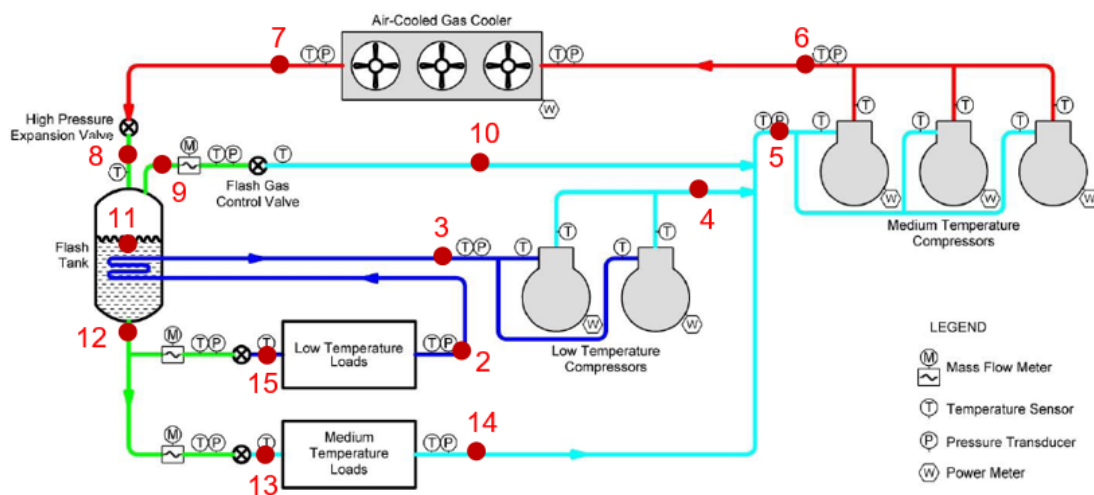


Figure 1. System diagram of commercial refrigeration system

3.2.1.2 Main Assumptions

The following assumptions were made for development of the models to predict the display case temperatures and refrigeration system power consumption.

- The air is well mixed inside the display case and has a uniform temperature profile.

- The impact of display case lighting is negligible.
- All resistances and capacitances of display case models are assumed to be time invariant.
- Only sensible load is considered in display case models.
- As the compressor power is the dominant power use, the focus of the model is to predict the compressor power consumption changes.

3.2.2 Modeling of Physics of Commercial Refrigeration Systems and Display Cases

3.2.2.1 Modeling Strategy

The commercial refrigeration system can be broken down into three components: thermal mass, equipment, and controls (Figure 2). The thermal mass can be thought of as the battery portion of the virtual battery system. It stores heat (or in the case of cooling, lack of heat) for later use. The equipment is what is used to heat or cool the thermal mass and is analogous to the power conversion system of a conventional electrical battery storage system. It converts one type of energy to another type that is compatible with the battery. Its function is to perform the work for the system. The controls are the final component. The controls use data from sensors within the thermal mass and set point inputs to make control decisions on how and when the equipment should run to charge the battery. This system is a virtual battery system in the sense that, unlike a physical battery, it doesn't store electricity but manipulates the work to heat or cool the thermal mass over time considerations to return the safe effects of storing electricity for future use.

The thermal model for an open display case consists of two coupled ordinary differential equations: one representing the temperature of the air in the case and the other representing the temperature of the product (i.e., food). The physical heat transfer to or from the case includes conduction/convection losses through wall panels, heat transfer between the air and the food, cooling done by the refrigeration system, heat from case fans and lights, and infiltration of the surrounding air. A closed display case can be modeled with the same equations; however, the term for infiltration will be significantly reduced or eliminated. Parameters can be estimated using physical data from the display case, and these estimated parameters can be used to set the upper and lower bounds. These bounds can then be used with a training routine to determine the best values for any particular system based on historical data.

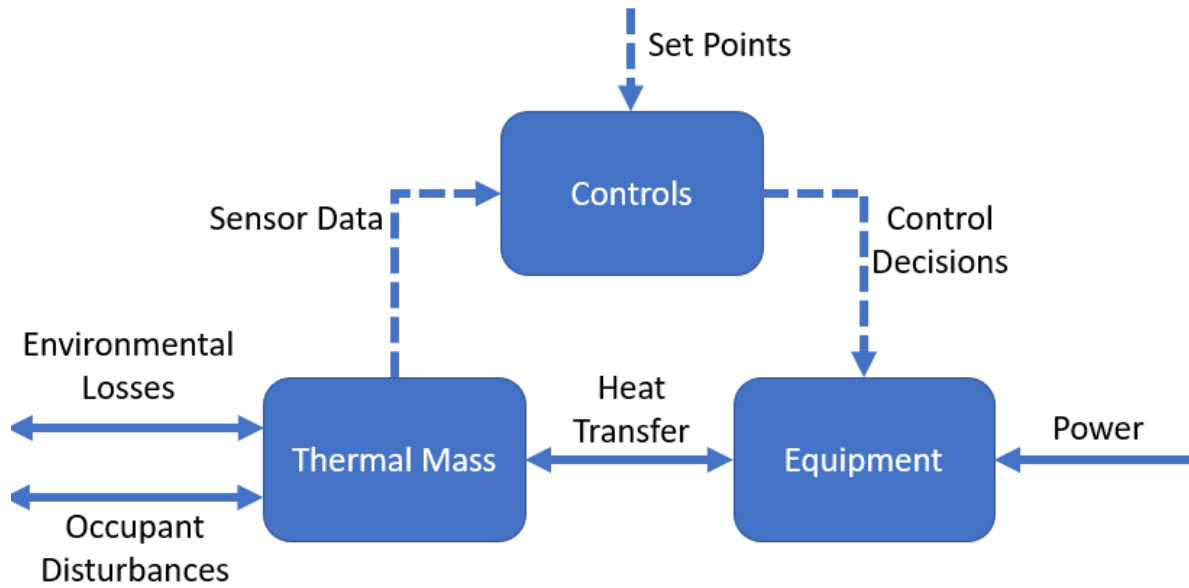


Figure 2. Generic virtual battery system broken down into components of thermal mass, equipment, and controls

The equipment model needs to provide a way to convert the heat transfer to or from the thermal storage to the electrical power consumption of the equipment. The greatest power consumers in a commercial refrigeration system are the compressors. Compressor manufacturers provide performance data on the compressors at various conditions or states. Performance curves based on these data will be developed for validation with the test data.

The system controls are the typical communication path between the equipment and an outside system. Some control systems may have built-in inputs for providing demand response capability. This allows for simple control inputs that will yield a predetermined response. However, many control systems do not have these types of inputs built in. For these systems, it is necessary to understand how typical control inputs (e.g., set points) are translated into equipment commands so the desired equipment response can be achieved. For many systems simple ON/OFF commands are the easiest method for obtaining a known response from the system. Other control options may provide different charge or discharge responses, higher efficiencies relative to ON/OFF control, and result in less wear and tear on the equipment, making it desirable to evaluate these options.

3.2.2.2 Display Case Model

Simplified gray-box refrigerator (case) thermal models were developed for both MT and LT display cases, and parameters were trained based on measured data from supermarket CO₂ refrigeration systems.

Outline of Mathematical Model

As shown in Figure 3, a 3R3C model structure is proposed for both MT and LT display cases. It is in an electrical analogue pattern with thermal resistance (R , in kelvins per watt) and thermal capacitance (C , in joules per kelvin). The physical properties of a CO₂ refrigerator case affecting thermal transfer are mainly those of the display case envelope, internal air, and food, which are

handled separately in this model. The developed model can therefore reflect the thermal status and response of different components in the display case.

The heat transfer in the display case model is described using the following first-order differential equations:

$$C_{air} \frac{dT_{ave}(t)}{dt} = \frac{T_{amb}(t) - T_{ave}(t)}{R_{infil}} + \frac{T_{food}(t) - T_{ave}(t)}{R_{food}} + \frac{T_{case}(t) - T_{ave}(t)}{R_{case}} + C1 \cdot Q_{AC,i}, \quad (1)$$

$$C_{food} \frac{dT_{food}(t)}{dt} = \frac{T_{ave}(t) - T_{food}(t)}{R_{food}}, \quad (2)$$

$$C_{case} \frac{dT_{case}(t)}{dt} = \frac{T_{ave}(t) - T_{case}(t)}{R_{case}} + C1 \cdot Q_{AC,m}. \quad (3)$$

C_{air} , C_{food} and C_{case} are the thermal capacitances of case air, food, and display case respectively. R_{food} and R_{case} are the thermal resistance between the air and the food and the air and the case respectively. R_{infil} is the thermal resistance of air infiltration for the MT (open) case or the thermal resistance of the glass wall for the LT (closed) case. Q_{AC} is the total cooling capacity (W) of the refrigeration supplied to the case. Unknown factors for Q_{AC} include the sensible heat ratio and the installed inefficiencies such as long refrigerant lines, low evaporator airflow, dirty coils, improper refrigerant charge, etc. Therefore, $C1$ is introduced to adjust Q_{AC} for unknown factors.

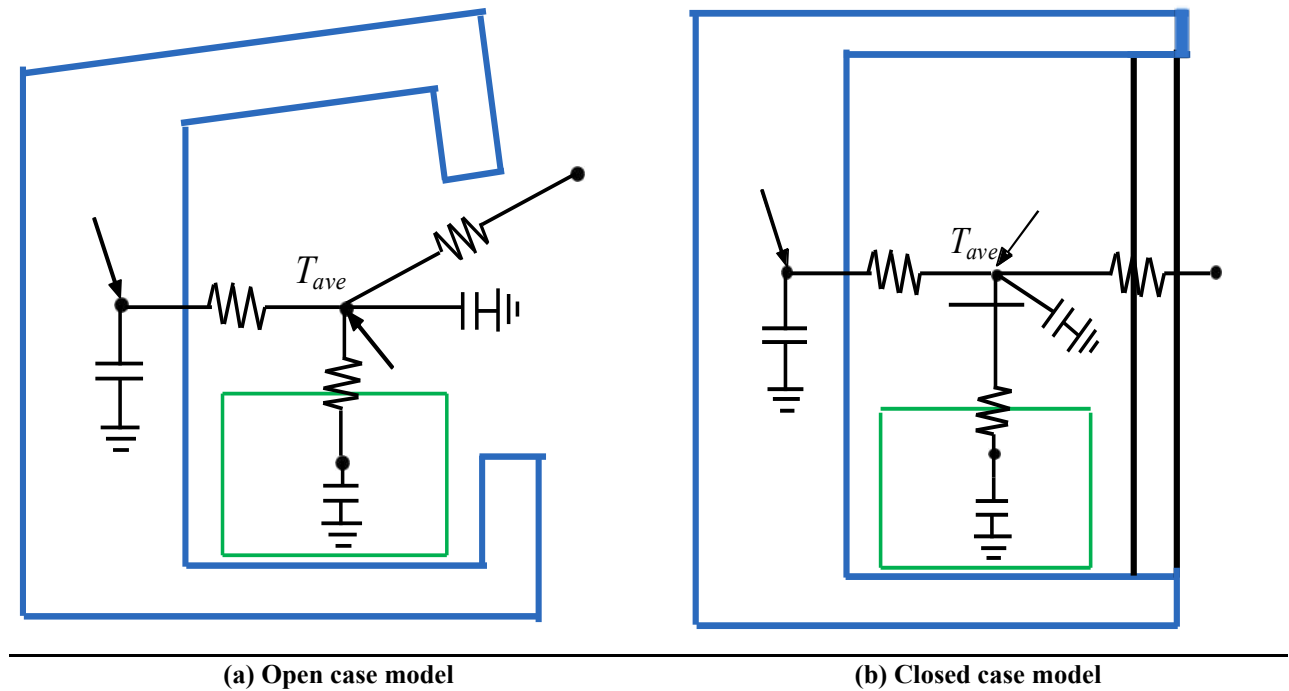


Figure 3. Schematic of simplified CO₂ supermarket refrigerator display case models. (3R3C, where R = thermal resistance in kelvins per watt and C = thermal capacitance in joules per kelvin).

Portions of $CI \cdot Q_{AC}$, i.e., $CI \cdot Q_{AC,i}$, are transmitted to the case air directly by convection and the rest, i.e., $CI \cdot Q_{AC,m}$, is absorbed by the refrigerator case where the subscripts i and m indicate the case air and internal mass respectively. They are calculated by the following equations:

$$C1 \cdot Q_{AC,i} = Sp1 \cdot C1 \cdot Q_{AC}, \quad (4)$$

$$C1 \cdot Q_{AC,m} = (1 - Sp1) \cdot C1 \cdot Q_{AC}, \quad (5)$$

where, $Sp1$ is the convection fraction for Q_{AC} , which is assumed to be unknown and needs to be identified by the searching algorithm.

Parameter Identification

The searching process for optimal values of the undetermined parameters in this model is a nonlinear optimization process. Given a set of parameters, the gray-box model can predict both the air in the case (T_{ave}) and food (T_{food}) temperature profiles. An objective function is used to evaluate the fitness between the predicted results and measured data collected from the reference system during the training period. The objective function J of such optimization is to minimize the integrated root mean square errors (RMSEs) of both T_{ave} and T_{food} , as defined in Eq. (6):

$$J(R_{case}, R_{food}, R_{infil}, C_{air}, C_{food}, C_{case}, C_1, Sp) = \sqrt{\frac{\sum_{k=1}^N (T_{ave,act} - T_{ave,simu})^2}{N-1}} + \sqrt{\frac{\sum_{k=1}^N (T_{food,act} - T_{food,simu})^2}{N-1}} \quad (6)$$

where, $T_{ave,act}$ and $T_{food,act}$ are the measured case air temperature and food temperature. $T_{ave,simu}$ and $T_{food,simu}$ are the results for the case air temperature and food temperature from the model. The parameters are identified by the particle swarm optimization (PSO) method. PSO is a computational method that optimizes a problem by iteratively trying to improve a candidate solution with respect to a given measure of quality. It solves a problem by having a population of candidate solutions and moving these particles around in the search space according to simple mathematical formulae over the particle's position and velocity.

The model development is written and the PSO package is imported in Anaconda (Pyswarm N.D.), which is a free, open-source, integrated development environment for Python.

3.2.2.3 Refrigeration System Model

Mathematical Equations

The thermodynamic cycle of the commercial refrigeration system is represented by the pressure-enthalpy diagram in Figure 4. The mathematic models for the major components are described in the following subsections.

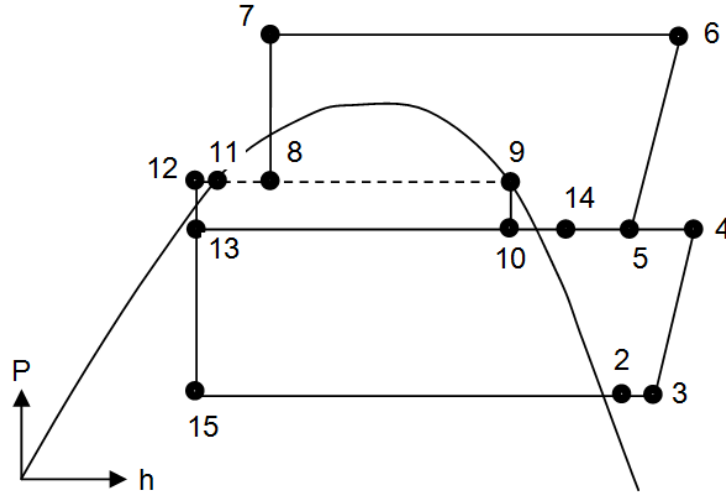


Figure 4. Commercial refrigeration system pressure-enthalpy (P-h) diagram

LT Evaporator:

The LT refrigeration capacity is calculated by multiplying the refrigerant mass flow rate through the evaporator by the enthalpy difference between evaporator inlet and outlet, given by

$$Q_{LT} = m_s(h_2 - h_{15}), \quad (7)$$

where Q_{LT} is the LT refrigeration capacity, m_s is the LT compressor suction mass flow rate, and h_{15} and h_2 are the LT evaporator refrigerant inlet and outlet enthalpies, respectively.

LT Compressor:

The LT compressor suction-side mass flow rate is

$$m_s = \rho_2 V_2, \quad (8)$$

where V_2 is the suction volumetric flow rate, which can be estimated by the formula in Eq. (9) (Bourdhouxhe, Grodent, and Lebrun 1999):

$$V_2 = \left\{ 1 - \frac{V_{LT_cl}}{V_{LT_disp}} [(P_e / P_s)^{1/\gamma} - 1] \right\} N_{LT_comp} V_{LT_disp}, \quad (9)$$

where V_{LT_cl} is the LT reciprocate compressor clearance volume, V_{LT_disp} is the LT reciprocate compressor displacement volume, N_{LT_disp} is the LT compressor rotational speed, and P_s and P_m are the LT compressor suction-side and discharge-side (economizer side) pressures, respectively. γ is refrigerant constant.

The suction-side refrigerant density is a function of the corresponding pressure and temperature, with the assumption that the refrigerant is a superheated vapor at this state:

$$\rho_2 = f(T_2, P_s). \quad (10)$$

The LT compressor power consumption is calculated with Eq, (11) (Bourdhouxhe, Grodent, and Lebrun 1999):

$$W_{LT} = \left(\frac{\gamma}{1 - \gamma}\right) \left[\left(\frac{P_e}{P_s}\right)^{\gamma-1/\gamma} - 1 \right] P_s V_2 / \eta_{LT} , \quad (11)$$

where η_{LT} is the LT compressor overall efficiency.

Similarly, for MT we have the following equations.

MT Evaporator:

$$Q_{MT} = m_d (h_{14} - h_{13}), \quad (12)$$

where Q_{MT} is the MT refrigeration capacity, m_d is the MT compressor suction mass flow rate, and h_{13} and h_{14} are the MT evaporator refrigerant inlet and outlet enthalpies, respectively.

MT Compressor:

$$m_d = \rho_5 V_5 , \quad (13)$$

$$V_5 = \left\{ 1 - \frac{V_{MT_cl}}{V_{MT_disp}} [(P_d / P_e)^{1/\gamma} - 1] \right\} N_{MT_comp} V_{MT_disp} , \quad (14)$$

$$\rho_5 = ref(T_5, P_e), \quad (15)$$

$$W_{MT} = \left(\frac{\gamma}{1 - \gamma}\right) \left[\left(\frac{P_d}{P_e}\right)^{\gamma-1/\gamma} - 1 \right] P_e V_5 / \eta_{MT} , \quad (16)$$

where V_5 is the suction volumetric flow rate, V_{MT_cl} is the MT reciprocate compressor clearance volume, V_{MT_disp} is the MT reciprocate compressor displacement volume, N_{MT_disp} is the MT compressor rotational speed, and P_e and P_d are the MT compressor suction-side (economizer side) and discharge-side pressures, respectively. γ is refrigerant constant.

Condenser/Gas Cooler:

$$Q_{cond} = m_d (h_6 - h_7) , \quad (17)$$

$$Q_{air} = m_a c_{pa} (T_{a_lvg} - T_{a_ent}) , \quad (18)$$

$$Q_{max} = C_{min} (T_{ref_ent} - T_{a_ent}), \quad (19)$$

where Q_{cond} and Q_{air} represent the condenser/gas cooler heat transfer capacity calculated from refrigerant side and air side, respectively. Q_{max} is the maximum possible heat transfer capacity of the condenser/gas cooler, and h_6 and h_7 are the condenser/gas cooler refrigerant inlet and outlet enthalpies, respectively. m_a is condenser/gas cooler air mass flow rate; T_{a_ent} and T_{a_lvg} are the air temperature entering and leaving the condenser/gas cooler, respectively; and T_{ref_ent} is the condenser/gas cooler refrigerant inlet temperature.

$$Q_{cond} = Q_{air} = \varepsilon Q_{max}, \quad (20)$$

$$C_{min} = \min(m_d C_{pr}, m_a C_{pa}), \quad (21)$$

$$C_{max} = \max(m_d C_{pr}, m_a C_{pa}), \quad (22)$$

where ε is the condenser/gas cooler effectiveness, which can be calculated through the number of transfer units, as shown in Eqs. (23) - (25).

For a single-phase zone (Threlkeld 1962)

$$\varepsilon = 1 - \exp\left[\frac{\exp(-k \times Ntu \times C) - 1}{k \times C}\right], \quad (23)$$

where C is the capacity ratio,

$$C = C_{min} / C_{max}. \quad (24)$$

For a two-phase zone (Bourdhouxhe, Grodent, and Lebrun 1999)

$$\varepsilon = 1 - \exp[-Ntu]. \quad (25)$$

High-Side Expansion Valve (Xue, Shi, and Ou 2008):

$$m_{hpxv} = m_d = k_{hpxv} C_{v_{hpxv}} \sqrt{\rho_7 (P_7 - P_8)} \quad (26)$$

Low-Side Expansion Valve (Xue, Shi, and Ou 2008):

$$m_{eev_{LT}} = m_s = k_{eev_{LT}} C_{v_{eev_{LT}}} \sqrt{\rho_{12} (P_{12} - P_{15})} \quad (27)$$

$$m_{eev_{MT}} = k_{eev_{MT}} C_{v_{eev_{MT}}} \sqrt{\rho_{12} (P_{12} - P_{13})} \quad (28)$$

Reduced Model

Solving for the above system model [Eqs. (7) - (28)] can provide the cooling capacities for the display case models and the power consumption for the control model/optimization. However, it is not practical to integrate the models for the entire refrigeration system into the display case thermal model and control optimization. Thus, further simplification is necessary for predicting the cooling load and power use. Based on data provided by the compressor manufacturer, we developed a reduced model that can be integrated into the display case thermal model and control model/optimization.

For the LT refrigeration cycle,

$$W_{LT} = a_0 + a_1 SST + a_2 SST^2 + a_3 SMT + a_4 SMT^2 + a_5 SST \cdot SMT, \quad (29)$$

$$Q_{LT} = a_6 + a_7 SST + a_8 SST^2 + a_9 SMT + a_{10} SMT^2 + a_{11} SST \cdot SMT, \quad (30)$$

where, SST is the saturation suction temperature for the LT compressor; SMT is the saturation middle stage temperature, which is equivalent to the saturation discharge temperature for the LT compressor; and $a_0, a_1 \dots a_{11}$ are parameters that can be calibrated with compressor manufacturer data.

For the MT refrigeration cycle,

$$W_{MT} = CF_{MT} \times (b_0 + b_1SMT + b_2SMT^2 + b_3SDT + b_4SDT^2 + b_5SMT \cdot SDT), \quad (31)$$

$$Q_{MT} = CF_{MT} \times (b_6 + b_7SMT + b_8SMT^2 + b_9SDT + b_{10}SDT^2 + b_{11}SMT \cdot SDT), \quad (32)$$

where, SMT is the saturation middle stage temperature, which is equivalent to the saturation suction temperature for the MT compressor; SDT is the saturation discharge temperature for the MT compressor; $b_0, b_1 \dots b_{11}$ are parameters that can be calibrated through compressor manufacture data; and CF_{MT} is the correction factor for partial load operation of the compressor with variable frequency drive (4MTC_10K). The CF_{MT} can be calculated by either saturated temperature (SMT and SDT) or partial load ratio (PLR):

$$CF_{MT} = k_0 + k_1SMT + k_2SDT + k_3SMT \cdot SDT, \quad (33)$$

$$CF_{MT} = k_0 + k_1PLR + k_2(PLR)^2 + k_3(PLR)^3. \quad (34)$$

Simplified Reduced Model

To integrate with the control/optimization model, the current model input variables, SST, SMT, and SDT, are approximated based on ambient temperature and the suction saturation set point temperatures of the refrigeration system.

As stated in the manual provided by Hillphoenix, “Suction gas from the low-temperature display case and freezer evaporators enters the low-temperature subcritical compressors at around 200 psig, well below the critical point for CO₂. The low-temp discharge gas at about 400 psig, then combines with the medium-temp suction gas from the medium-temp display cases and walk-in cooler evaporators before entering the medium-temp transretinal compressor . . .” (Hill Phoenix 2013).

Therefore, the LT compressor suction pressure is a controlled variable that can be set by an operator through the controller panel. The test data on supermarket CO₂ refrigeration systems indicates that the LT compressor suction pressure is around 182 psig (SST = -25.6°F), and the discharge pressure is around 395 psig (SMT = 16°F).

The refrigeration system manual provides details on the control of the condenser fan and high-pressure control valve (Xue, Shi, and Ou 2008).

- $T_{amb} < 41^\circ\text{F}$
Condenser fan is off; ICMT controls the discharge pressure to maintain 3°F subcooling at the condenser exit.
- $41^\circ\text{F} < T_{amb} < 72^\circ\text{F}$
Condenser fan is on, adjusting speed to maintain 5°F temperature difference between ambient temperature and condenser discharge saturated liquid temperature. ICMT controls the discharge pressure to maintain 3°F subcooling temperature.
- $72^\circ\text{F} < T_{amb} < 77^\circ\text{F}$

Condenser fan is on, adjusting speed to maintain 77°F condenser discharge saturated liquid temperature. ICMT controls the discharge pressure to maintain 3°F subcooling at the condenser exit.

- 77°F < T_{amb} < 83°F
Condenser fan is on, running full speed. ICMT controls the discharge pressure to optimal pressure.

Based on the control strategy and actual test data, the relationship between ambient temperature and condenser out saturated discharge temperature (SDT) is shown in Figure 5.

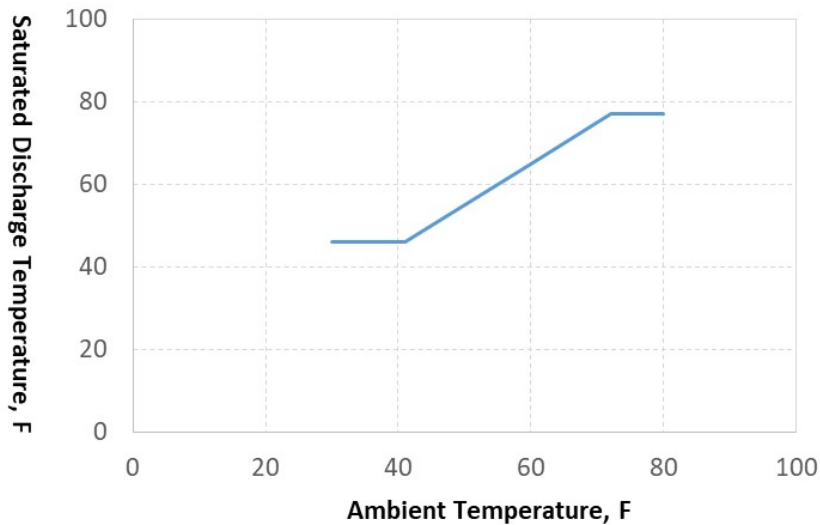


Figure 5. Relationship between ambient temperature and saturated discharge temperature

T _{amb} < 41°F:	SDT = 46.791 - 0.0214T _{amb}
41°F ≤ T _{amb} < 72°F:	SDT = T _{amb} + 5
T _{amb} ≥ 72°F:	SDT = 77°F

3.2.2.4 Control Model

According to the manufacturer’s manual (Hill Phoenix 2013), the Danfoss AK-PC controller is used for the refrigeration system capacity control. The calculation of the requested compressor capacity takes place on the basis of a proportional integral (PI) controller, which divides capacity range into five different control zones according to the suction pressure value. The zone timer, defined as the integration time of the PI controller whenever the suction pressure is in the zone, is used to slow/speed the PI controller. The “requested capacity” from the PI controller shows the actual requested compressor capacity. The integrator is looking at the deviation between the set point and the current suction pressure and increases/reduces the requested capacity accordingly. The controller will start extra compressor capacity if requested capacity has increased to a value that allows the next compressor step to start. Similarly, the controller will stop compressor capacity if the requested capacity has decreased to a value that allows the next compressor step to stop.

To model this capacity control, the requested capacity (Q_{LTreq} and Q_{MTreq}) will be calculated by the load demand side (display case and false load). The available capacity (Q_{LT} and Q_{MT}) will be given based on the compressor model, and the required number of compressors (N_{LTcomp} and N_{MTcomp}) is given by the following.

For LT compressors

$$N_{LTcomp} = \begin{cases} 1, & \text{if } Q_{LTreq} \leq Q_{LT1} \\ 2, & \text{if } Q_{LTreq} > Q_{LT1} \end{cases} \quad (35)$$

For MT compressors

$$N_{MTcomp} = \begin{cases} 1, & \text{if } Q_{MTreq} \leq Q_{MT1} \\ 2, & \text{if } Q_{LM1} < Q_{LTreq} \leq (Q_{MT1} + Q_{MT2}) \\ 3, & \text{others} \end{cases} \quad (36)$$

Where Q_{LT1} , Q_{LT2} , Q_{MT1} , Q_{MT2} , and Q_{MT3} are available compressor (LT/MT) capacities at current operating conditions and can be calculated through Eqs. (30) and (32).

The PLRs for variable speed compressors are given by the following

$$PLR_{LT} = 100\% \times \left[\frac{Q_{LTreq} - (N_{LTcomp} - 1)Q_{LT2}}{Q_{LT1}} \right] \quad (37)$$

$$PLR_{MT} = 100\% \times \left[\frac{Q_{MTreq} - \text{Min}(1, N_{MTcomp} - 1)Q_{MT2} - \text{Max}(0, N_{MTcomp} - 2)Q_{MT3}}{Q_{MT1}} \right] \quad (38)$$

The total power consumption of LT and MT are given by the following.

$$W_{LT_tot} = W_{LT1} + (N_{LTcomp} - 1)W_{LT2} \quad (39)$$

$$W_{MT_tot} = W_{MT1} + \text{Min}(1, N_{MTcomp} - 1)W_{MT2} + \text{Max}(0, N_{MTcomp} - 2)W_{MT3} \quad (40)$$

3.3 Test Hardware

3.3.1 Commercial Refrigeration Systems and Display Cases Tested

The laboratory setup for the commercial refrigeration system consists of a transcritical CO₂ compressor rack, one MT and one LT refrigerated display case, an air-cooled gas cooler, and MT and LT false loads. As shown in Figure 1 and Figure 6, the liquid CO₂ leaving from the flash tank flows through the display cases (both LT and MT) and false load heat exchangers (both LT and MT) to remove their heat loads. The superheated CO₂ leaving from the LT display cases and LT false load heat exchanger returns to the LT compressors. The superheated CO₂ leaving from the MT display cases and MT false load heat exchanger mixes with CO₂ from the flash tank vapor outlet and the LT compressors' discharge and then enters the MT compressors. The compressed CO₂ from the MT compressors flows into the air-cooled gas cooler and is cooled by

outside air. The cooled CO₂ is throttled by the high-pressure side expansion valve and flows into the flash tank.

The overall cooling capacity of this commercial refrigeration system is ~12.2 tons with LT cooling capacity of ~2.6 tons at -22°F evaporating temperature and MT cooling capacity of ~9.6 tons at 20°F evaporating temperature. The LT load consists of one four-door display case and an LT false load provided by a plate heat exchanger, two 3 kW electric heaters, and a glycol loop. The MT load consists of one open display case and an MT false load provided by a plate heat exchanger, nine 3 kW electric heaters, and a glycol loop.



Figure 6. Commercial refrigeration system

Compressor Rack

The compressor rack contains two LT compressors and three MT compressors using CO₂ refrigerant. Each set of compressors consists of one primary variable-speed compressor (capable of modulating capacity from 10% to 100%) and one or two secondary fixed-speed compressors. The facility is equipped with two sets of reciprocating compressors (MT and LT). The LT compressors operate in the subcritical zone, and the MT compressors can operate in both the subcritical zone and the supercritical zone. When the refrigeration load is low, the refrigeration load is satisfied by the primary variable-speed compressor, which can modulate its capacity according to the load demand, and the secondary fixed-speed compressor is turned off. If the load exceeds the capacity of the primary variable-speed compressor, the secondary fixed speed compressors will be brought online, and the primary variable-speed compressor will modulate its capacity to match the load. Expansion valves are used to regulate the suction pressure of the MT and LT compressors independently. The target suction pressures (or suction saturation temperatures) are set based on the coldest temperature required by the display cases that those compressors serve (either MT or LT). Each case has a temperature set point, and the refrigerant flow to the evaporator coil of the case is modulated to maintain this temperature. Therefore, it is

possible to control the refrigeration system power consumption by changing these set points in addition to more traditional ON/OFF means like shutting down a compressor or compressors or shutting off refrigerant flow to one or more display cases. Each of these “control levers” will result in different system power and thermal responses. Specifications for the compressors are shown in Table 1.

Table 1. Compressor Specifications for Laboratory Setup

Compressor type	Temperature level	Capacity control	Model	Refrigerating capacity, kBtu/h (kW) ^a	Power (kW) ^a
Reciprocating	LT	Variable	2KSL-1K	19.0 (5.57)	1.34
Reciprocating	LT	Fixed	2MSL-07K	12.0 (3.52)	0.82
Reciprocating	MT	Variable	4MTC-10K	38.0 (11.1)	9.66
Reciprocating	MT	Fixed	4MTC-10K	39.0 (11.4)	9.72
Reciprocating	MT	Fixed	4MTC-7K	38.5 (11.3)	9.4

^aRefrigerating capacity and power are given for the following operating conditions using R-744 (CO₂):

LT: -22°F (-30°C) evaporating temperature, 20°F (-6.7°C) condensing temperature

MT: 20°F (-6.7°C) evaporating temperature, 100°F (38°C) condensing temperature



Figure 7. Low temperature display case



Figure 8. Medium temperature display case

Refrigerated Display Cases and False Loads

The LT load consists of a four-door vertical display case (Figure 7), 10 ft (3.0 m) long, and a false load provided by a plate heat exchanger, two electric heaters, and a glycol loop. The rated capacity of the four-door display case is 5,700 Btu/h (1,670 W), and the false load is about 20,500 Btu/h (6,000 W). The MT load consists of one open vertical display case (Figure 8), 8 ft (2.4 m) long, and a false load provided by a plate heat exchanger, nine electric heaters, and a glycol loop. The rated capacity of the open display case is 9,600 Btu/h (2,810 W), and the false load is about 92,000 Btu/h (27,000 W). Specifications for the display cases are shown in Table 2.

Table 2. Specifications for Refrigerated Display Cases

	Low Temperature Display Case	Medium Temperature Display Case
Model Number	6RZLH	O5DM-NRG
Type	4-door, vertical multi-deck	Open, vertical multi-deck
Length	10 ft (3.0 m)	8 ft (2.4 m)
Rated Capacity	5,700 Btu/h (1,670 W)	9,600 Btu/h (2,810 W)
Fan Amperage	0.93 amps	0.75 amps
Lighting Amperage	0.90 amps	0.40 amps
Antisweat Heater Amperage	7.99 amps	N/A
Defrost Type	Electric	Off-cycle
Defrost Amperage	16.29 amps	N/A

Air-Cooled Gas Cooler

The Luvata (model LGV8812) air-cooled gas cooler, equipped with two variable speed fans, is used to reject heat from the refrigeration system. The gas cooler receives superheated refrigerant from the MT compressors and rejects heat to the outdoor air delivering either subcooled liquid refrigerant (during subcritical operation) or LT vapor (during transcritical operation) to the flash tank. The rated heat rejection capacity of this air-cooled gas cooler is 268,000 Btu/h (78.5 kW) for CO₂ at an entering temperature of 242°F (117°C) and an exit gas temperature of 97.5°F (36.4°C).

3.3.2 Testing Hardware and Data Acquisition Setup

Controls

The refrigeration system is controlled through a Danfoss AK-SC 355 system controller. The main control functions include the following.

- Compressor control to maintain the suction pressure set points for the LT and MT refrigeration circuits.
- High pressure expansion valve control to maintain optimum high-side pressure.
- Condenser fan speed control to maintain condensing pressure.

The display cases are controlled by Danfoss AK-CC 550A case controllers that communicate with the system controller and regulate the expansion valve operation, display case air temperature, defrost operation, and lighting and fan operation.

The false loads are controlled through electronic expansion valves located in the upstream refrigerant pipes entering the false load heat exchangers. The electronic expansion valves are used to maintain 15k of refrigerant superheat temperature leaving the false load heat exchangers.

Instrumentation

The commercial refrigeration system is fully instrumented to measure its performance. The measurements include refrigerant temperatures and pressures at each of the major component inlets and outlets, such as compressors, display cases, false load heat exchangers, expansion valves, and the gas cooler. Additional measurements include refrigerant mass flow rate of loads and power consumption of compressors, gas cooler fans, and false load heaters. A detailed list of the measurement points and specifications of the instrumentation are given in Table 3.

Table 3. Measurement Points and Instrument Specifications

Measured Variable	Instruments	Range	Accuracy
Power			
MT 1 st compressor power	Watt transducer	0 - 80,000 W	±5% of reading
MT 2 nd compressor power		0 - 80,000 W	
MT 3 rd compressor power		0 - 80,000 W	
LT 1 st compressor power		0 - 8000 W	
LT 2 nd compressor power		0 - 8000 W	
Mass Flow Rate			
MT evaporator mass flow rate	Coriolis mass flow meter	0 - 10kg/min	±0.05%
LT evaporator mass flow rate		0 - 10kg/min	
Flash tank bypass mass flow rate		0 - 10kg/min	
LT false load mass flow rate	Positive displacement flow meter	0.11 - 26.4 L/min	
MT false load mass flow rate		0.11 - 26.4 L/min	
Temperature			
MT display case suction temperature	Thermocouple	-270- 400 °C	Greater of 1.0°C or 0.75% for 0 to 350°C)
LT display case suction temperature			
Flash tank vapor outlet temperature			
Gas cooler inlet/outlet temperature			
MT compressor rack inlet/outlet temperature			
LT compressor rack inlet/outlet temperature			
MT 1 st compressor suc./dis. temperature			
MT 2 nd compressor suc./dis. temperature			
MT 3 rd compressor suc./dis. temperature			
LT 1 st compressor suc./dis. temperature			
LT 2 nd compressor suc./dis. temperature			
Pressure			
MT display case suction pressure	Pressure transducer	0 - 14 Mpa	±0.25% full scale
LT display case suction pressure		0 - 7 Mpa	
Flash tank vapor outlet pressure		0 - 14 Mpa	
Gas cooler inlet/outlet pressure		0 - 14 Mpa	
MT compressor rack inlet/outlet pressure		0 - 14 Mpa	
LT compressor rack inlet pressure		0 - 7 Mpa	
LT compressor rack outlet pressure		0 - 14 Mpa	

The enthalpy of the refrigerant at different points in the system was determined using pressure and temperature measurements and ensuring that the refrigerant was single-phase at all measurement points. Placement of refrigerant-side instrumentation can be seen in Figure 1. Air temperature within the display case was measured at multiple points in the product storage area in addition to return and supply air temperatures to and from the case evaporator coil. Sample data from the operation of an MT refrigeration case is shown in Figure 9.

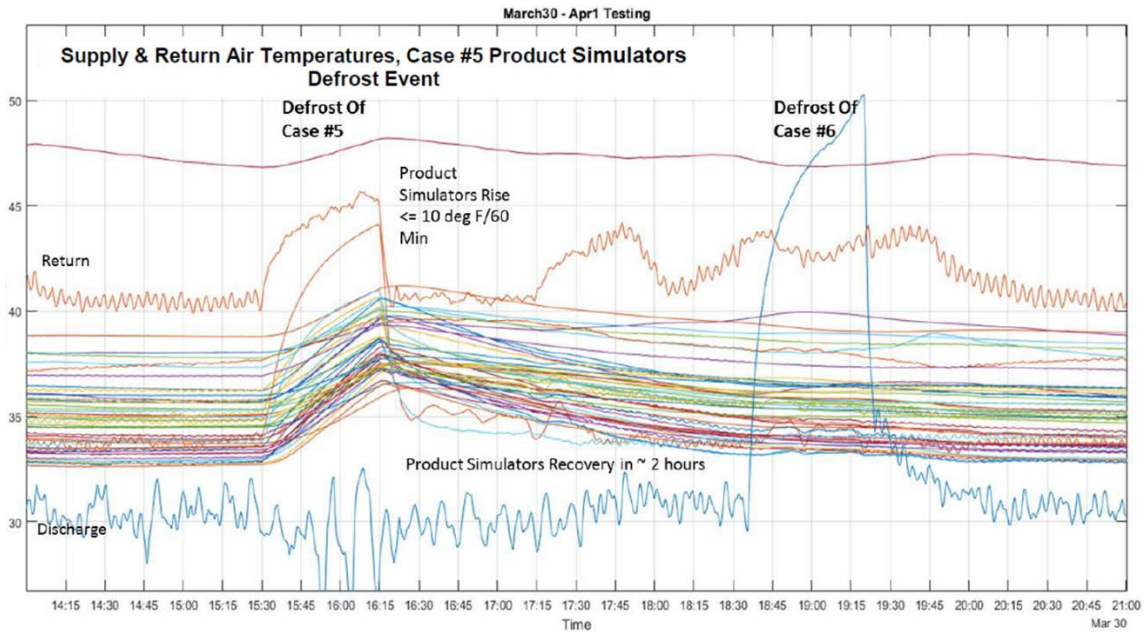


Figure 9. Sample data showing product temperatures of a medium temperature refrigeration case during and after a defrost cycle

3.4 Test Procedures

3.4.1 Relevant Standards and Test Methods

The Energy Policy and Conservation Act (EPCA) set forth requirements that manufacturers test and certify their appliances, devices, and equipment to comply with applicable energy conservation standards as part of the Energy Conservation Program for Consumer Products. The US Department of Energy (DOE) has test procedures for rating walk-in cooler panels, doors, and refrigeration equipment; commercial freezers and refrigerators; commercial ice makers; and refrigerated bottled or canned beverage vending machines. In accordance with EPCA, test procedures shall be reasonably designed to produce test results that measure energy efficiency, energy use, or estimated annual operating cost of a covered product during a representative average use cycle or period of use and must not be unduly burdensome to conduct. Commercial refrigeration equipment is included as a covered product in EPCA, and thus is subject to the energy conservation test procedures developed by DOE.

The CFR includes a test procedure for rating commercial refrigerators, freezers, and refrigerator-freezers and energy conservation standards for the following equipment categories.

- Remote Condensing Commercial Refrigerators and Commercial Freezers
- Self-Contained Commercial Refrigerators and Commercial Freezers without Doors
- Self-Contained Commercial Refrigerators and Commercial Freezers with Doors

- Self-Contained Commercial Refrigerators with Transparent Doors for Pull-Down Temperature Applications
- Commercial Ice Cream Freezers (Remote Condensing and Self-Contained)

Test Procedures

The CFR includes two test procedures for commercial refrigerators, freezers, and refrigerator-freezers. For equipment tested after October 20, 2014, and before March 28, 2017, the test procedure in Appendix A to Subpart C of 10 CFR 431 should be used. For equipment tested on or after March 28, 2017, the test procedure in Appendix B to Subpart C of 10 CFR 431 should be used. This report will focus on the Appendix B test procedure as it is applicable to equipment currently being manufactured.

The Appendix B test procedure references the test procedure in industry standard AHRI 1200 (I-P)-2010 and specifically sections 3, 4, and 7, with section 6 being applicable to self-contained condensing units and section 5 being applicable to remote condensing units. AHRI 1200 (I-P)-2010 requires tests to be performed according to ANSI/ASHRAE 72-2005.

The rating test requires a 24-hour test of the refrigerator or freezer with ambient conditions held constant at 75.2°F dry bulb temperature and 64.4°F wet bulb temperature. The equipment is tested with test simulators and filler packages loaded into the product storage space. The test simulators consist of a plastic container of at least 1 US liquid point of volume with a lid conforming to the dimensions shown in Figure 10. The simulator is filled with any natural or artificial sponge material that is saturated with a solution consisting of a 50 : 50 ±2% mixture by volume of propylene glycol and distilled water. Test simulators are placed on the left and right end of the case and at 36 to 48 in. intervals across the width. At each location simulators are placed at the front and rear and at the top and bottom in contact with the manufacturer's load-limit boundaries. The temperature of these product simulators is measured over the test period and the average must be 38°F ±2°F for MT (refrigerator) applications, 0 ±2°F for LT (freezer) applications, and -15°F ±2°F for ice cream freezers. Filler packages containing material that closely approximates food product characteristics is used to fill the rest of the case to 70% to 90% of the net usable volume of the case (Figure 11).

For cases with remote condensing units, the refrigerant or coolant mass flow is measured at the inlet to the case, and the temperature and pressure are measured both entering and leaving the case. This allows for the cooling provided to the case to be measured during the test.

The 24-hour test period should begin with a defrost cycle, and the refrigerating “on” and “off” periods should be recorded throughout the test. A sample 24-hour test period is shown in Figure 12. During the 24-hour test period, cases with doors should be opened for 6 s, 6 times per hour, for 8 consecutive hours. Data are recorded at 3-minute intervals, and the electrical consumption of the case (and refrigeration system for self-contained units) is measured over the 24-hour test.

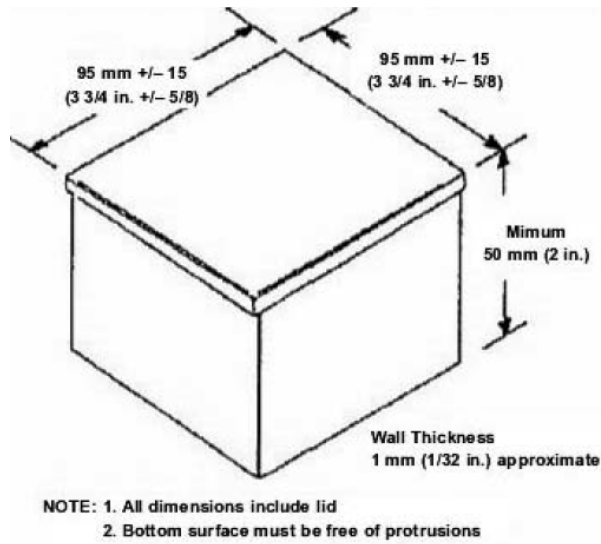


Figure 10. Test simulator dimensions from ASHRAE 72-2005

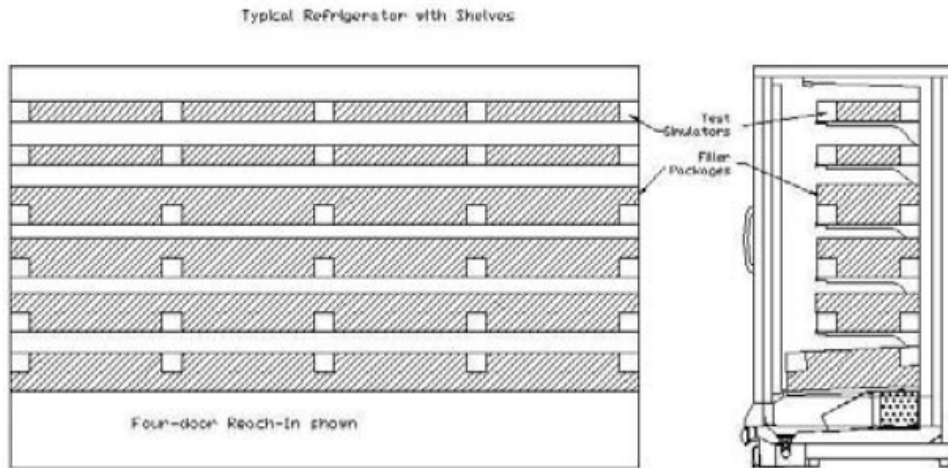


Figure 11. Typical test simulator location and filler material in a refrigerated case with shelves from ASHRAE 72-2005

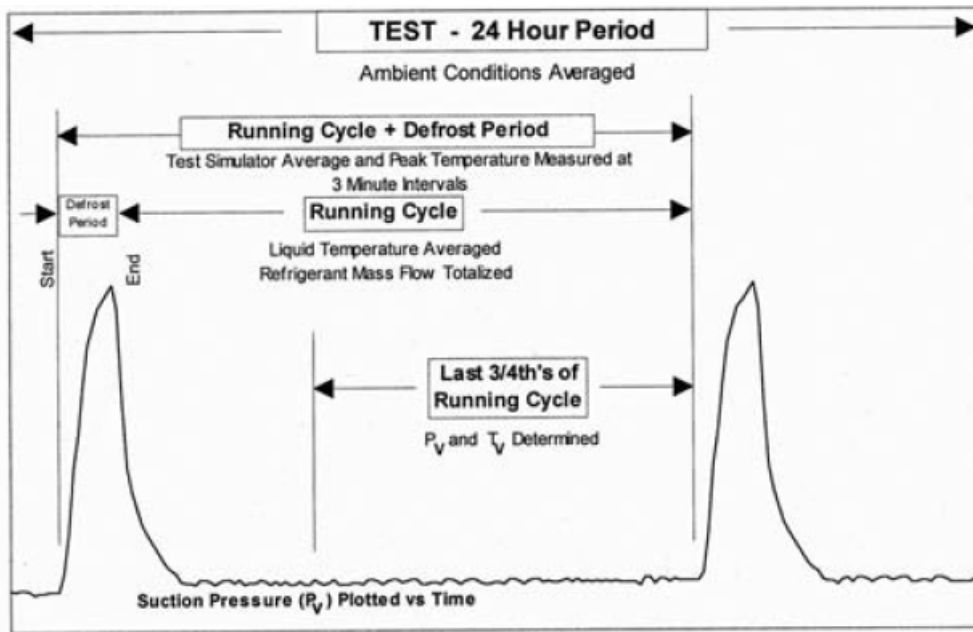


Figure 12. Example 24-hour test period from ASHRAE 72-2005

For remote condensing refrigerated cases, the total electrical load is measured and adjusted to determine the calculated daily energy consumption (CDEC). The CDEC includes electrical use of compressors; evaporator fan motors; lighting; surface anticondensate load, including fans and heaters; defrost heaters; condensate evaporator pans; and any other suitable electrical loads when they are part of the unit. For remote condensing cases, the compressor energy consumption is calculated based on the cooling delivered to the case during the 24-hour test divided by an energy efficiency ratio based on the adjusted dew point temperature of the refrigerant. The adjusted dew point temperature is 2°F lower than the measured dew point temperature for MT applications and 3°F lower for LT and ice cream applications to account for pressured drop between the case and compressor suction line.

For self-contained refrigerated cases, the total daily energy consumption (TDEC) is measured and includes energy use of compressors; evaporator fan motors; condensing fan motors; lighting; anticondensate loads, including fans and heaters; defrost heaters; condensate evaporator pans; and any other suitable electrical loads when they are part of the unit.

AHRI 1200 (I-P)-2010 includes calculations for adjusting the energy consumption (CDEC or TDEC) based on the inclusion of alternate components for both remote condensing and self-contained refrigeration equipment.

For self-contained refrigeration equipment, a calculated change in the energy use for the alternate component can be substituted for the energy use of the component used in the total energy test only if the alternate component uses less energy than the original component. However, a credit for reduction in compressor energy consumption due to the alternate component cannot be taken if a calculated value is used. A direct measurement of the total electrical load is required if the alternate component uses more energy than the original component or if it is desired to take a credit for the compressor energy reduction associated with the alternate component.

3.4.2 Characterization Test

The characterization test is a procedure for measuring all the physical and control parameters of a device and its controllers that are needed to define the performance of a fleet of devices for any foreseeable grid service. It focuses exclusively on the measurement of key parameters and does not involve time-series testing against actual, individual grid services as doing so would take too long and would limit the ability to develop ratings for grid services other than those specifically tested.

The characterization sequence outlined here may adopt parameters from existing test procedures that define a device’s power input and output capacities and rate of change, energy input and output conversion efficiencies, and energy storage capacity in various operational modes and conditions. To the extent these adopted parameters are insufficient for the purposes of this project, the characterization test will define a test apparatus and sequence of tests to measure the parameters.

In addition to these power- and energy-related parameters, grid services are generally also defined by the potential duration of device response and transition times or limits on changes from one operational state or mode to another. Measuring parameters that describe these limits is a key focus of the characterization tests. The transition times or limits may be a function of a device’s inherent physical properties or of its control systems. The characterization tests are designed to separately distinguish sources and their effects. The characterization tests are not designed to measure communication network time lags between the utility operator and the device controller as these vary with the network design and traffic levels. They are also not designed to test the communication protocols used by the manufacturers for their compatibility or interoperability with communication standards.

The commercial refrigeration system was tested to validate the device models and obtain parameters to define the fleet behavior under a variety of predefined conditions (drive cycles). This document details the test apparatus and data collection procedures for the commercial refrigeration system.

3.4.3 Baseline Test

The system will be baseline tested to determine capacity, efficiency, and power use at various indoor and outdoor conditions to characterize the typical operation of the system. Test conditions are shown in Table 4.

Table 4. Baseline Test Conditions

Test	Low Temperature Case (°F)	Medium Temperature Case (°F)	Outdoor Dry Bulb (°F)	Indoor Dry Bulb (°F)	Indoor Wet Bulb (°F)
1	-6	30	100	75.2	64.4
2	-6	30	90	75.2	64.4
3	-6	30	75	75.2	64.4
4	-6	30	55	75.2	64.4
5	-6	30	40	75.2	64.4
6	-6	30	75	72.4	63.5
7	-6	30	75	69.6	62.5
8	-6	30	75	78.0	65.3

3.4.4 Response Characterization to Control Inputs Test

As noted previously, there are several different ways to modulate the power use of a commercial refrigeration system. A series of tests will be performed to characterize the system response to step changes in these control inputs as shown in Table 5. The following are specific measurements of interest.

- **Response time:** After a control change is initiated, the response time is how long it takes the system to respond. This measure accounts for delays in the controls of the system and is a critical metric for grid services requiring a fast response.
- **Time to steady state:** After the system responds to a control change, the time to steady state is a measure of how long it takes the system power consumption to reach steady-state. This measure accounts for control limitations in the slew rate of equipment or hardware limitations on how fast a system can respond. The response may also include spikes, overshoots, or other transient responses that are of interest, particularly if the control is cycling the unit on and off.
- **Magnitude of power change:** The flexibility in the power consumption of the system is a critical value for the virtual battery model. Different control inputs have different limits on how much the power consumption can be changed and whether intermediate values can be achieved.
- **Duration of power change:** This is a measure of how long the power change can be maintained before the temperatures in the display cases exceed the limits. It is expected that large changes in power will only be able to be maintained for a shorter duration than smaller changes in power.
- **Change in efficiency:** Different control inputs may affect the efficiency of the system differently. There are different losses associated with the different controls, and identifying the most efficient control method is desirable.

Table 5. Tests for Characterizing System Response to Control Inputs

Control Input	Change in Setting	Outdoor Dry Bulb Range ^a (°F)	Indoor Dry Bulb ^b (°F)	Indoor Wet Bulb ^b (°F)
Medium Temperature (MT) Suction Header Pressure	Up to ±5 psi	45–100	75	65
Low Temperature (LT) Suction Header Pressure	Up to ±5 psi	45–100	75	65
MT case temperature set point	Up to ±5F on one or both cases	45–100	75	65
LT case temperature set point	Up to ±5F on one or both cases	45–100	75	65
Refrigerant flow to MT case	On→Off and Off →On for one or both cases	45–100	75	65
Refrigerant flow to LT case	On→Off and Off →On for one or both cases	45–100	75	65

MT false load heater	Number of heaters to be turned ON: 0 →2 →3 →4 →5 →6 →7→8 →9 and 9 →8 →7 →6 →5 →4 →3→2 →0	45–100	75	65
LT false load heater	Number of heaters to be turned ON: 0 →1 →2 and 2 →1 →0	45 – 100	75	65

^aThe outdoor dry bulb temperature is not controlled and depends on the ambient conditions.

^bThe indoor is an air conditioning environment, but the indoor dry bulb and wet bulb temperatures are not precisely controlled; the values are approximated according to the temperature reading.

3.4.5 Manufacturer Tests

Compressor manufacturers provide some performance test data (e.g., power consumption, cooling capacity) (Table 6) (Bitzer N.D.), which can also be used for calibration and validation of refrigeration system device models.

Table 6. Examples of Manufacturer Performance Test Data

Control Input	Evaporation Temperature (°C)	Condensation Temperature (°C)
Medium temperature compressors	0, 10, 20, 30, 40, 50, 60	50, 60, 70, 80, 86, 95, 104, 113, 122
Low temperature compressors	-25, -30, -35, -40, -45, -50	10, 5, -5, -10, -20

3.5 Experimental Results and Model Validation

Both manufacturer performance test data and laboratory experimental data were used to calibrate and validate the model prediction of display case temperature, including case air temperature, food temperature, and refrigeration system power consumption. The results are discussed in the following sections.

3.5.1 Experimental Results

Power consumption test results are plotted in Figure 13–Figure 17, which demonstrate the influence of changing the compressor suction pressure set point, display case air temperature set point, and false load heater on power consumption.

- MT suction pressure:
The influence of the MT suction head on the MT compressor power consumption is shown in Figure 13. The test varied the MT suction head (saturated temperature) from 11°C to 21°C with steps of 5°C. The MT compressor power consumption decreased as the suction head temperature increased. We noticed that modulation of the MT suction head temperature could lead to oscillation of the suction head.

- **LT suction pressure:**
Figure 14 plots the variation in LT compressor power consumption as LT suction pressure is changed. The LT suction pressure set point changed within the range of -21°C to -31°C . The LT compressor power consumption varied at different suction head temperatures. Similar as the MT suction head, modulation of the LT suction head temperature could lead to oscillation of the suction head.
- **MT display case air temperature:**
The test results for changing the MT display case air temperature set point are plotted in Figure 15. During the test, the MT display case air temperature set point was adjusted from between 25°F and 35°F . The results indicate the power consumption of MT compressor varies between 8 and 17 in average kW.
- **LT display case air temperature:**
As shown in Figure 16, the LT display case air temperature set point was changed from -6°C to -11°C , then -1°C , and finally back to -6°C . The results indicated that the LT compressor turned on more frequently under a set point of -11°C and less frequently at a set point of -1°C compared to a set point of -6°C . The power consumption of the LT compressor changed accordingly.
- **MT false load:**
The false load test, as shown in Figure 17, stepped the false load heater from two to eight one by one. The MT compressor power consumption increased accordingly. During the defrost cycle, the MT power consumption dropped in some periods during the test.

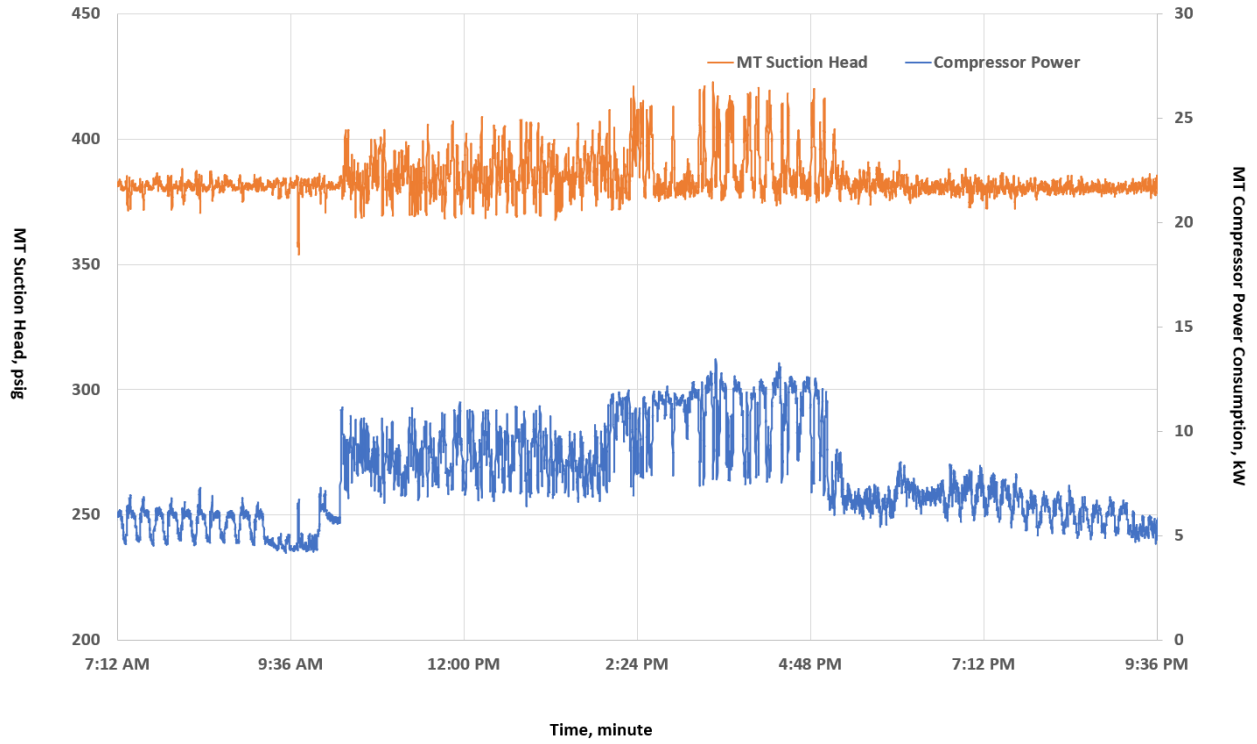


Figure 13. Medium temperature (MT) compressor power consumption at different MT suction pressure set points

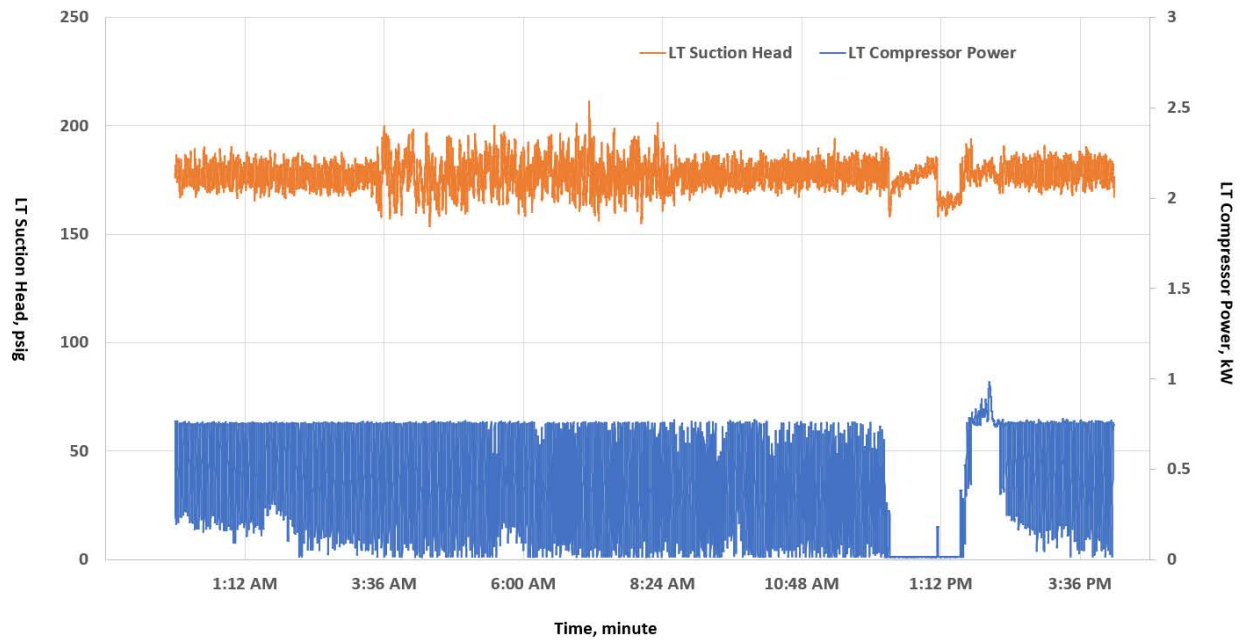


Figure 14. Low temperature (LT) compressor power consumption at different low temperature suction pressure set points

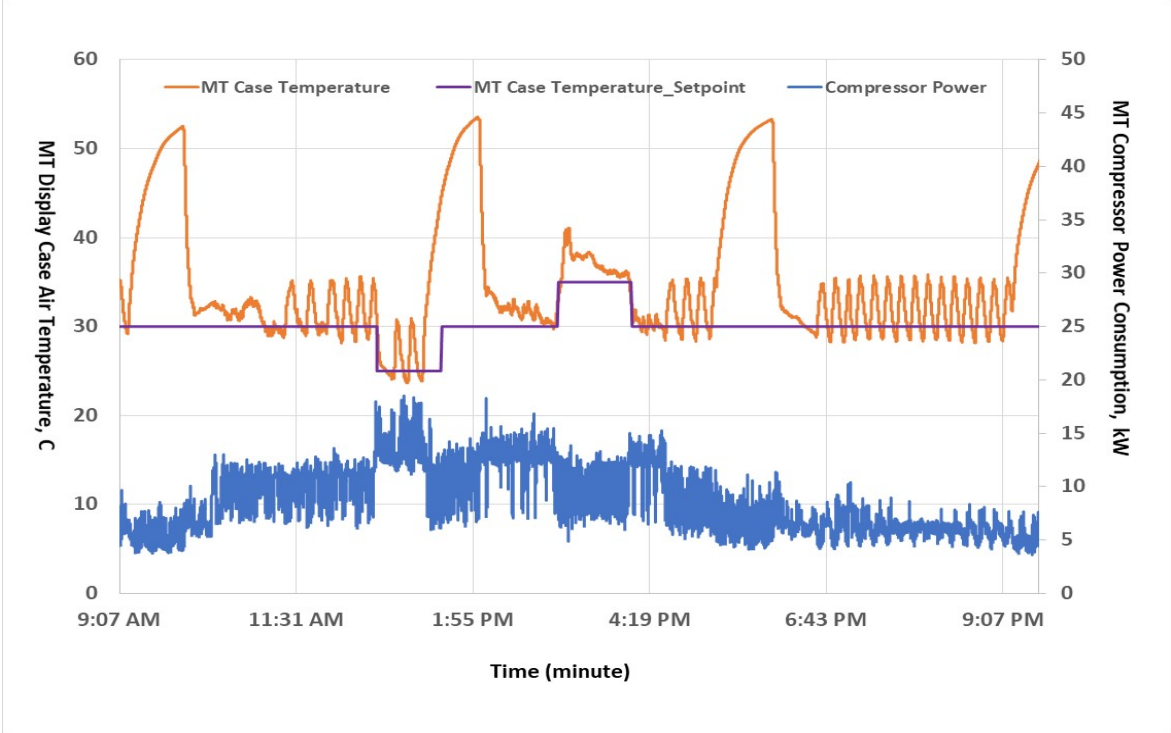


Figure 15. Medium temperature (MT) compressor power consumption at different MT display case air temperature set points

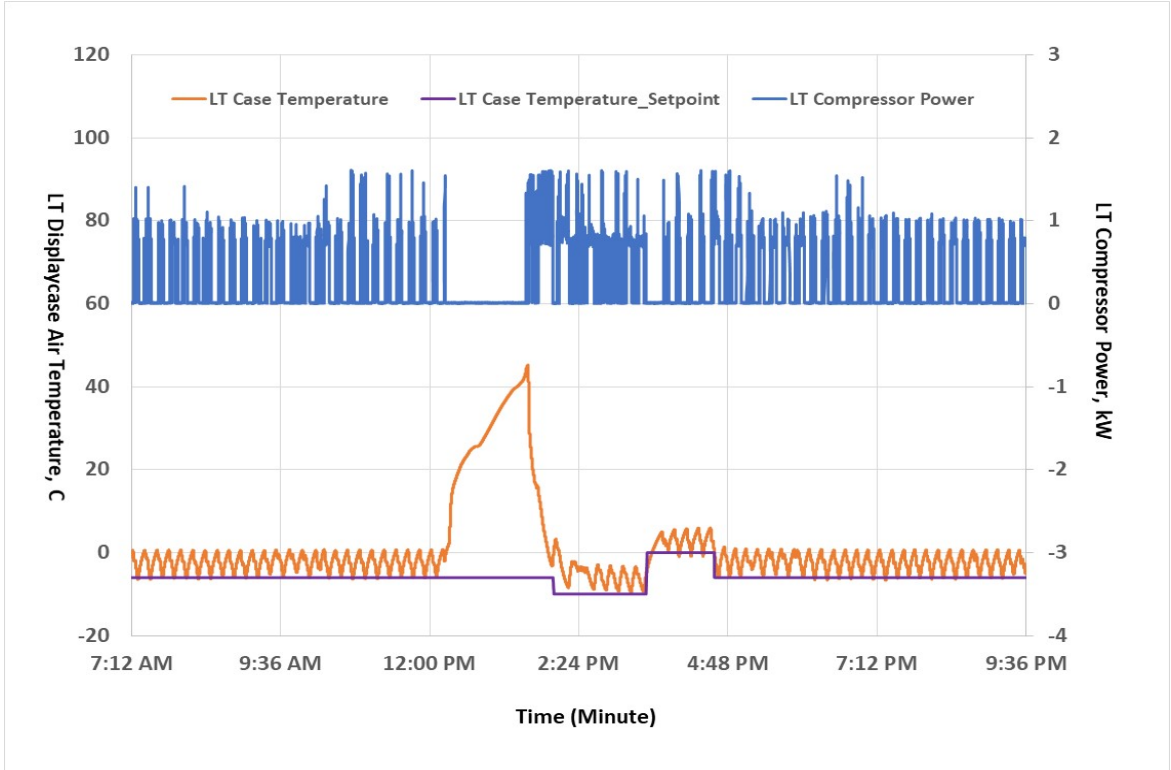


Figure 16. Low temperature (LT) compressor power consumption at different LT display case air temperature set points

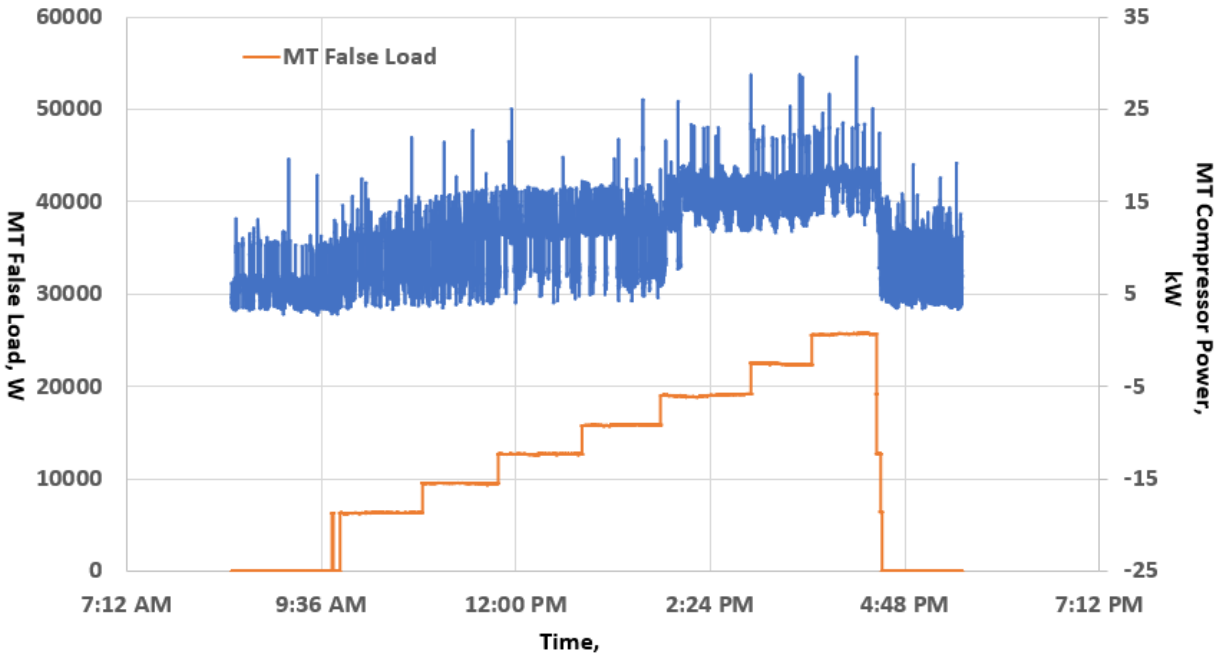


Figure 17. Medium temperature (MT) compressor power consumption at different false loads

3.5.2 Power Consumption Calibration and Validation

The commercial refrigeration system power consumption components include MT compressors (one variable speed and two fixed speed), LT compressors (one variable speed and one fixed speed), two fixed-speed gas cooler fans, and one fixed-speed display case evaporator fan. Because the fans are fixed speed, they consume a relatively small percentage of the power compared to the compressors. The accurate prediction of compressor power consumption is the most critical factor for estimating total system power consumption.

The compressor manufacturer data can be used to calibrate the reduced model discussed in section 2. The model parameters are identified and listed in Table 7.

Table 7. Compressor Parameters

Low Temperature (LT)	LT_2MSL-07K	LT_2KSL-1K
a ₀	215.5507761	327.4501456
a ₁	-14.0674587	-23.86936961
a ₂	-0.151139912	-0.253120663
a ₃	17.72476551	29.50798137
a ₄	-0.039997352	-0.05600268
a ₅	0.265484865	0.426545153
a ₆	6746.846085	10994.40286
a ₇	132.7492133	212.3219856
a ₈	0.690417918	1.087957604
a ₉	-55.02242334	-87.15702764
a ₁₀	0.101191569	0.139549028
a ₁₁	-0.632892268	-1.001876311

Table 7. Compressor parameters (continued)

Medium Temperature (MT)	4MTC-7K	4MTC-10K
b ₀	3743.692211	3677.089459
b ₁	-113.1469513	-115.2126198
b ₂	-0.949968838	-0.909689722
b ₃	5.866269538	5.977244154
b ₄	0.426104769	0.478541268
b ₅	1.741848346	1.707071315
b ₆	31930.52927	38545.43758
b ₇	802.6804349	895.2242371
b ₈	2.930720513	3.439209561
b ₉	-201.986731	-427.6732271
b ₁₀	-0.343492271	1.427300647
b ₁₁	-5.958668834	-7.221110318
k ₀	1	0.861088
k ₁	0	-0.00307
k ₂	0	-4.2E-05
k ₃	0	3.90E-06

The calibration performance is shown in Figure 18–Figure 21 and indicates the high-level accuracy, within $\pm 2\%$ error, for all compressors.

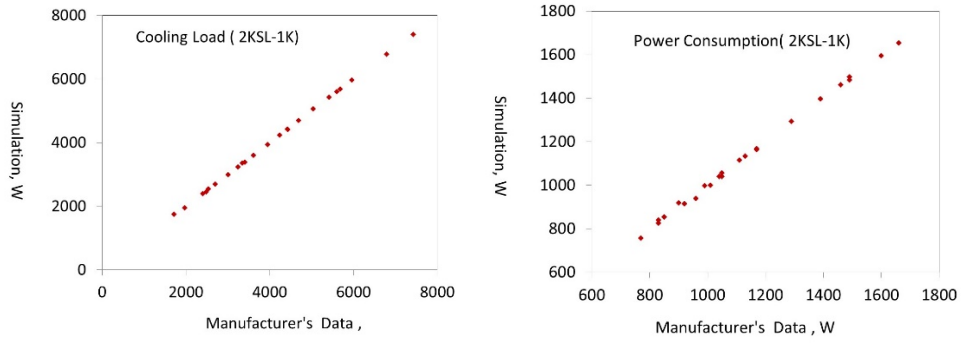


Figure 18. Power consumption calibration for compressor 2KSL-1K

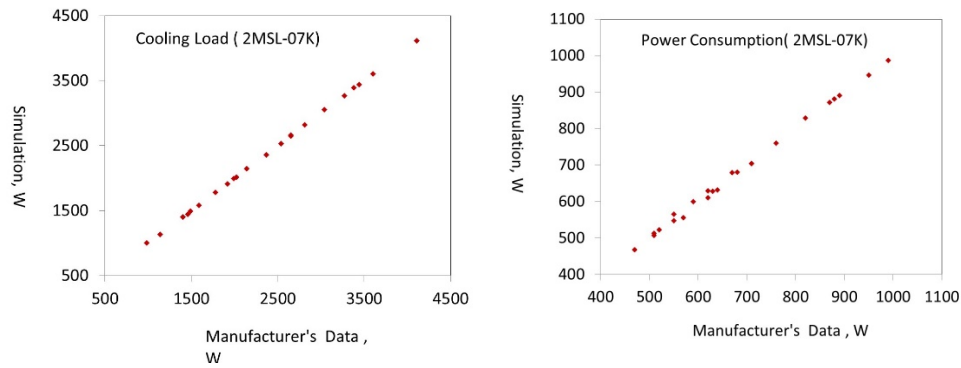


Figure 19. Power consumption calibration for compressor 2MSL-07K

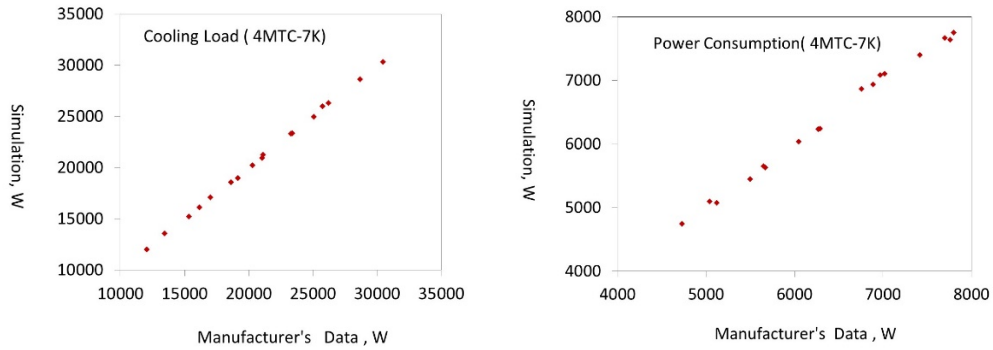


Figure 20. Power consumption calibration and validation data for compressor 4MTC-7K

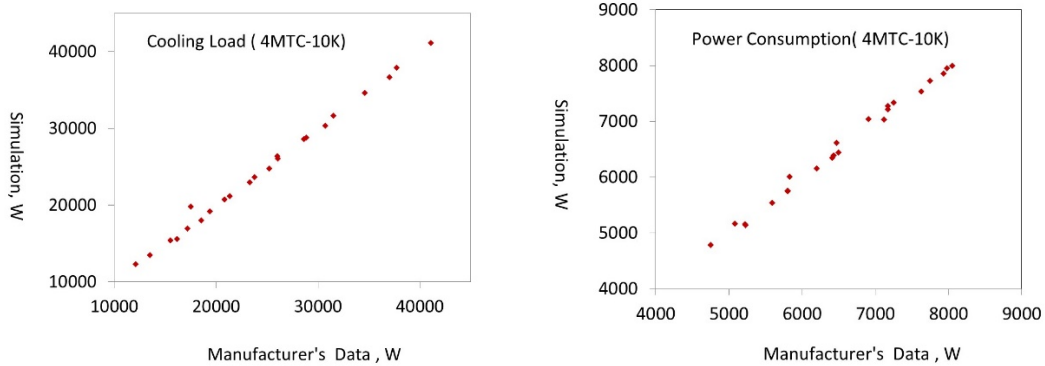


Figure 21. Power consumption calibration and validation data for compressor 4MTC-10K

Validation Test Case 1

The first validation test case used the data set collected from 5:00 pm on February 6, 2019, to 12:00 pm on February 7, 2019. The display case air temperature set points were -6°F for LT and 30°F for MT. The ambient temperature varied between 65°F and 80°F . The data sampling rate was around 3.75 s (16 data points per minute). The measured power consumption of the LT and MT compressors was compared to the simulation results, as shown in Figure 22 to Figure 25. Figure 22 and Figure 23 compared the measured power consumption of the LT and MT compressors with the simulation results from the reduced model, which took SST, SMT, and SDT as input variables. Figure 24 and Figure 25 compared the measured power consumption of the LT and MT compressors with the simulation results from the simplified reduced model, which took ambient temperature and case temperature as input variables. The results indicate the following.

- For the LT compressors, both the reduced model and the simplified reduced model maintained high accuracy in predicting power consumption.
- For the MT compressors, the reduced model maintained high accuracy in power prediction, while the simplified reduced model had reasonable accuracy.

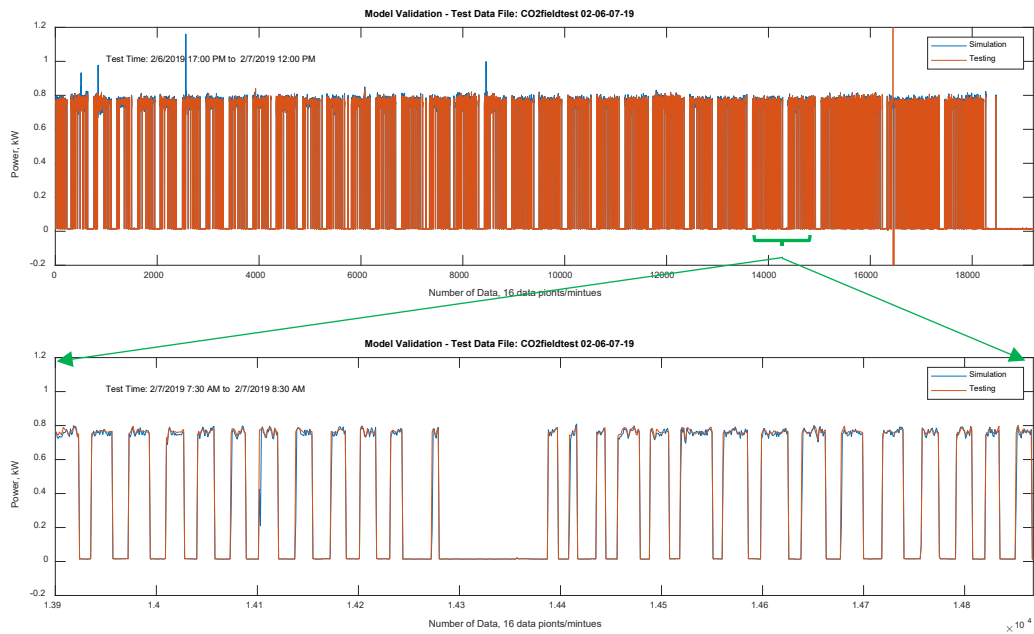


Figure 22. Low temperature compressor power consumption comparison of simulation and test data from validation test case 1

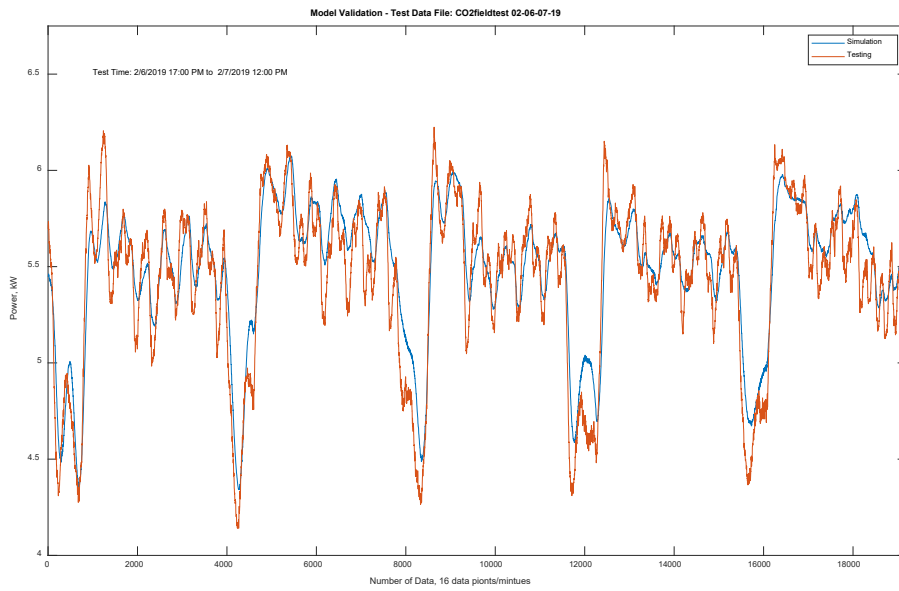


Figure 23. Medium temperature compressor power consumption comparison of simulation and test data from validation test case 1

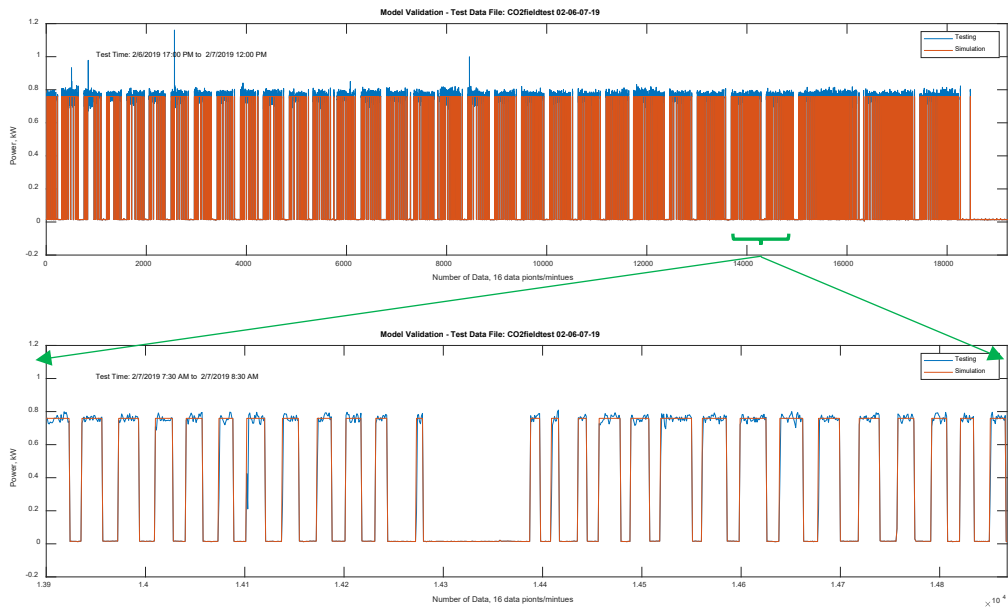


Figure 24. Low temperature compressor power consumption comparison of simulation and test data from validation test case 1

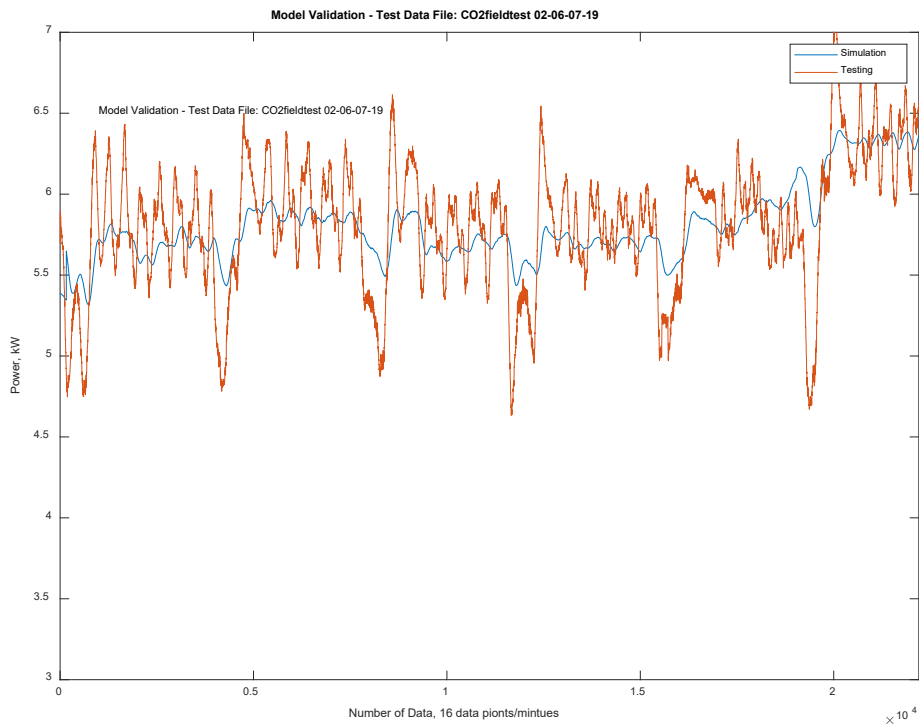


Figure 25. Medium temperature compressor power consumption comparison of simulation and test data from validation test case 1

Validation Test Case 2

The second validation test case used the data set collected from 5:00 pm on February 7, 2019, to 12:00 pm on February 8, 2019. The display case air temperature set points were -3°F for LT and 30°F for MT. The ambient temperature dropped from 80°F to around 35°F . The data sampling rate was around 3.75 s (16 data points per minute).

The measured power consumption of the LT and MT compressors was compared to the simulation results, as shown in Figure 26 to Figure 29. Figure 26 and Figure 27 compared the measured power consumption of the LT and MT compressors with the simulation results from the reduced model, which took SST, SMT, and SDT as input variables. Figure 28 and Figure 29 compared the measured power consumption of the LT and MT compressors with the simulation results from the simplified reduced model, which took ambient temperature and case temperature as input variables. The results indicate the following.

- For the LT compressors, both the reduced model and the simplified reduced model maintained high accuracy in predicting power consumption.
- For the MT compressors, the reduced model maintained high accuracy in power prediction, while the simplified reduced model had reasonable accuracy.
- For the MT compressors, both the reduced model and the simplified reduced model accurately predicted the power changes caused by the ambient temperature variation.

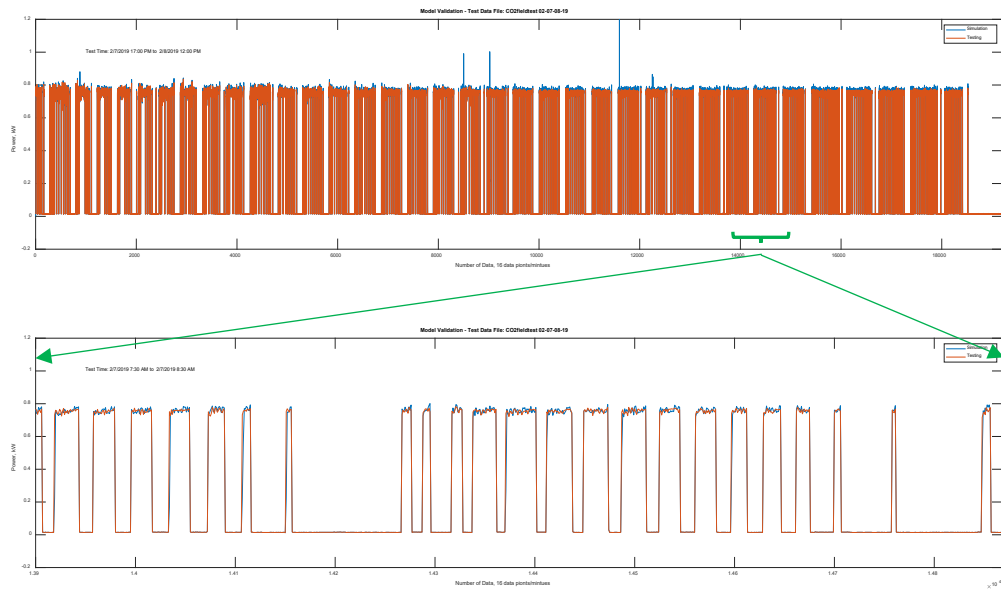


Figure 26. Low temperature compressor power consumption comparison of simulation and test data from validation test case 2

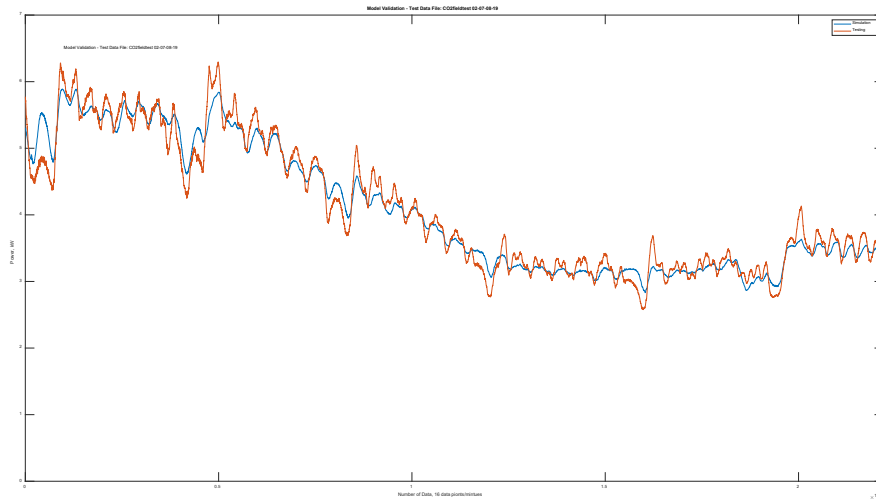


Figure 27. Medium temperature compressor power consumption comparison of simulation and test data from validation test case 2

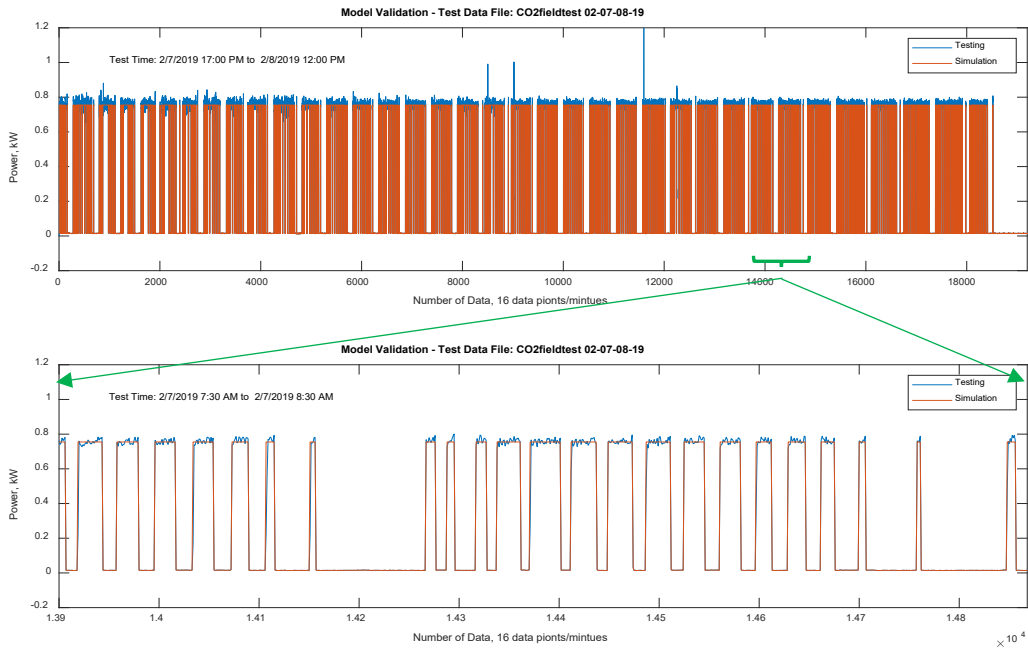


Figure 28. Low temperature compressor power consumption comparison of simulation and test data from validation test case 2

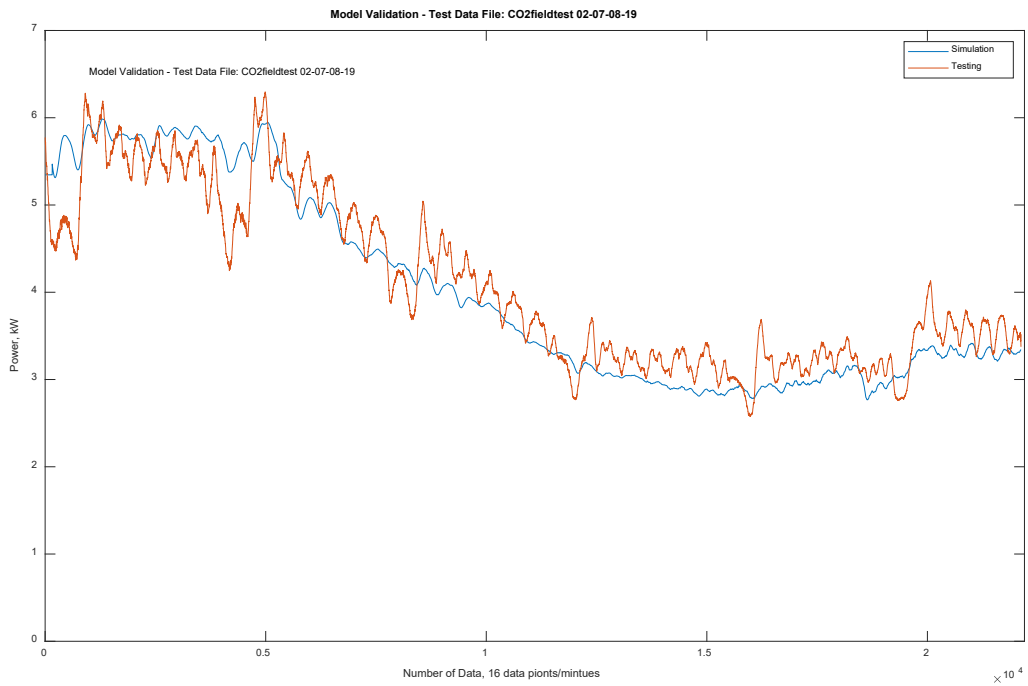


Figure 29. Medium temperature compressor power consumption comparison of simulation and test data from validation test case 2

Validation Test Case 3

The third validation test case used the data set collected from 12:00 am to 11:59 pm on Aug. 12, 2019. The display case air temperature set point was 30°F for MT. The LT compressors and display case were off. The ambient temperature varied from 60°F to 100°F. The data sampling rate was around 1 s. The false load heaters were all scheduled off from 12:00 am to 9:22 am; seven heaters were scheduled on from 9:22 am to 11:50 am; four heaters were scheduled on from 11:50 am to 2:05 pm; seven heaters were scheduled on from 2:05 pm to 3:20 pm; six heaters were scheduled on from 3:20 pm to 4:00 pm; all heaters were scheduled off from 4:00 pm to 11:59 pm.

The measured power consumption of the MT compressors was compared to the simulation results from the reduced model, which took SST, SMT, and SDT as input variables (Figure 30).

- For the MT compressors, the reduced model maintained high accuracy in power prediction except for a time period right after 9:22 am, when all seven heaters were turned on. Other than that, the reduced model predicted power consumption well and caught the power variation when the heaters turned on and off.

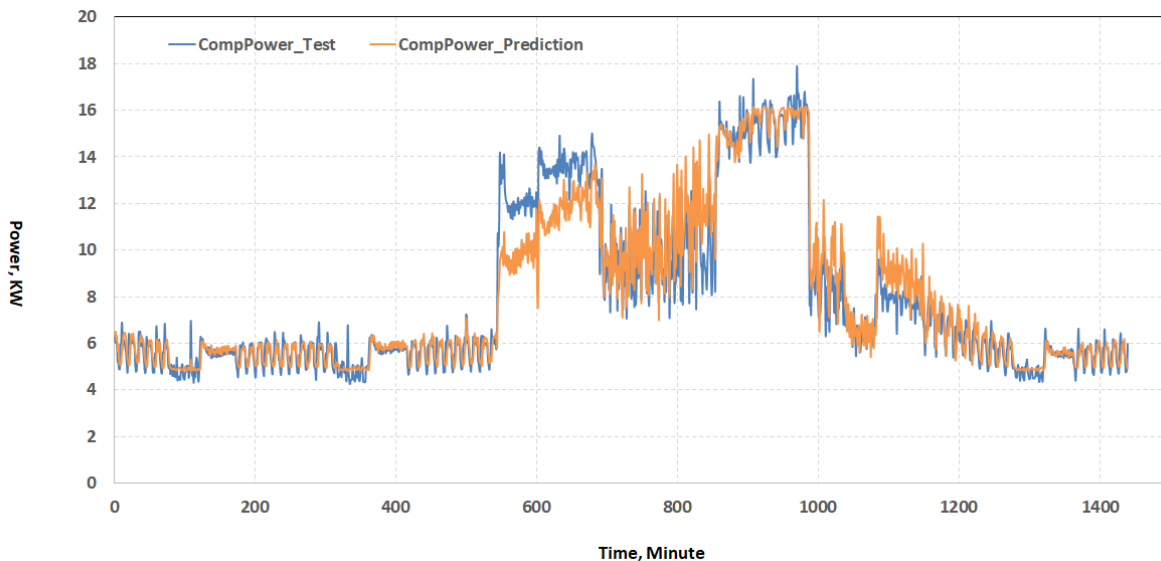


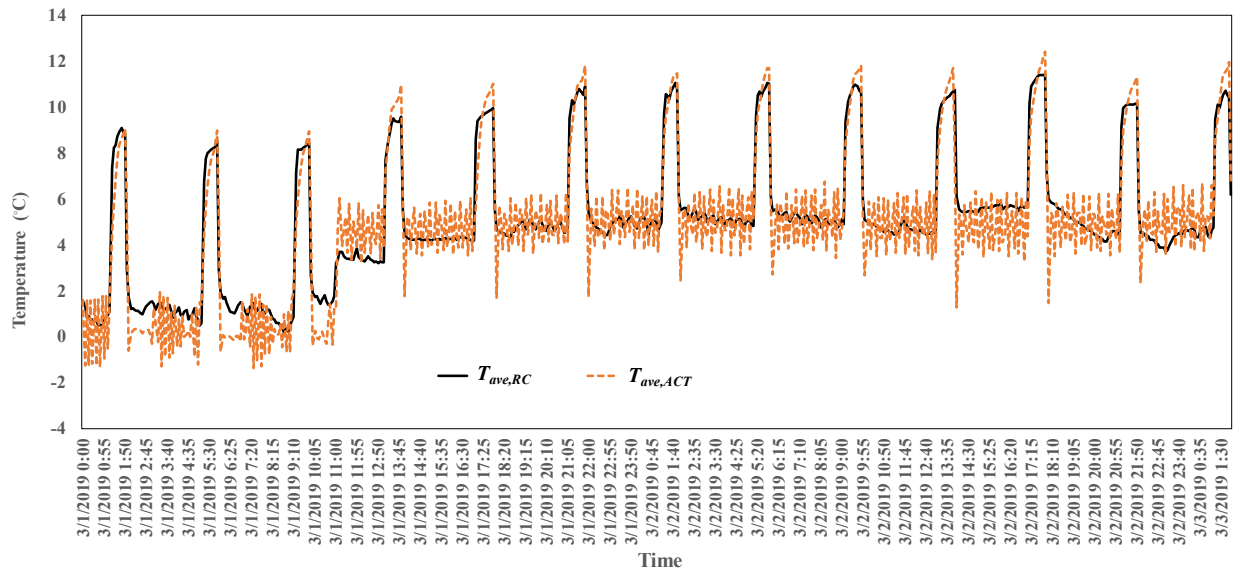
Figure 30. Comparison of simulated and measured power consumption from validation test case 3

3.5.3 Display Case Temperature Calibration and Validation

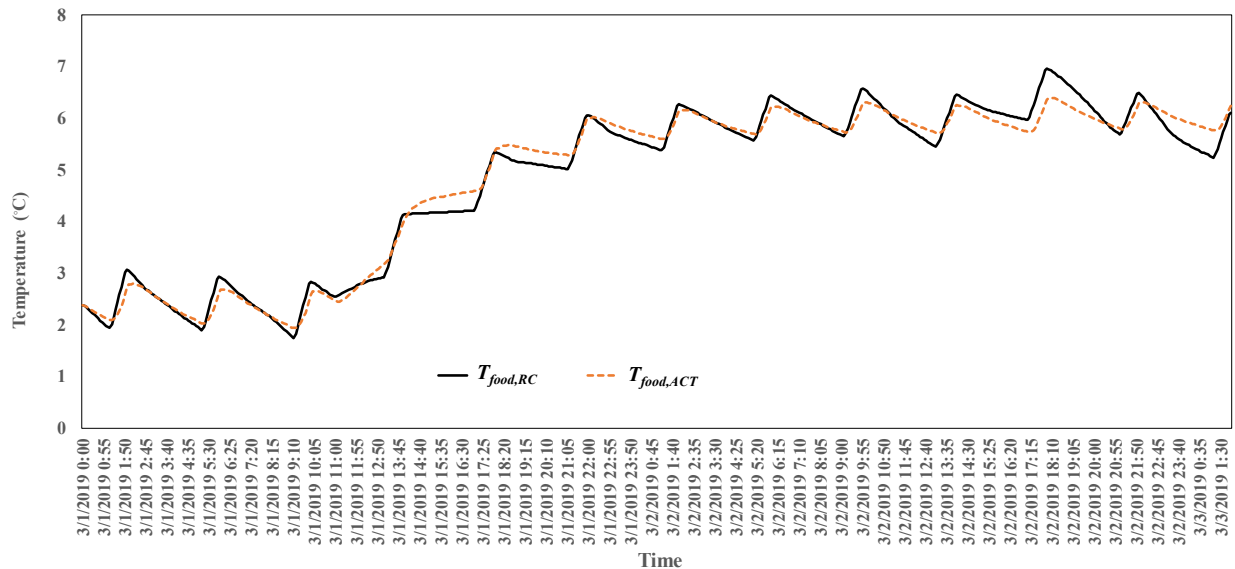
The refrigeration case models were tested and validated with data collected from the reference refrigeration system in different consecutive time periods with various operating conditions, e.g., different schedules of supply air temperature set points. The data collected from March 1, 2019, to March 2, 2019, and March 3, 2019, to March 5, 2019, were used for training and validation, respectively, of the developed open case model. The data collected from July 22, 2019, 11:30 am, to July 26, 2019, 8:59 am, and July 26, 2019, 9:00 am, to August 1, 2019, 11:59 pm, were used for training and validation, respectively, of the developed closed case model.

The training and testing results for the open case model are shown in Figure 31 and Figure 32. $T_{ave,act}$ and $T_{food,act}$ are the measured case supply air and food temperatures, respectively. $T_{ave,RC}$ and $T_{food,RC}$ are the case supply air and food temperatures from the model for a 24-hour prediction horizon. The resulting parameters identified by PSO are $R_{infil} = 0.00575$ K/W, $R_{food} = 0.003915$ K/W, $R_{case} = 0.03647$ K/W, $C_{air} = 75,964$ J/K, $C_{food} = 3,245,969$ J/K, $C_{case} = 19,109,514$ J/K, $CI = 0.1792$, and $SpI = 0.6862$.

The training and testing results for the closed case model are shown in Figure 33 and Figure 34. The resulting parameters identified by PSO are $R_{infil} = 0.015954$ K/W, $R_{food} = 0.003993$ K/W, $R_{case} = 0.074229$ K/W, $C_{air} = 106,454.1$ J/K, $C_{food} = 2,816,670$ J/K, $C_{case} = 20,668,608.24$ J/K, $CI = 1.1$, and $SpI = 0.8163$.

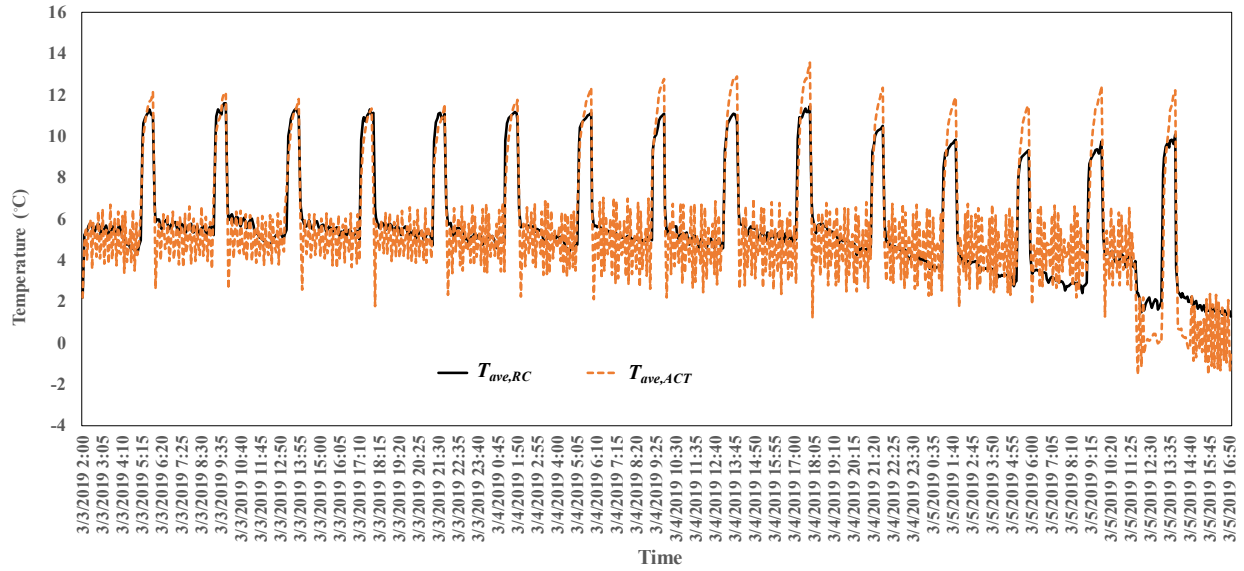


(a) Air in case temperature comparisons

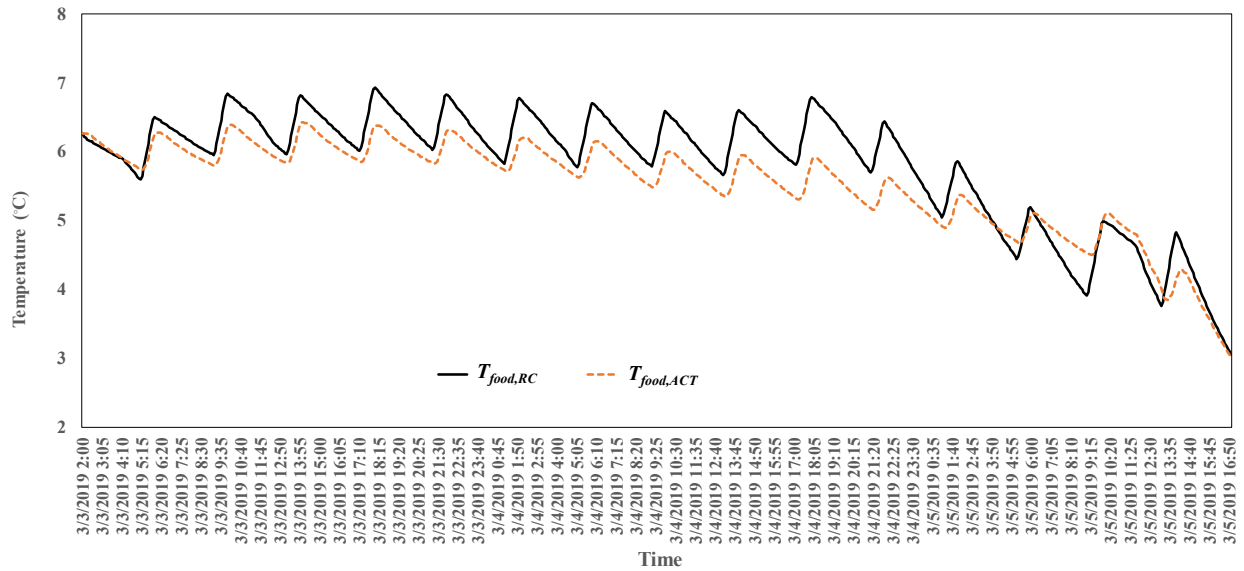


(b) Food temperature comparisons

Figure 31: Open case refrigerator display case model training results from March 1 to March 2, 2019

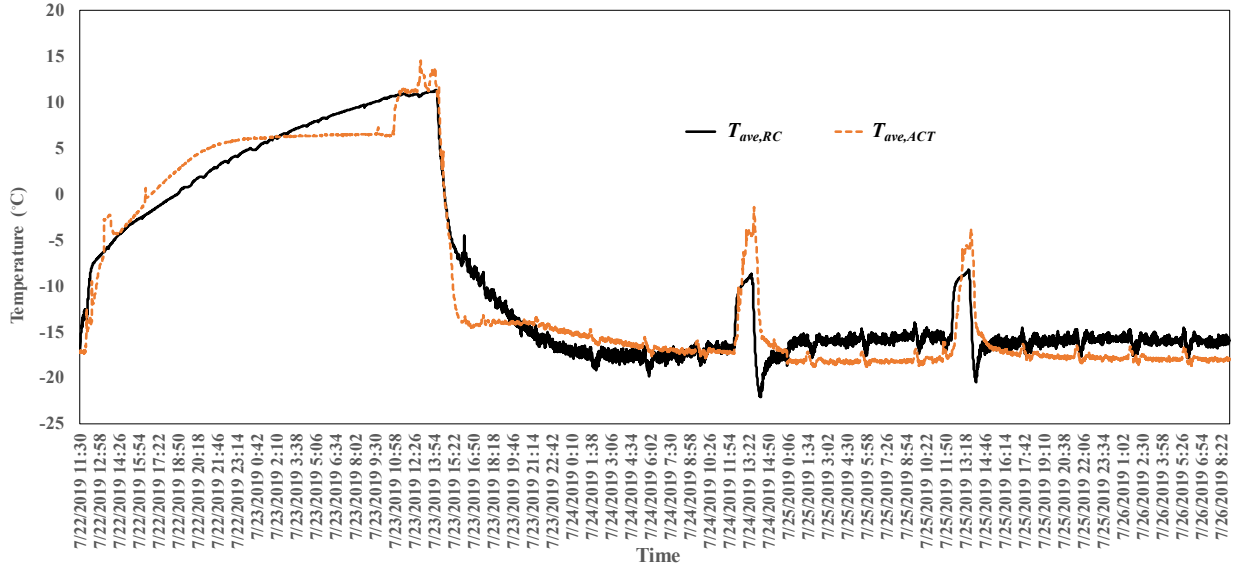


(a) Air in case temperature comparisons

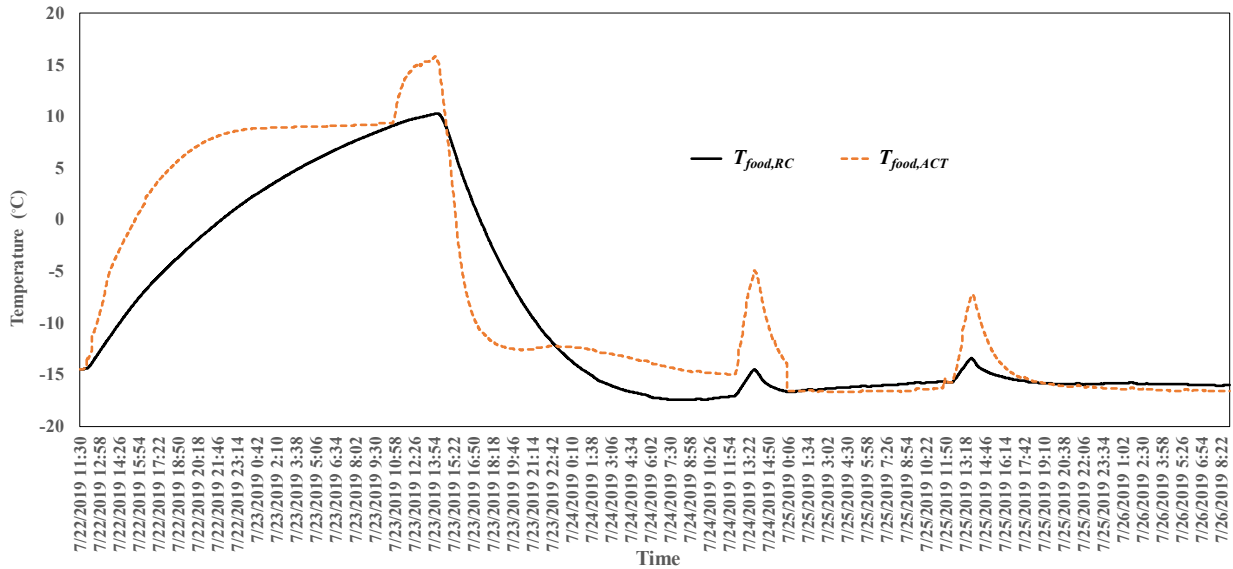


(b) Food temperature comparisons

Figure 32. Open case refrigerator display case model validation results from March 3 to March 5, 2019

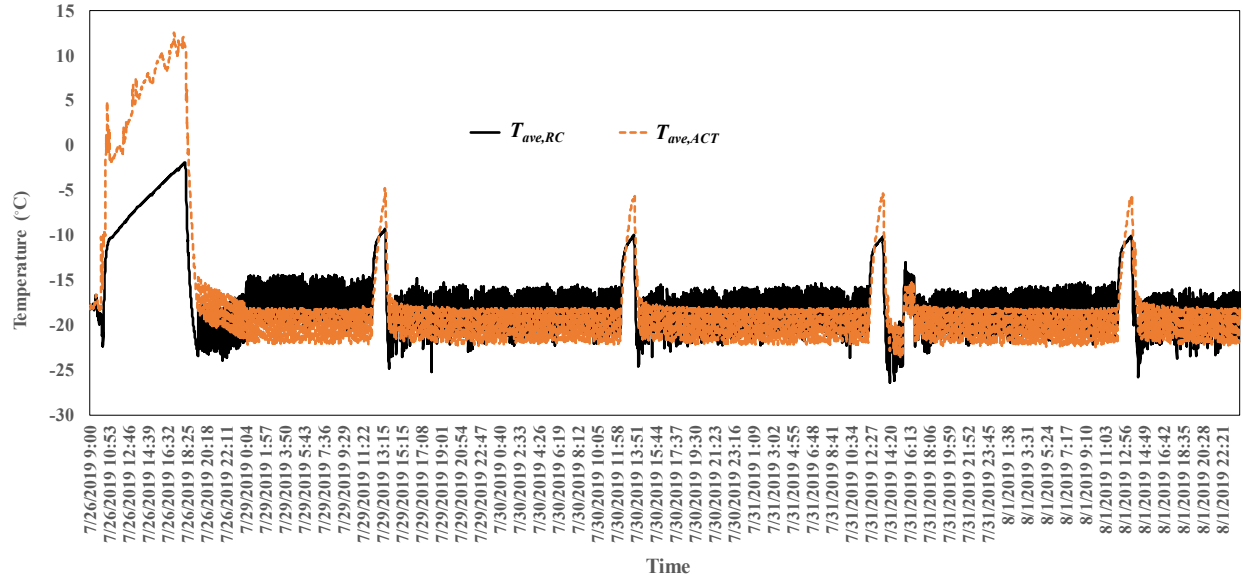


(a) Air in case temperature comparisons

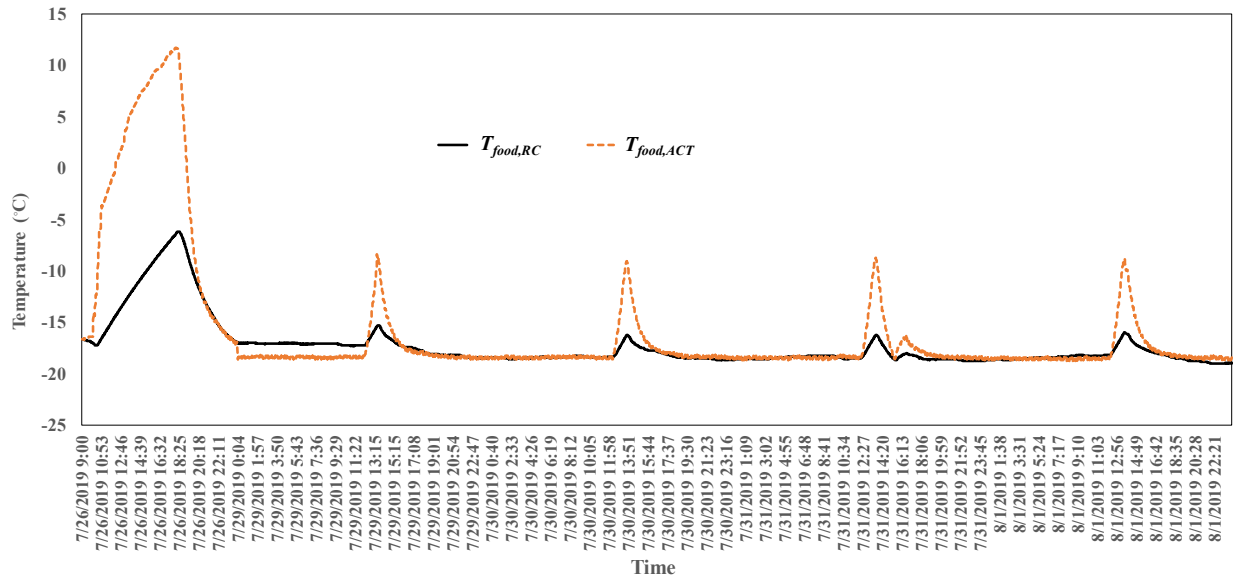


(b) Food temperature comparisons

Figure 33. Closed case refrigerator display case model training results from July 22 to July 26, 2019



(a) Air in case temperature comparisons



(b) Food temperature comparisons

Figure 34. Closed case refrigerator display case model validation results from July 26 to August 1, 2019

To quantify the deviations of the predicted data from the measured data in both the training sessions and testing sessions, the RMSE index was used to evaluate the deviations (Table 8).

Table 8. Accuracy Indices of the Developed Open/Closed Case RC (Resistance-Capacity) Models

Time	Open/closed case model	Training/validation	Root mean square error	
			T_{ave}	T_{food}
3/1/2019 to 3/2/2019	Open case model	Training	1.19	0.21
3/3/2019 to 3/5/2019		validation	1.48	0.40
7/22/2019 to 7/26/2019	Closed case model	Training	2.96	1.66
7/26/2019 to 8/1/2019		validation	2.39	1.96

T_{ave} = case supply air temperature; T_{food} = case food temperature.

It was found that the developed RC (Resistance-Capacity) model performs satisfactorily in the prediction of case supply air and food temperatures.

3.5.4 System Validation

The system validation is to integrate the display case model and commercial refrigeration system model with the control model and to take actual test inputs (e.g., ambient temperature, display case set points). The system validation will predict the display case air temperatures and refrigeration system power consumption so that it can be compared with measured values to validate these simulation models.

One-day test data (July 13, 2019) was selected to perform the system validation study. The display case air temperature set points were -6°F for LT and 30°F for MT. The ambient temperature varied between 70°F and 95°F. The data sampling rate was around 1 s. The measured closed (LT) and open (MT) display case temperatures and LT and MT compressor power consumption were compared to the simulation results, as shown in Figure 35 to Figure 38. Figure 35 shows the measured vs. predicted closed (LT) display case air temperature. Figure 36 compares the measured power consumption of LT compressors with the simulation results. The measured vs. predicted open (MT) display case air temperatures are shown in Figure 37. Figure 38 compares the measured power consumption of MT compressors with the simulation results. The results indicate the following.

- For the LT compressors, both display case air temperature and compressor power consumption were predicted by the proposed system model with reasonable accuracy, as shown in Figure 35 and Figure 36.
- For the MT compressors, the display case air temperature predictions matched well with the air temperature test results trend but missed the temperature fluctuations (Figure 37). Figure 38 indicates good agreement on total compressor power consumption between the models and laboratory test results.

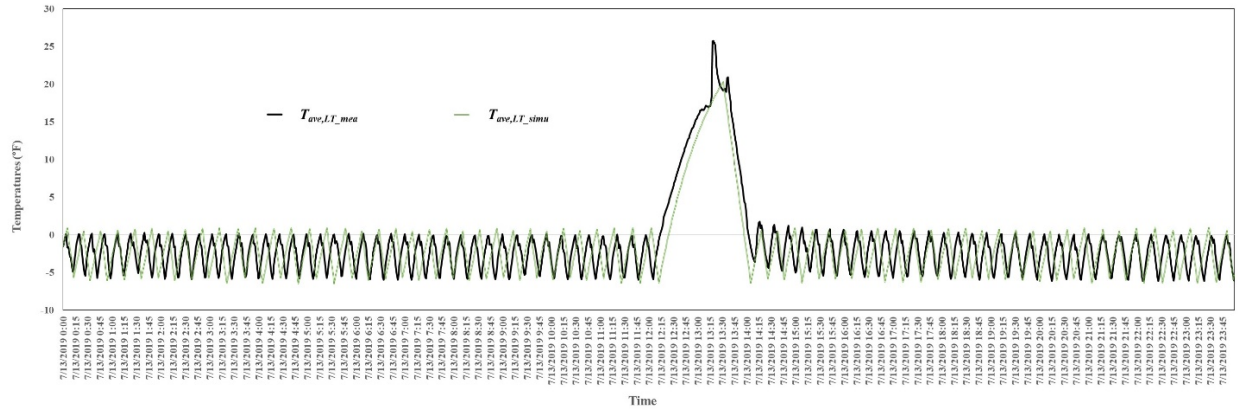


Figure 35. Closed low temperature (LT) display case air temperature: test vs. prediction

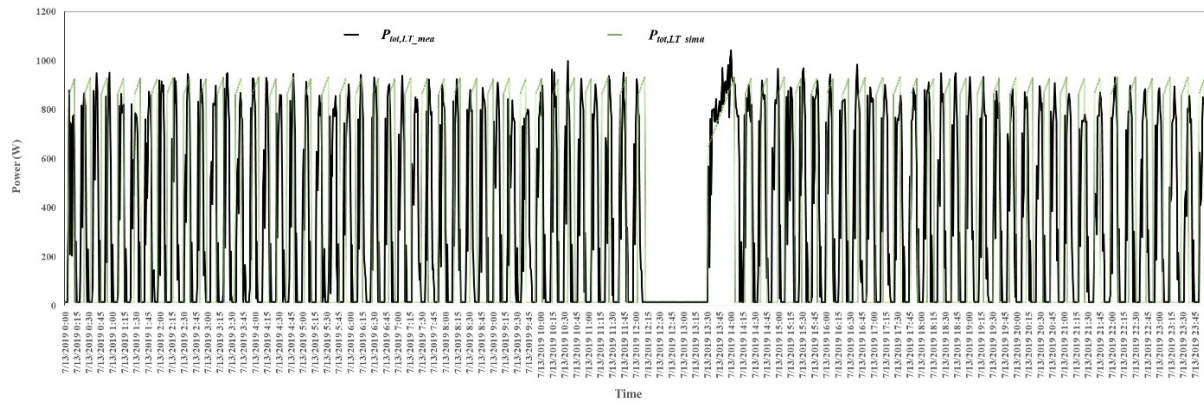


Figure 36. Low temperature (LT) compressor power consumption: test vs. prediction

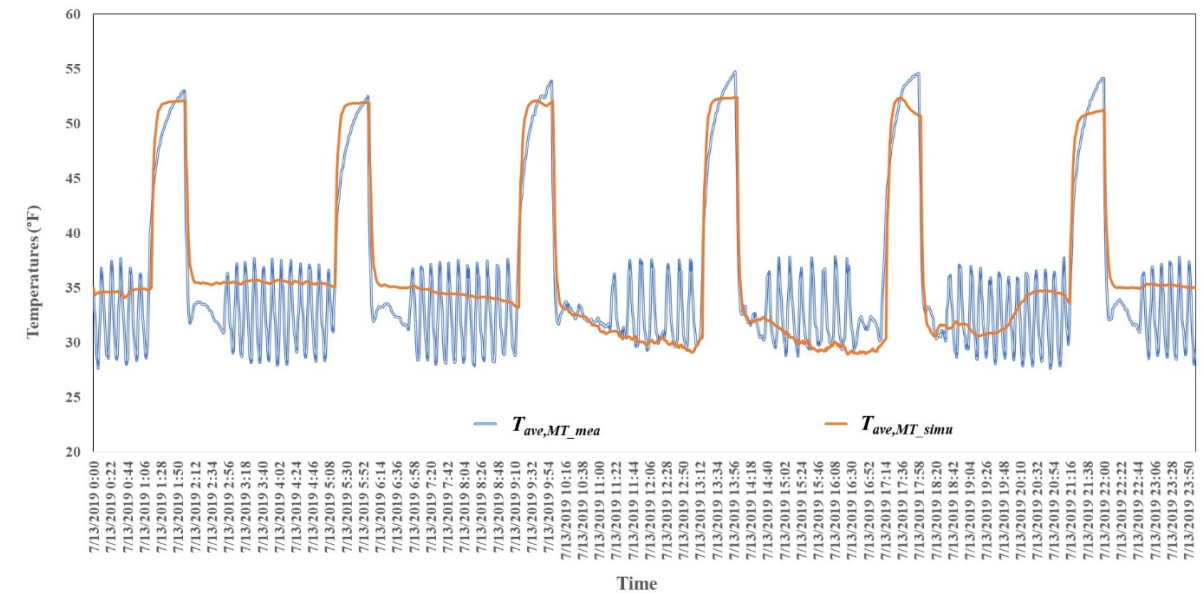


Figure 37. Open medium temperature (MT) display case air temperature: test vs. prediction

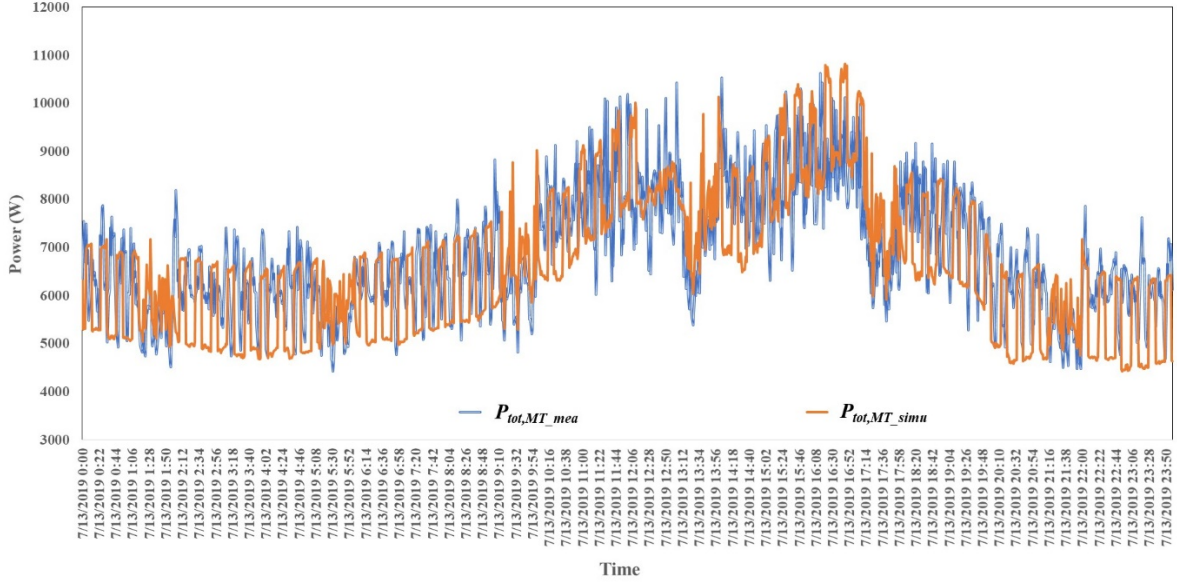


Figure 38. Medium temperature (MT) compressor power consumption: test vs. prediction

3.6 Battery-Equivalent Model

The commercial refrigeration system device models have been developed, calibrated, and validated through experimental data. The main task of this chapter is to develop a battery-equivalent model for commercial refrigeration systems and convert the device model to this battery-equivalent model.

The SOC (state of charge) is defined as

$$SOC = \frac{T - T_{set}}{T_{max} - T_{set}}. \quad (41)$$

where, T refers to air in the case (T_{ave}) and T_{max} is the allowable upper boundary of T .

The reference capacity of a commercial refrigeration system is

$$Cap_{fixed} = C_p(T_{max} - T_{set}). \quad (42)$$

According to Eq. (41),

$$SOC(t + 1) - SOC(t) = \frac{T(t+1) - T(t)}{T_{max} - T_{set}}. \quad (43)$$

Combining Eq. (42) and Eq. (43) gives

$$SOC(t + 1) - SOC(t) = C_p \frac{T(t+1) - T(t)}{Cap_{fixed}}. \quad (44)$$

Substituting Eq. (1) into Eq. (44), and ignoring case temperature impact results in the commercial refrigeration system battery-equivalent model, gives

$$SOC(t + 1) - SOC(t) = \frac{1}{Cap_{fixed}} \left[\frac{T(t) - T_{food}(t)}{R_{food}} + \frac{T(t) - T_{amb}(t)}{R_{infil}} - \eta P_c \right] \Delta t. \quad (45)$$

Eq. (45) can be rearranged as

$$SOC(t + 1) - SOC(t) = \frac{1}{Cap_{fixed}} \left[\left(-\eta P_c + \frac{P_d}{\eta} \right) \Delta t - P_{loss} \Delta t \right], \quad (46)$$

where P_{loss} is defined as

$$P_{loss} = \frac{T(t) - T_{food}(t)}{R_{food}} + \frac{T_{amb}(t) - T(t)}{R_{infil}}. \quad (47)$$

Charge and discharge power are calculated as

$$P_{MT,charge} = 0.269Q_{MT,req} + 0.682T_{out}^2 - 59.185T_{out} - 22.833T_{set} - 0.958, \quad (48)$$

$$P_{LT,charge} = 0.182Q_{LT,req} + 12.525, \quad (49)$$

$$P_{MT,discharge} = 0, \quad (50)$$

$$P_{LT,discharge} = 0, \quad (51)$$

where, $Q_{MT,req}$ and $Q_{LT,req}$ are the required cooling capacity of MT and LT and can be calculated based on Eq.(30) and Eq. (32). Efficiency of the system is represented by η , which is calculated by dividing the required cooling capacity by the charging power.

The parameters to calculate fixed capacity and power loss are given in Table 9.

Table 9. Parameters for the Battery-Equivalent Model

Parameters	Low Temperature	Medium Temperature
C_p	106,454 J/K	75,964 J/K
R_{food}	0.003993 K/W	0.003915 K/W
R_{infil}	0.015954 K/W	0.00575 K/W

Note that there are several important assumptions:

1. It's assumed that $SOC_{thermal}$ (SOC), of which definition is defined in Equation 41, is equivalent to $SOC_{electrical}$ which is the required electrical state of charge from grid, as shown in the following equation:

$$SOC_{thermal} = SOC_{electrical} \quad (52)$$

2. The maximum charged electrical energy is equivalent to the maximum discharged electrical energy:

$$E_{Ch,max} = E_{Dis,max} \quad (53)$$

- The maximum charged electrical energy is fixed and determined by the maximum observed electrical energy consumed in a charging cycle.
- Both temperature and electrical power increase or decrease linearly.

Based on these assumptions and the calculation from the above equations, measured and simulated SOC and E_{Ch} (charged electrical energy) for both MT and LT cases, as shown in Fig. 39 and 40.

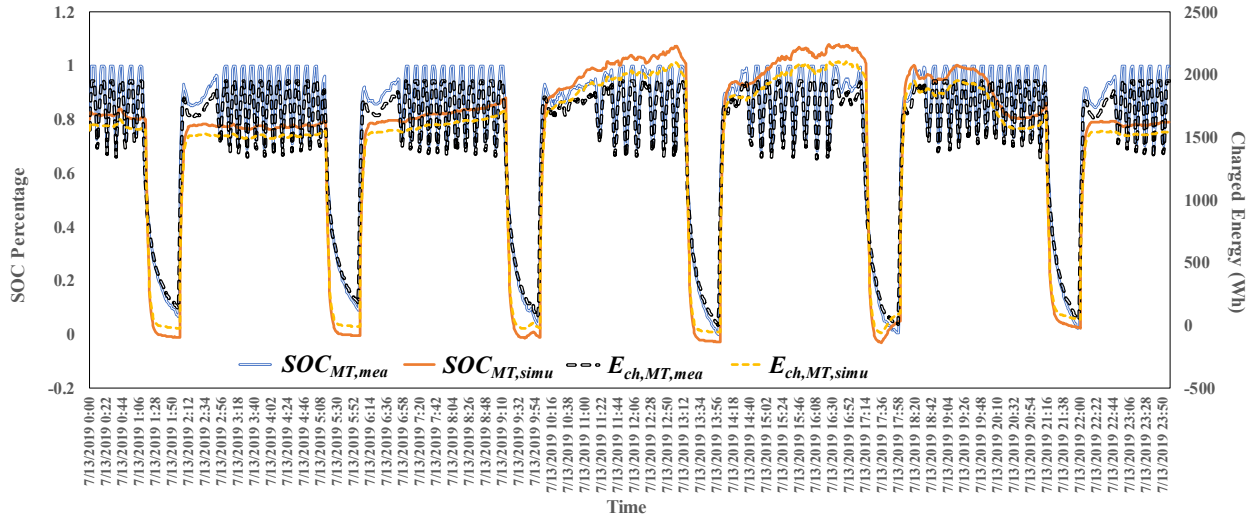


Fig 39. Measured and simulated SOC and E_{ch} of MT case

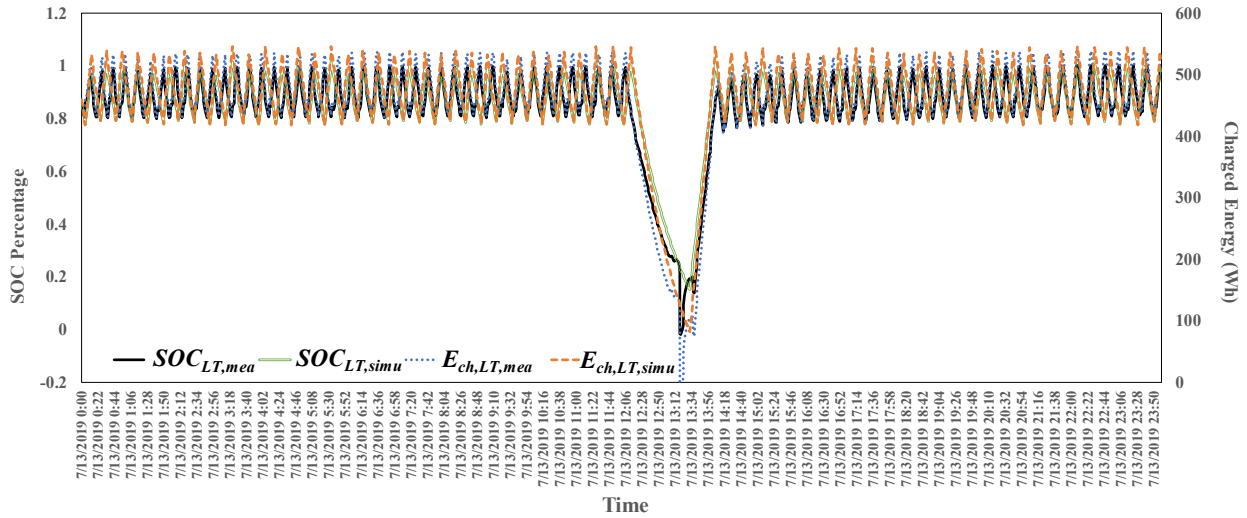


Fig 40. Measured and simulated SOC and E_{ch} of LT case

3.7 Conclusions

The conclusions of the commercial refrigeration system device model development and testing were ultimately based upon targeted stakeholder engagements and feedback in collaboration with the DOE national laboratory technical team. Commercial refrigeration system models were

developed in this study to predict display case temperatures, including air temperature and food temperature, and the power consumption of refrigeration systems. A general, standard device model with a battery-equivalent interface was used as the display case model. The refrigeration system power consumption was calculated through a reduced equipment model that provides a way to convert the heat transfer to or from the thermal storage to electrical power consumption of the equipment. Both manufacturer performance test data and laboratory experimental data were used to calibrate the model prediction of display case temperature and refrigeration system power consumption. The validated results indicate the model prediction error is within reasonable range.

In addition, this work yielded some useful insights.

- Commercial refrigeration can provide significant load flexibility through modulating the number of display cases ON/OFF, changing the display case air temperature set points and/or compressor suction head. Among them, modulation of the number of display cases ON/OFF is the most effective strategy for commercial refrigeration systems.
- The standard device model for display cases, integrated with the commercial refrigeration system reduced model and control model, can predict the load flexibility with acceptable accuracy.

Also, the following future improvement opportunities have been identified.

- Because the simplified reduced model only takes ambient temperature and display case temperature as inputs to model the LT and MT compressor power consumption, it is difficult to maintain high accuracy when predicting compressor power use, especially at partial load operation when the variable speed drive is modulated. A better model, taking limited inputs while maintaining high accuracy, is necessary.
- The current controls for commercial refrigeration system compressor speed generate high frequency, large magnitude oscillation in compressor variable frequency drive speed and power consumption. Proportional-integral-derivative controllers need to be retuned or redesigned to address this.
- A more detailed control model is necessary to represent the actual control logic of commercial refrigeration systems, which will improve the power prediction accuracy.

3.8 References

Bitzer. N.D. Bitzer CO₂/Semi-Hermetic reciprocating compressor subcritical and transcritical models.

Bourdouxhe, J.P., Grodent, M., and Lebrun, J. 1999. *HVACTOOLKIT: A Toolkit for Primary HVAC System Energy Calculation*. ASHRAE, ISBN 1-883413-73-7.

Hill Phoenix ADVANSOR CO₂ booster refrigeration system installation and startup manual, Version 3- Rev1, August 2013.

Pyswarm. N.D. “Particle swarm optimization (PSO) with constraint support.”
<https://pythonhosted.org/pyswarm/>.

Threlkeld, J.L. 1962. *Thermal Environmental Engineering*. Prentice-Hall, Englewood Cliffs, NJ.

Z. Xue, L. Shi, H. Ou. 2008. “Refrigeration flow characteristics of electronic expansion valve based on thermodynamic analysis and experiment.” *Applied Thermal Engineering* 28, 238-243.



This report was funded by the U.S. Department of Energy

1000 Independence Ave SW
Washington, DC 20585
(202) 586-5000

<https://gridmod.labworks.org/>